THESIS

SUMMERTIME OZONE PRODUCTION AT CARLSBAD CAVERNS NATIONAL PARK, NEW MEXICO: INFLUENCE OF OIL AND NATURAL GAS DEVELOPMENT

Submitted by
Andrey Marsavin
Department of Atmospheric Science

In partial fulfillment of the requirements
For the Degree of Master of Science
Colorado State University
Fort Collins, Colorado
Fall 2023

Master's Committee:

Advisor: Jeffrey L. Collett, Jr

Emily V. Fischer
Megan D. Willis

ABSTRACT

SUMMERTIME OZONE PRODUCTION AT CARLSBAD CAVERNS NATIONAL PARK, NEW MEXICO: INFLUENCE OF OIL AND NATURAL GAS DEVELOPMENT

Southeastern New Mexico's Carlsbad Caverns National Park (CAVE) has increasingly experienced summertime ground-level ozone (O_3) levels surpassing the US Environmental Protection Agency's National Ambient Air Quality Standard (NAAQS) of 70 parts per billion by volume (ppbv). The park is located in the western part of the Permian oil and natural gas (O&G) basin, where production rates have more than tripled in the last decade. We investigate O_3–precursor relationships by constraining a zero-dimensional (0-D) model to an hourly nitrogen oxides (NO_x = NO + NO_2) and speciated volatile organic compound (VOC) data set collected at CAVE during the summer of 2019. O&G-related VOCs dominated the calculated VOC reactivity with hydroxyl radicals (OH) on days when O_3 concentrations were primarily controlled by local photochemistry. Radical budget analysis showed that NO_x levels were high enough to impose VOC sensitivity on O_3 formation in the morning hours, while subsequent NO_x loss through photochemical consumption led to NO_x-sensitive conditions in the afternoon. Daily maximum O_3 was sensitive to both NO_x and O&G-related VOC emission reductions, with NO_x reductions generally being more effective. The model could not reproduce a 5-day high O_3 episode when constrained to observed NO_x and primary VOCs, likely due to influence from O_3 produced during air mass transport from regional O&G basins as indicated by back-trajectory analysis, low *i*/*n*-pentane ratios consistent with O&G emissions, increased concentrations of secondary VOCs, and extensive oxidation of emitted NO_x. Constraining the model with observed total oxidized reactive nitrogen (NO_y), which approximates NO_x at the time of emission, greatly improves model-observation agreement during this episode, reaffirming NO_x-sensitive conditions in photochemically aged air masses.

ACKNOWLEDGEMENTS

I would like to thank the many collaborators who contributed to this project. The 2019 Carlsbad Caverns Air Quality Study, which provides the data for my analysis, was designed and supervised by Barkley Sive, Bret Schichtel, Tony Prenni, Emily Fischer, and Jeff Collett. Specialized measurements during the field study were collected by Yong Zhou, Amy Sullivan, Lilly Naimie, Katie Benedict, Emily Fischer, Barkley Sive, Julieta Juncosa Calahoranno, and Ilana Pollack. The National Park Service (NPS) contributed ozone and meteorological measurements. Elana Cope helped process the PAN chromatograms. Da Pan performed the VOC source apportionment analysis which this thesis builds upon. A special thank you to Da, Ilana, Emily, and to my advisor, Jeff, for their guidance and insight which helped me piece together the results presented in this work. I would additionally like to thank Jeff, Emily, and Megan Willis for being part of my master's advisory committee. This work is supported by the NPS under Agreement Number P20AC00679 with Colorado State University. The assumptions, findings, conclusions, judgments, and views presented herein should not be interpreted as necessarily representing the NPS. I thank Glenn Wolfe for his publicly available F0AM model and corresponding MATLAB scripts used to process model output, the University of Leeds for providing the MCM v3.3.1, and the NOAA Air Resources Laboratory (ARL) for providing the HYSPLIT transport model. I also thank Erin McDuffie and Jeff Pierce for valuable discussions regarding model configuration.

TABLE OF CONTENTS

LIST OF TABLES

LIST OF FIGURES

Chapter 1

Introduction

1.1 Oil, natural gas, and ozone (O_3) in the US Southwest

Ground-level (O_3) is a secondary air pollutant associated with adverse effects on both human and ecosystem health (Cohen et al., 2017; Monks et al., 2015; Kohut, 2007). O_3 was designated as a criteria pollutant by the US Clean Air Act in 1970, and concentrations are monitored nationwide following protocols set by the US Environmental Protection Agency (EPA). Over the past two decades, concerted efforts to reduce O_3 precursor emissions have resulted in a steady decline in maximum daily 8-h average (MDA8) O_3 concentrations across much of the continental US (Simon et al., 2015; Gaudel et al., 2018). However, certain regions, particularly in the western and central US, have experienced more modest declines or even increasing O_3 trends (Strode et al., 2015; https://www.epa.gov/air-trends/ozone-trends). Figure 1.1 compares the annual fourth-highest MDA8 (4MDA8) O_3 trends since the year 2000. This comparison is made between measurements taken at 826 regulatory monitoring sites across the continental US and those specifically obtained from the US Southwest. Here, "Southwest" refers to the climatic region designated by the National Oceanic and Atmospheric Administration (NOAA), which encompasses Colorado, Utah, Arizona, and New Mexico. This comparison reveals a noticeably less significant trend in O_3 in the Southwest when compared with the rest of the country, such that in most recent years, the 4MDA8 O_3 concentration averaged across the Southwest was still exceeding the 70 parts per billion by volume (ppbv) National Ambient Air Quality Standard (NAAQS).

O_3 concentrations measured at a specific location result from the combination of regional background influence and local production through photochemical reactions involving its precursors, nitrogen oxides (NO_x) and volatile organic compounds (VOCs). In the western US, background O_3 can compose a large faction (30-60 ppbv) of the 70 ppbv NAAQS due to various factors in-

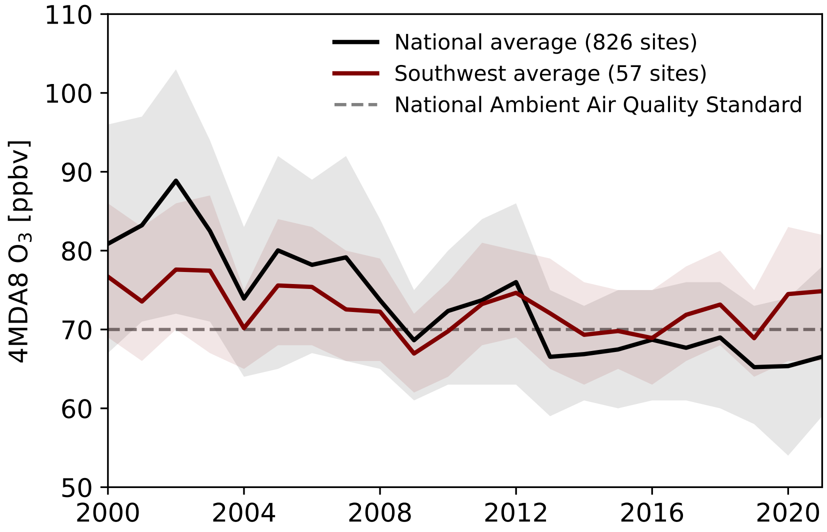

Figure 1.1: Spatially-averaged fourth-highest maximum daily 8-h average (4MDA8) O_3 concentrations between 2000 and 2021. Shading represents the $10^{th}/90^{th}$ percentiles. Measurements are shown for the entire US (average of 826 regulatory monitoring sites), and the US Southwest (average of 57 sites across Colorado, Utah, Arizona, and New Mexico). Data source: https://www.epa.gov/air-trends/ozone-trends.

cluding wildfire emissions, intrusions of stratospheric O_3, and long-range transport of Asian industrial emissions (Jaffe et al., 2022). Local photochemical production of O_3 on top of the regional background can be attributed to NO_x and VOC emissions from both biogenic and anthropogenic sources. While emissions of O_3 precursors from anthropogenic sources like power plants and vehicles have generally declined across the continental US (Simon et al., 2015), recent research indicates an increase in emissions specifically in regions associated with oil and natural gas (O&G) production. For instance, Dix et al. (2020) identified positive trends in nitrogen dioxide (NO_2) tropospheric columns, measured by satellite between 2007–2018, over several US O&G basins (Bakken, Eagle Ford, and Permian), in contrast to declining NO_2 columns over major urban regions. Satellite observations have also revealed recent (e.g., 2017-2019) increases in methane (CH_4) emissions from US O&G basins, which correlate with rising O&G production rates, active well counts, and new well drilling activities (Lu et al., 2023). These top-down CH_4 emission estimates are much larger than reported in emission inventories, suggesting that emissions of other VOCs are likely also underestimated (Francoeur et al., 2021; Dalsøren et al., 2018; Kort et al., 2016; Li et al., 2017).

O&G-related emissions may be contributing to the challenge of reducing O_3, particularly in areas such as the US Southwest (Allen, 2016; Pozzer et al., 2020; Tzompa-Sosa and Fischer, 2021). Since the early 2010s, the US has emerged as the world's largest producer of O&G, largely due to the widespread adoption of "unconventional" O&G extraction technologies such as horizontal drilling and hydraulic fracturing (https://www.eia.gov/todayinenergy/detail.php?id=48756). The states of Texas and New Mexico are at the forefront of O&G production, primarily because they share the Permian basin, which is the largest oil and the second-largest natural gas-producing basin in the US (Robertson et al., 2020). Covering roughly 160,000 km^2 across the two states, the Permian has been the site of extensive O&G activities since the early 20th century. In recent years, however, O&G production from the Permian has accelerated to unprecedented levels: between 2010 and 2021, natural gas and crude oil production rates have multiplied by factors of 4 and 5, respectively, with each new well drilled producing a mean of 960 barrels of oil equivalent per day. Much of this growth in productivity can be attributed to unconventional techniques, exemplified by the mean horizontal well length growing from 120 m in 2010 to over 3000 m in 2021. The Permian currently accounts for over 40% of US crude oil production and 17% of US natural gas production (https://www.eia.gov/todayinenergy/detail.php?id=54079#). Short-term forecasts from the US Energy Information Administration (EIA) predict that Permian O&G productivity will keep increasing steadily through 2024 (https://www.eia.gov/todayinenergy/detail.php?id=60201). A recent report by Enverus, a private O&G data analytics company, suggests that the Permian contains sufficient geologically viable reserves to sustain production through approximately 2040 (https://www.enverus.com/newsroom/quantifying-unproven-inventory-in-the-permian/).

This growth of US O&G production has led to air quality concerns in areas surrounding O&G activities. Of interest to this thesis is Carlsbad Caverns National Park (CAVE), which is located within the New Mexico portion of the Permian basin. Recent observations have revealed more frequent exceedances of the 70 ppbv O_3 NAAQS within the park, prompting investigation into the factors responsible for this increase. The next section (1.2) will describe the photochemical reactions that result in tropospheric O_3 formation. Section 1.3 will delve into the issue of elevated

O_3 at CAVE in more detail, offering a summary of prior research conducted at the site and outlining the objectives of this thesis.

1.2 O_3 formation mechanism

O_3 in the troposphere is formed through a set of nonlinear photochemical reactions involving NO_x, VOCs, and free radical species. The photolysis of NO_2, which occurs at wavelengths shorter than $\sim$420 nm, is the step directly preceding tropospheric O_3 formation:

$$\mathrm{NO_2} + hv \rightarrow \mathrm{NO} + \mathrm{O(^3P)}. \tag{R1}$$

The resulting ground state oxygen atom ($O(^3P)$) reacts with molecular oxygen (O_2) to form O_3:

$$\mathrm{O(^3P)} + \mathrm{O_2} + \mathrm{M} \rightarrow \mathrm{O_3} + \mathrm{M}, \tag{R2}$$

where M is any third body, often N_2 or O_2, that collisionally stabilizes the resulting O_3 molecule. To complete the O_3 formation cycle, NO_2 needs to be re-generated from nitric oxide (NO):

$$\mathrm{NO} + \mathrm{O_3} \rightarrow \mathrm{NO_2} + \mathrm{O_2} \tag{R3}$$

$$\mathrm{NO} + \mathrm{HO_2} \rightarrow \mathrm{NO_2} + \mathrm{OH} \tag{R4}$$

$$\mathrm{NO} + \mathrm{RO_2} \rightarrow \mathrm{NO_2} + \mathrm{RO}. \tag{R5}$$

If R3 follows R1 and R2, an O_3 molecule is consumed, resulting in a null cycle. If NO is instead oxidized by peroxy radicals (R4 and R5), net O_3 formation occurs. Peroxy radicals are primarily sourced from the oxidation of carbon monoxide (CO), CH_4, and non-methane VOCs by the hydroxyl radical (OH):

$$\mathrm{CO} + \mathrm{OH} + \mathrm{O_2} \rightarrow \mathrm{CO_2} + \mathrm{HO_2} \tag{R6}$$

$$\mathrm{RH} + \mathrm{OH} + \mathrm{O_2} \rightarrow \mathrm{RO_2} + \mathrm{H_2O}, \tag{R7}$$

where RH in the reaction above represents any hydrocarbon. Due to their orders-of-magnitude faster reactivity with OH, non-methane VOCs often play a much larger role in the generation of peroxy radicals in polluted environments compared to CO or CH_4. A major summertime pathway to OH formation is the photolysis of O_3 (at wavelengths below $\sim$330 nm), followed by reaction of the excited state oxygen atom ($O(^1D)$) with water:

$$\mathrm{O_3 + hv \rightarrow O_2 + O(^1D)} \tag{R8}$$

$$\mathrm{O(^1D) + H_2O \rightarrow 2\,OH.} \tag{R9}$$

Other radical initiation pathways include the photolysis of carbonyl compounds such as formaldehyde (HCHO), the photolysis of nitrous acid (HONO), and the ozonolysis of alkenes. Depending on both chemical and meteorological conditions, these pathways can be of comparable importance to the $O(^1D)$ + H_2O pathway in certain environments (Akimoto, 2014).

Because peroxy radicals are needed to form NO_2, O_3 formation can be limited by the abundance of both NO_x and VOCs. If NO_x is low relative to VOCs, the O_3 production rate is near-linearly dependent on the NO_x concentration (NO_x-sensitive regime). Each molecule of NO_x can repeatedly cycle between NO and NO_2 until eventually consumed by reaction with OH:

$$\mathrm{NO_2 + OH + M \rightarrow HNO_3 + M.} \tag{R10}$$

NO_x can also be consumed through net organic nitrate formation:

$$\mathrm{NO + RO_2 + M \rightarrow RONO_2 + M} \tag{R11}$$

$$\mathrm{NO_2 + RO_2 + M \rightarrow RO_2NO_2 + M.} \tag{R12}$$

In high NO_x-environments, R10, R11, and R12 can considerably weaken the radical pool, forcing O_3 production to become limited by the rate at which peroxy radicals are produced from R7 (VOC-sensitive regime). Radical species can also be removed from the system through termination reactions that do not involve NO_x:

$$HO_2 + HO_2 \rightarrow H_2O_2 + O_2 \tag{R13}$$

$$HO_2 + RO_2 \rightarrow RO_2H + O_2 \tag{R14}$$

$$RO_2 + R'O_2 \rightarrow \text{products} \tag{R15}$$

$$HO_2 + OH \rightarrow H_2O + O_2. \tag{R16}$$

The chemical transition point between VOC- and NO_x-sensitive regimes depends on whether NO_x-radical reactions (R10, R11, and R12) or radical-radical reactions (R13, R14, R15, and R16) dominate the net rate of radical termination (Kleinman, 2005). When the rates of these two families of termination reactions are approximately equal, O_3 formation can be sensitive to changes in emission of both NO_x and VOCs ("transitional regime"; Sillman and He, 2002; Wang et al., 2019). If NO_x is present in large excess of VOCs and radical-NO_x reactions dominate, a reduction in NO_x emissions can actually enhance O_3 formation (e.g., Nelson et al., 2021).

1.3 O_3 and its precursors at Carlsbad Caverns National Park

Summertime O_3 levels exceeding the 70 ppbv NAAQS have recently become more common at CAVE. CAVE is located within southeastern New Mexico's Eddy County, which, together with neighboring Lea County, presently account for about 30% of the Permian basin's total O&G production (https://www.eia.gov/todayinenergy/detail.php?id=57020). Figure 1.2 shows the location of CAVE relative to active O&G wells in the region. O_3 concentrations have been measured at CAVE by the National Park Service (NPS) for over a decade during warmer months (April-September), with continuous measurements starting in July 2019 (Figure 1.3). These observations show that, starting in 2018, which is around when O&G production from the Permian began to rapidly accelerate, CAVE began to consistently experience days with MDA8 O_3 above 70 ppbv. Notably, there were 21 days with MDA8 O_3 above 70 ppbv in 2022. To place these exceedances in context, O_3 observations at CAVE can be compared to other areas using the O_3 design value (ODV), which is used by the EPA to describe the air quality status of a given site relative to the NAAQS. The ODV is calculated as the three-year running mean of the annual fourth-highest MDA8 value (4MDA8). Based on the observations shown in Figure 1.3, the most recent (2020-2022) ODV at CAVE is 77 ppbv. Note that this value was calculated only for comparison purposes and should not be considered as an official EPA-issued ODV, mainly because the O_3 data set from CAVE has not been filtered for exceptional events (e.g., wildfire smoke, stratospheric intrusion). That said, the CAVE ODV is equivalent to the ODV of the nearby city of Carlsbad, New Mexico (population: 30,000; 40 km northeast of CAVE) and the Dallas-Ft. Worth metro area (population: 7,600,000; 700 km east of CAVE). The ODV at CAVE is 4 ppbv lower than the 81 ppbv ODV for the El Paso-Las Cruces metro area (population: 1,000,000; 180 km west of CAVE). The Los Angeles-South Coast Air Basin (population: 18,000,000) currently holds the highest official ODV in the US, at 113 ppbv (https://www.epa.gov/air-trends/air-quality-design-values).

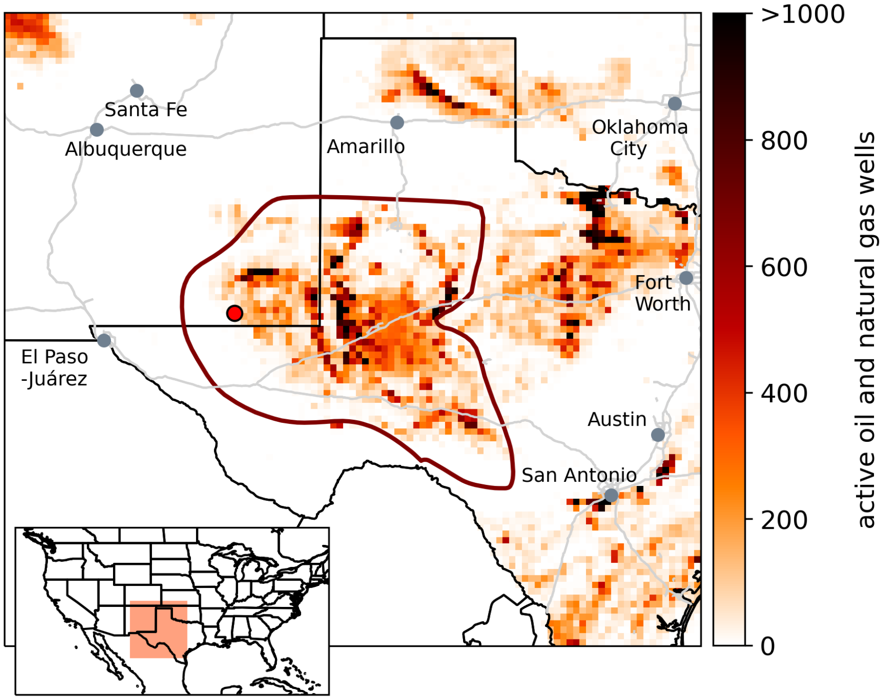

Figure 1.2: Map of active O&G gas wells (gridded to 0.1 × 0.1° resolution) in the western Texas/ southeastern New Mexico study region as of 2019 (https://hifld-geoplatform.opendata.arcgis.com/maps/oil-and-natural-gas-wells). The maroon polygon outlines the Permian basin and the red dot marks the location of CAVE. Gray lines show major highways in the region.

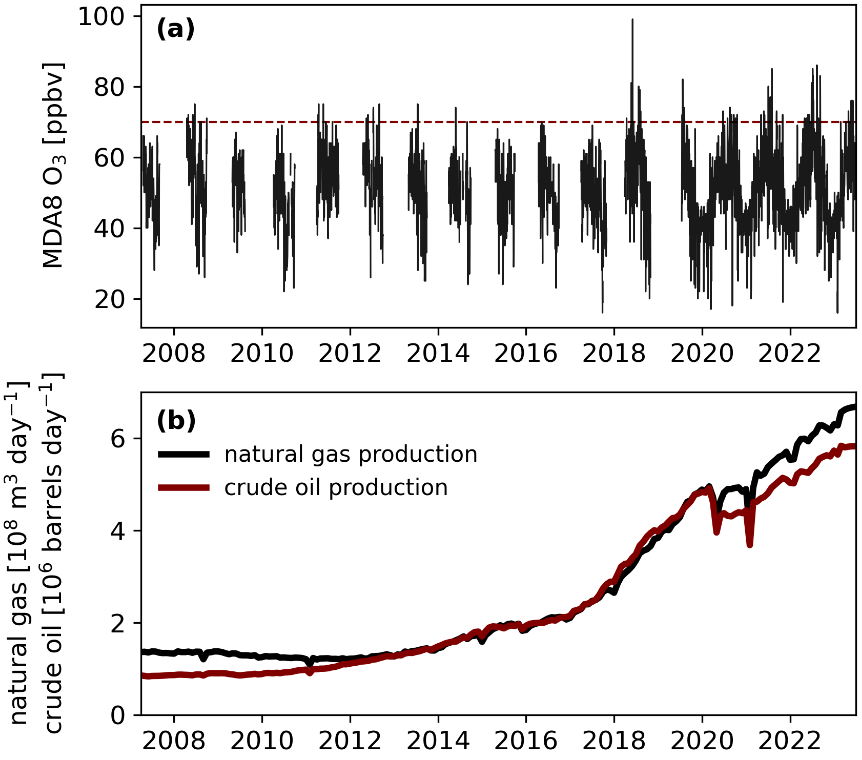

Figure 1.3: (a) MDA8 O_3 measured at CAVE since 2007. The dashed horizontal line marks the 70 ppbv NAAQS. (b) Crude oil and natural gas production rates from the Permian basin over the same period (https://www.eia.gov/petroleum/drilling/).

The 1977 amendments to the Clean Air Act designated CAVE, along with other national parks larger than 24 km^2 (6,000 acres), as Class I federal protected areas (https://www.nps.gov/subjects/air/cleanairact.htm). High O_3 can pose health risks to park staff and visitors, potentially causing respiratory issues such as difficulty breathing, airway inflammation, and the exacerbation of pre-existing lung conditions like asthma, emphysema, and chronic bronchitis (Zhang et al., 2019). Vulnerable groups, such as children and the elderly, are particularly susceptible to these effects. O_3 is also phytotoxic, causing significant foliar injury to sensitive plant populations. Exposure to high O_3 can lead to reduced photosynthesis, premature leaf loss, and increased vulnerability to various environmental stresses (Hogsett et al., 1997; Kohut, 2007). Plant species occurring at CAVE with known O_3 sensitivity include white sagebrush (*Artemisia ludoviciana*), Goodding's willow (*Salix* *gooddingii*), common chokecherry (*Prunus virginiana*), ponderosa pine (*Pinus ponderosa*), and skunkbush sumac (*Rhus trilobata*) (Benck et al., 2017).

Reasons to study O_3 formation at CAVE extend beyond immediate impacts to the national park. The findings of this study are expected to apply to other receptor sites subject to O&G-related emissions from the Permian basin. This includes Texas' Guadalupe Mountains National Park (GUMO), another Class 1 federal protected area 50 km southwest of CAVE, where measured O_3 concentrations correlate closely with those at CAVE (Pollack et al., 2023). Furthermore, a data set of O_3 precursor abundances collected downwind of the Permian can offer insights into how O&G emissions can influence background O_3 on a regional scale. Given the relatively long atmospheric lifetimes of certain O&G-related VOCs (e.g., the lifetime of ethane (C_2H_6) is approximately 2 months in the summer; Helmig et al., 2016), emissions from localized O&G activities have the potential to increase O_3 in downwind regions that do not have their own O&G-related emissions (Pozzer et al., 2020; Tzompa-Sosa and Fischer, 2021).

While high O_3 within or near certain US O&G basins have been extensively studied as a wintertime phenomenon, CAVE experiences elevated O_3 primarily during the summer months. This distinction is important, although it is worth noting that impacts from O&G emissions on summer O_3 have also been observed near the Denver-Julesburg basin in Colorado (McDuffie et al., 2016; Lindaas et al., 2019). Several factors contribute to high summer O_3 at CAVE, including well-established O_3-temperature relationships driven by greater actinic flux, faster reaction rate constants, thermal decomposition of NO_x reservoir species such as peroxyacetyl nitrate (PAN; $CH_3CO_3NO_2$), and increased emissions of biogenic as well as anthropogenic VOCs (e.g., from fuel evaporation; Porter and Heald, 2019; Rubin et al., 2006). Seasonal differences in wind patterns at CAVE also play a role in O_3 levels. During the summer, prevailing southeasterly winds transport O_3 precursors from the Permian basin to the park, while stronger westerly winds in the winter may reduce the influence from O&G emissions (Crosman, 2021; Barkley et al., 2023). In regions like Utah's Uinta basin, high wintertime O_3 has been linked to a shallow planetary boundary layer (PBL) trapping pollutants near the surface, and bright snowpack conditions leading to enhanced radical production from the photolysis of carbonyl compounds (Edwards et al., 2014; Ahmadov et al., 2015). While a recent study reported more pronounced surface CH_4 enhancements in the Permian basin in the wintertime due to a lower PBL (Barkley et al., 2023), CAVE's persistent wintertime westerly winds position it upwind of these emissions. Further, the minimal snowfall in this region suggests that summertime surface albedos are not significantly lower than wintertime albedos, although seasonal variations in humidity may impact the strength of the $O(^1D) + H_2O$ radical production pathway (R9).

CAVE and three other national parks in the US Southwest (Joshua Tree, Grand Canyon and Great Basin) were subject to a VOC sampling study for five months (April-September) in 2017 (Benedict et al., 2020). Whole air samples were collected at various times of day to reveal a substantial influence of O&G emissions on VOC composition at CAVE. The total VOC mixing ratio was approximately 7-10 times greater at CAVE than at the other parks, with the largest contributions coming from light ($< C_5$) alkanes. This screening study lacked high temporal resolution measurements of both NO_x and VOCs needed to comprehensively address O_3 formation in the park, motivating a follow-up study (Carlsbad Caverns Air Quality Study; CarCavAQS) carried out in the summer of 2019. A description of the study site and trace gas instrumentation is provided in Section 2.1 of this thesis. Pan et al. (2023) characterized the sources of VOCs impacting CAVE during CarCavAQS using positive matrix factorization (PMF). Results from this analysis are summarized in Section 2.2. Pollack et al. (2023) used this source apportionment, together with observations of NO_x and peroxy acyl nitrates (PANs), to demonstrate that emissions from O&G activities were the primary drivers of local photochemistry, with consistently high VOC/NO_x ratios implying NO_x-sensitive O_3 production. These studies motivated a detailed model analysis of O_3 photochemistry at CAVE, offering a comparison to prior observational insights.

This thesis presents results from a zero-dimensional (0-D) "box" model constrained to CarCavAQS observations. Box models can effectively simulate radical chemistry with detailed chemical mechanisms and observational constraints, avoiding uncertainties stemming from emission inventories (Cardelino and Chameides, 1995; Kim et al., 2022). These advantages, however, come at the cost of a simplified parameterization of physical processes such as advection and entertainment. Box models have been previously used alongside field observations to study O_3 formation within or near O&G basins, including the Upper Green River (Carter and Seinfeld, 2012, Uinta (Edwards et al., 2013; 2014), and Denver-Julesburg basins (McDuffie et al., 2016) in the US, as well as the Yellow River delta in China (Chen et al., 2020; Lee et al., 2021). The current study represents the first box model analysis constrained to detailed observations of O_3 precursors specific to western Texas /southeastern New Mexico O&G production regions. A description of the model setup is provided in Section 2.3. Key factors driving day-to-day variability in O_3 at CAVE are identified, and the model is used to assess the impact of potential NO_x and VOC emission reductions on O_3 formation (Chapter 3).

Chapter 2

Methods

2.1 Site description and measurements

CarCavAQS was conducted between July 25 and September 5, 2019. This work will focus on the 35-day period between July 30 and September 3, during which speciated VOC measurements were available. Measurements were made from the CAVE Biology Building (32.18°N, 104.44°W; 1335 m elevation), which is 0.5 km from the park visitor center. The site sits on a ridge near the northwestern corner of the Permian basin, $\sim$300 m in prominence above the basin floor. Instrument inlets were positioned 6-7 m above ground level. Trace gas measurements from several different instruments are used in this work, and a brief description of each is provided in the following subsections. More detailed operation and calibration procedures can be found in the cited references.

2.1.1 Real-time gas chromatographic system

C_2-C_{10} hydrocarbons, C_1-C_2 halocarbons, and C_1-C_5 alkyl nitrates ($RONO_2$) were measured with a custom automated five-channel, three-gas chromatograph (GC) analytical system (Pan et al., 2023; Benedict et al., 2019; Abeleira et al., 2017; Sive et al., 2005). The system is equipped with five separator columns and five detectors (three flame ionization detectors (FID), one electron capture detector (ECD), and one mass spectrometric (MS) detector). Ambient samples were collected each hour using a cryogen-free pre-concentrator at -160°C for 5 min at a flow rate of 200 mL min^{-1}, for a total sample volume of 1 L. Calibrations with whole air standards were conducted every 10th sample in the same manner as the ambient samples. The whole air standards were validated using the Colorado State University canister analytical system (Russo et al., 2010; Sive et al., 2005; Swarthout et al., 2015; Zhou et al., 2005). Measurement precisions and method detection limits of all species measured by the GC system were determined from replicate analyses of the whole air standards prior to deployment (Pan et al., 2023).

2.1.2 Proton transfer reaction-mass spectrometer

Isoprene, acetonitrile, and select oxygenated VOCs (OVOCs; acetone, acetaldehyde, methyl ethyl ketone (MEK), and methyl vinyl ketone (MVK)) were measured with a quadrupole proton transfer reaction-mass spectrometer (PTR-MS; model: PTR-MS HS, Ionicon Analytik, Innsbruck, Austria; Pan et al., 2023). Ambient air was continuously sub-sampled at $\sim$2 mL min^{-1} from a $\sim$9.5 mL min^{-1} pumped bypass, and the instrument drift tube pressure and temperature were kept at 2.2 mbar and 45^{o}C, respectively. Ultrapure water was used to produce the H_3O^+ reagent ion source at a flow rate of 6 mL min^{-1} with a discharge current of 4 mA. Calibrations were performed before and after deployment using whole air standards. The accuracy of the standards were < ±5% for all species, and the measurement precision of the PTR-MS was ±10% for individual compounds.

2.1.3 PAN and PPN

Peroxyacetyl nitrate (PAN) and peroxypropionyl nitrate (PPN) were measured with a custom gas chromatograph with electron capture detection (GC-ECD; Pollack et al., 2023; Flocke et al., 2005; Zaragoza et al., 2017). Ambient air was sub-sampled at $\sim$200 mL min^{-1} from a $\sim$9 L min^{-1} pumped bypass. This configuration corresponds to a residence time of 1.2 s, avoiding significant PAN decomposition in the inlet. The instrument analyzed a 1.5 mL sample every 10 minutes using ultrahigh purity (UHP) helium (He) as the carrier gas. A multi-point calibration was performed before and after deployment, and once during deployment. Additional automated calibrations were performed every 4 hours using an acetone photolysis cell and NO calibration gas. The uncertainty of the calibration system was determined to be ±10% prior to deployment, and an on-site detection limit was estimated at 25 pptv.

2.1.4 Carbonyl compounds

C_1-C_7 carbonyl compounds were measured by adsorption of ambient air in sorbent cartridges coated with 2,4-dinitrophenylhydrazine(DNPH; Waters Sep-Pak). Cartridges were collected once per day between 10:00–17:00 local time (LT) at a flow rate of 1.5 L min^3, downstream of an O_3 scrubber. After the campaign, the cartridges were extracted with acetonitrile and resulting samples analyzed with high-performance liquid chromatography with ultraviolet (UV) detection (HPLC-UV; Agilent 1260 Infinity; Fedak et al., 2018). The detection limit for the carbonyl compounds was approximately 0.1 µg m^3.

2.1.5 Gas analyzers, nitric acid, and meteorology

Additional trace gas instruments whose data are used in this work include a Thermo 48C non-dispersive infrared absorption analyzer for CO, a Picarro G2508 cavity ring-down spectrometer for CH_4, and a Thermo 49i UV absorption analyzer for O_3. The O_3 analyzer was coupled with a Thermo 49iPS O_3 reference station for nightly zero, precision, and span checks.

NO_x and total oxidized reactive nitrogen (NO_y) were measured with an Eco Physics CLD 780 TR chemiluminescence NO detector outfitted with custom inlets. NO_2 and NO_y compounds were reduced to NO by a UV (395 nm) photolytic converter and a heated (320°C) molybdenum converter, respectively, both positioned at the inlet tip (Pollack et al., 2023). All three inlet channels (NO, NO_x, and NO_y) were calibrated by standard addition of NO calibration gas to a flow of ultrapure zero air (UZA). NO_2 conversion efficiency was calibrated with gas-phase titration of the NO standard with O_3 produced by UV irradiation of UZA at 185 nm. NO_y conversion efficiency was calibrated by standard addition of nitric acid (HNO_3) generated by a temperature-controlled permeation tube. The permeation tube was validated before and after deployment using the NOAA UV optical absorption system (Neuman et al., 2003). Estimated uncertainty for the NO, NO_2, and NO_y measurements were ±5%, ±10%, and ±15%, respectively. The precision and detection limit of the NO detector was 13 pptv and 50 pptv at 1 Hz, respectively.

Gaseous HNO_3 was collected in 24 h intervals (midnight to midnight) using University Research Glassware (URG) sodium-carbonate-coated annular denuder samplers. After sample collection, the denuders were extracted in deionized water and analyzed by ion chromatography (Dionex DX-500; Naimie et al., 2022). Note that additional inorganic gases (NH_3, SO_2) as well as both organic and inorganic particle-phase constituents were also measured during CarCavAQS. While not a focus of this thesis, these measurements are described in detail in Naimie et al. (2022).

Data from all trace gas instruments except for the carbonyl cartridges and annular denuder samplers was averaged to 1 h intervals to match the sampling frequency of the GC system. The NPS routinely monitors O_3 and standard meteorological parameters (temperature, pressure, relative humidity, solar radiation, wind speed and direction) at CAVE; the rest of the instruments were only deployed during CarCavAQS. O_3 and meteorological data are available for download from the NPS Air Resource Division webpage (https://ard-request.air-resource.com/). Ambient air temperature and relative humidity during the study period ranged from 19 to 40°C (mean = 29°C) and 9 to 83% (mean = 34%), respectively. The North American monsoon significantly influences late summer meteorology at CAVE, typically imposing southeasterly transport over the region. In August 2019, a persistent subtropical ridge situated over southeastern New Mexico weakened monsoonal flow and brought below-average precipitation and above-average temperatures to most of the US Southwest (https://www.weather.gov/psr/SouthwestMonsoon2019Review). During these relatively calm conditions, terrain-driven flows became prominent at CAVE, characterized by daytime southeasterly upslope flows and nighttime northeasterly downslope flows (Crosman, 2021). During CarCavAQS, occasional stronger northwesterly gusts were also observed during both daytime and nighttime (Pan et al., 2023).

2.2 Non-methane VOC source apportionment

Results presented in this thesis build on a source attribution of the CarCavAQS non-methane VOC data set determined using the EPA Positive Matrix Factorization (PMF) v5.0 model (Paatero, 1997). Details on the PMF methodology and solution are described in Pan et al. (2023). Briefly, 47 non-methane VOCs were attributed among seven VOC source factors. Uncertainties of the factor profiles were estimated from 100 bootstrapping runs, the means and medians from which were nearly identical in the PMF solution (Figure 2.1). Among the seven VOC source factors, three were associated with primary O&G emissions. Factor 1 was composed mainly of longer-lived alkanes ($C_2 - C_7$), Factor 2 was composed mainly of shorter-lived alkanes ($C_7 - C_8$), and Factor 3 included $C_8 - C_{10}$ alkanes, ethylbenzene, and xylenes potentially tied to O&G pre-production processes. On average, Factors 1–3 accounted for the majority of the total VOC mixing ratio, showed strong correlations with NO_x and CH_4, and were predominantly associated with the southeast wind sector (the direction of the Permian basin; Pan et al., 2023; Pollack et al., 2023). Of the remaining four factors, two were characterized by OVOCs and $RONO_2$ associated with secondary chemical production (Factors 4 and 5), one included $C_2 - C_4$ alkenes attributed to a mixture of possible combustion sources (Factor 6), and the other was a regional background factor containing halocarbons, acetonitrile, and isoprene (Factor 7). These PMF results serve a dual role in this thesis: to contextualize the variability of VOC sources over the study period and to inform model scenarios with targeted reductions of VOCs from specific emission sources.

2.3 0-D modeling approach

The Framework for 0-D Atmospheric Modeling (F0AM v4.2.2; Wolfe et al., 2016) was used to evaluate the sensitivity of O_3 formation to changes in precursor concentrations. Simulations were initialized with and constrained to observed NO_x, CO, CH_4, and primary VOC concentrations, as well as meteorological inputs (temperature, pressure, and relative humidity). While the representation of physical processes like dilution and entrainment is highly simplified in 0-D “box” models, they serve as valuable tools for sensitivity analyses if simulated levels of unconstrained secondary species such as O_3 and OVOCs are in reasonable agreement with observations. Such agreement indicates that the model appropriately represents the photochemical processes active in oxidant production (Souri et al., 2023).

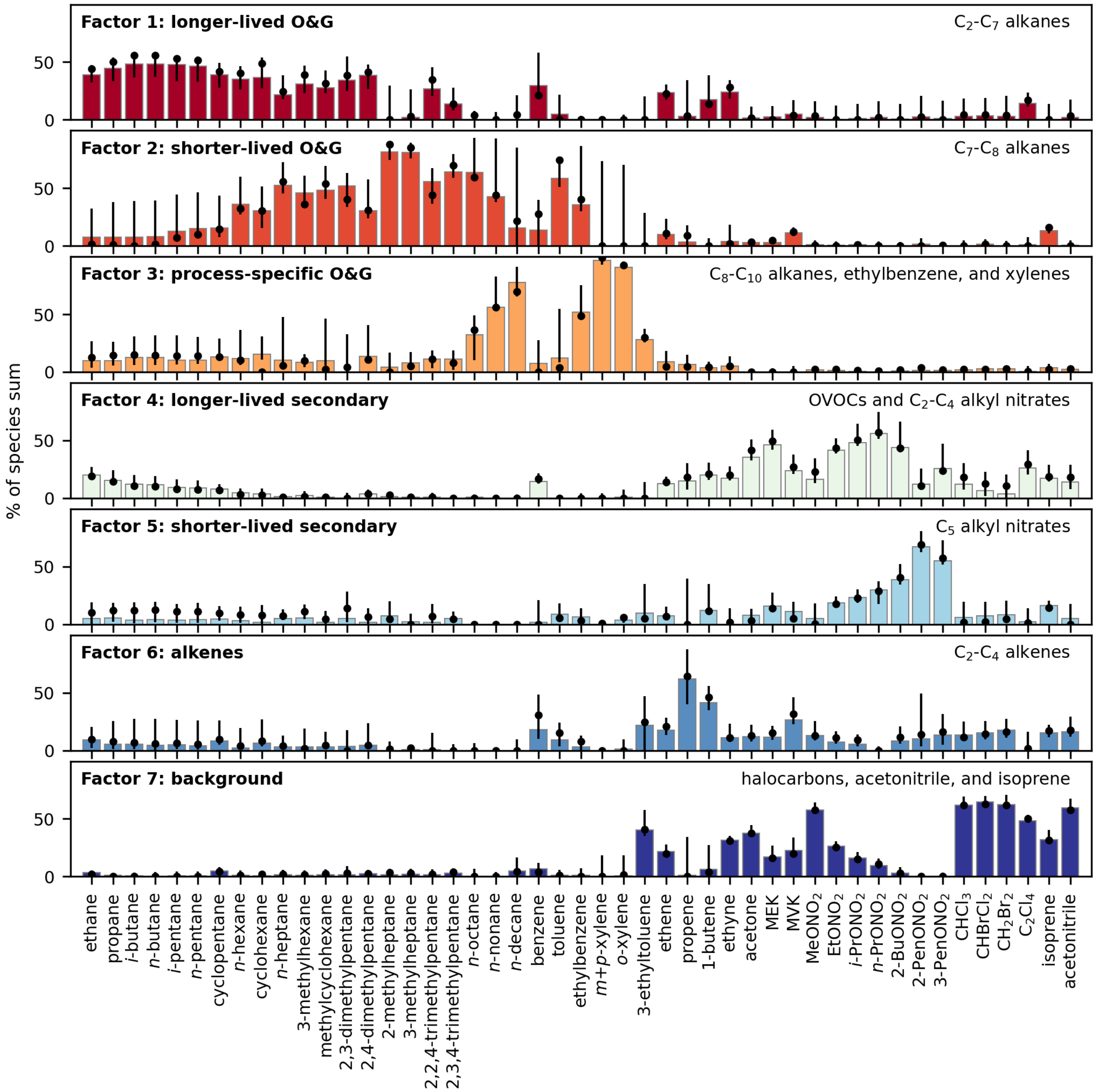

Figure 2.1: Non-methane VOC PMF factor profiles (adapted from Pan et al. (2023)). The bars represent the contributions of the factor to each species, and error bars represent the 25th and 75th percentiles of the contributions from 100 bootstrapping runs. Dots show the means of the bootstrapping runs.

Box models can reasonably capture observed O_3 levels when a large fraction of O_3 at a given site is produced by *in situ* chemistry (Edwards et al., 2013; Edwards et al., 2014; McDuffie et al., 2016; Ninneman and Jaffe, 2021; Xiong et al., 2023). O_3 levels in photochemically aged air masses depleted of NO_x and primary VOCs are likely to be underestimated by a box model as substantial O_3 production occurs far upwind of the location of interest (Xue et al., 2013). In this study, O_3 sensitivity results are based only on CarCavAQS days when photochemically fresh air masses impacted CAVE. Photochemical age was assessed with the NO_x/NO_y ratio, where higher values indicate less aging (Kleinman et al., 2008). Days with hourly NO_x/NO_y ratios exceeding 0.8 were considered influenced by photochemically fresh air masses (Warneke et al., 2007). The ratio calculation was restricted to the morning hours (06:00–10:00 LT) to capture the characteristics of air masses affecting CAVE before substantial PBL expansion and photochemical processing has occurred. Based on this threshold, eleven days during CarCavAQS were selected for O_3 sensitivity analysis using the F0AM model. Other characteristics that distinguish these eleven days from the rest of the campaign are discussed in Section 3.1. Limited model analysis is conducted for a set of high O_3 days influenced by more aged emissions (Section 3.5).

A subset of the Master Chemical Mechanism (MCM v3.3.1; Jenkin et al. 2015) was used for the model chemistry scheme, containing near-explicit gas-phase degradation schemes for CH_4 and 27 primary VOCs, as well as relevant inorganic reactions, yielding a total of 2572 species and 7523 reactions. Data reduction criteria used by Pan et al. (2023) were applied to all VOC observations such that species with long periods of missing data and/or signal-to-noise ratios <0.5 were excluded from the model constraints. This approach reduces uncertainty in the constraints and allows model precursor control strategy scenarios to be directly based on the Pan et al. (2023) CarCavAQS PMF results. 47 of 58 individual VOCs analyzed by the GC system and the PTR-MS met criteria for inclusion (Table 2.1). Among these, 27 are primary VOCs with degradation schemes included in the MCM. The MCM v3.3.1 lacks degradation schemes for 10 measured primary VOCs that meet the data reduction criteria (6 branched alkanes, 2 cyclic alkanes, and 2 halocarbons); these species were "lumped" together with other species that have similar reaction rate coefficients with OH (Table 2.2).

For primary VOC constraints, missing data was filled using a least squares regression of NO_x and measured mixing ratios for all measurement points. We note that while most primary VOCs correlated well with both NO_x and CH_x, correlations with NO_x were slightly stronger on average

(Table 2.2). For species with poor correlations with NO_x and CH_4 (r <0.5), missing data were filled by linear interpolation of the time series. This approach to VOC constraints is sufficient to reproduce observed O_3 concentrations with good accuracy (see Section 3.2). If the data reduction criteria are ignored and the model is instead constrained to 38 measured primary species with included degradation schemes in the MCM, the simulated O_3 mixing ratios exhibit a negligible difference (<1%) compared to the 28 primary species mechanism (Figure 2.2).

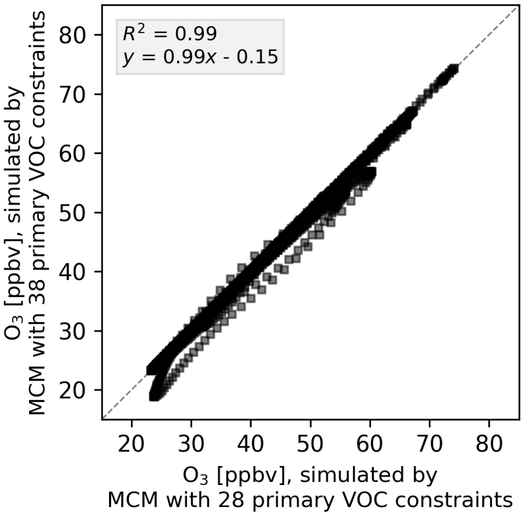

Figure 2.2: Comparison of O_3 concentrations simulated by the MCM with 38 primary VOC constraints (compounds listed with MCM name in Table 2.1 plus CH_4) versus 28 primary VOC constraints (compounds listed as "constrained" in Table 2.2 plus CH_4) across eleven modeled days. The coefficient of determination (R^2) and the linear least-squares fit to the data are included. The dashed line represents a 1:1 fit. The 28 primary VOC constraints are those with measured concentrations that do not include extended periods of missing data and/or low signal-to-noise ratios (Pan et al., 2023), while the 38 primary VOC constraints include all measured species whose degradation schemes are included in MCM v3.3.1. The observed good agreement is primarily due to the fact that most additional VOCs included in the 38 primary species mechanism were frequently at or below their detection limits, resulting in a negligible effect on O_3 formation. All model results presented in this study are derived from simulations employing the 27 primary species mechanism.

O_3 and other measured secondary species (OVOCs, PANs, C_1-C_5 $RONO_2$) were initialized with their observed mixing ratios for the first model time step but not constrained further, leaving them available for model validation. Formaldehyde (HCHO), an important primary radical source, was not measured in real time but instead quantified with daily carbonyl cartridges. An orthogonal distance regression (ODR) between HCHO and acetaldehyde concentrations obtained from all cartridge samples resulted in a ratio of 0.27 ±0.07. This ratio of 0.27 was applied to hourly PTR-MS acetaldehyde data to estimate hourly HCHO concentrations used for model initialization. A similar approach to estimating HCHO concentrations for box model initialization has been employed by McDuffie et al. (2016).

Physical loss by dilution during PBL growth was simulated by applying a first-order loss rate (k_{dil}; 5×10^{-5} s^{-1}, corresponding to a dilution lifetime of $\sim$ 6 h) to all model-calculated species. Background mixing ratios of O_3 and other measured secondary species, estimated from their nighttime (00:00–05:00 LT) averages, were added to the model at the dilution rate to simulate entrainment from the residual layer. The dilution rate was determined by varying k_{dil} to improve model-observation agreement for the observed secondary species. An additional first-order loss rate was added for O_3 to represent dry deposition to the surface, calculated with a typical O_3 dry deposition velocity of 0.8 cm s^{-1} (Finlayson-Pitts and Pitts, 2000) and assuming that diurnal PBL height varies from 300 m at night to 3 km in the afternoon. These PBL heights were chosen based on August 2019 mean values from the Modern-Era Retrospective analysis for Research and Applications (MERRA-2) reanalysis data set (Gelaro et al., 2017).

The observational constraint on NO_x was partitioned by the model into NO and NO_2 at each time step assuming photostationary state. Photolysis rates were calculated as a function of solar zenith angle, elevation, surface albedo, and total O_3 column using lookup tables from the National Center for Atmospheric Research Tropospheric Ultraviolet and Visible (NCAR TUV) radiation model. An albedo of 0.2 was chosen based on the August 2019 monthly mean value over CAVE from MERRA-2, which is consistent with previous airborne albedo measurements over the Chihuhahuan desert (Pelgrum et al., 2000). A total O_3 column of 287 DU was chosen based on mean Ozone Monitoring Instrument (OMI) observations over CAVE in August 2019 (https://www.esrl.noaa.gov/gmd/grad/neubrew/SatO3DataTimeSeries.jsp). To account for deviations from clear-sky conditions, a correction factor scaled by *in situ* pyranometer observations of solar radiation was applied to all calculated photolysis rates (j_{corr}), which improved the model agreement with observed NO/NO_2 ratios. The sensitivity of modeled photochemical O_3 production to the parameters described above is discussed in Section 3.3.

Each simulation was initialized at midnight and integrated forward for 48 h with a time step of 10 min. Following the approach of Mayhew et al. (2022), daily observational constraints were duplicated to provide a 48 h constraint of two repeated periods: the first 24 h period was included for model spin-up and the second 24 h period was considered as the model output. Further simulations showed that modeled O_3 mixing ratios were not affected when using a spin-up period longer than 24 h. Appendix A contains additional notes on model configuration for future use.

2.4 Model-calculated O_3 metrics

Output from the F0AM model was used to calculate several well-established metrics for evaluating O_3 sensitivity. Given that O_3 formation requires the oxidation of NO by peroxy radicals to form NO_2 (R4 and R5), the instantaneous photochemical O_3 production rate ($P(O_3)$) can be calculated as the net rate of O_x (= O_3 + NO_2) production:

$$\begin{aligned} P(\mathrm{O_3}) = {} & k_{\mathrm{HO_2+NO}}[\mathrm{HO_2}][\mathrm{NO}] + \sum k_{\mathrm{RO_{2\mathit{i}}+NO}}[\mathrm{RO_{2\mathit{i}}}][\mathrm{NO}] \\ & - k_{\mathrm{OH+NO_2+M}}[\mathrm{OH}][\mathrm{NO_2}][\mathrm{M}] - P(\mathrm{RONO_2}) - P(\mathrm{RO_2NO_2}) \\ & - k_{\mathrm{OH+O_3}}[\mathrm{OH}][\mathrm{O_3}] - k_{\mathrm{HO_2+O_3}}[\mathrm{HO_2}][\mathrm{O_3}] \\ & - k_{\mathrm{O(^1D)+H_2O}}[\mathrm{O(^1D)}][\mathrm{H_2O}]] - L(\mathrm{alkenes} + \mathrm{O_3}), \end{aligned} \tag{2.1}$$

where *k* terms are the rate coefficients and RO_{2i} are individual organic peroxy radicals. The negative terms in Equation 2.1 represent the rates of O_x loss pathways: the reaction between OH and NO_2 to form HNO_3 (R10), the net production of organic nitrates ($RONO_2$ and $RONO_2$; R11 and R12), the reactions of OH and HO_2 with O_3, the photolysis of O_3 followed by reaction of $O(^1D)$ with water (R9), and alkene ozonolysis reactions. This definition of $P(O_3)$ only includes chemical production and loss terms and thus does not consider physical processes (i.e., surface deposition and advection).

As described in Section 1.2, the chemical transition point between $\mathrm{NO_x}$-sensitive and VOC-sensitive $\mathrm{O_3}$ production regimes depends on whether radical-radical reactions (R13, R14, R15, and R16) or radical-$\mathrm{NO_x}$ reactions (R10, R11, and R12) dominate the net rate of radical termination. The L_N/Q metric can be used to diagnose the instantaneous $\mathrm{O_3}$ production regime, where L_N is the rate of radical loss by reaction with $\mathrm{NO_x}$ and Q is the total radical termination rate (Kleinman, 2005). If L_R is the rate of radical-radical termination reactions, Q is equal to the sum of L_R and L_N:

$$L_N = k_{\mathrm{OH+NO_2+M}}[\mathrm{OH}][\mathrm{NO_2}][\mathrm{M}] + P(\mathrm{RONO_2}) - P(\mathrm{RO_2NO_2}), \tag{2.2}$$

$$\begin{aligned} L_R = {} & k_{\mathrm{HO_2+HO_2}}[\mathrm{HO}]^2 + \sum k_{\mathrm{RO}_{2i}+\mathrm{HO_2}}[\mathrm{RO}_{2i}][\mathrm{HO_2}] + \sum k_{\mathrm{RO}_{2i}+\mathrm{R'O}_{2i}}[\mathrm{RO_2}][\mathrm{R'O_2}] \\ & + k_{\mathrm{HO_2+OH}}[\mathrm{HO_2}][\mathrm{OH}] \end{aligned} \tag{2.3}$$

$$Q = L_N + L_R. \tag{2.4}$$

Model-calculated radical loss rates by the net formation of nitrous acid (HONO), peroxynitric acid ($\mathrm{HO_2NO_2}$), and nitro compounds were negligible compared to the reactions listed in Equation 2.2 and thus are not included in the L_N term. When $L_N > L_R$, or $L_N/Q > 0.5$, the majority of radical termination occurs by reaction with $\mathrm{NO_x}$, and thus $\mathrm{O_3}$ production can be deemed VOC-sensitive. When $L_N/Q < 0.5$, radical-radical termination reactions dominate and $\mathrm{O_3}$ production is $\mathrm{NO_x}$-sensitive. It is important to clarify that the chemical transition point ($L_N/Q = 0.5$) does not necessarily line up with the "policy-relevant" transition point described by Schroeder et al. (2017), at which further additions of $\mathrm{NO_x}$ definitively result in a decline in $P(\mathrm{O_3})$. This is because the amount of OH continues to grow with increasing $\mathrm{NO_x}$ via the $\mathrm{HO_2}$ + $\mathrm{NO_2}$ reaction (R4) even if $L_N/Q > 0.5$. Since the oxidation of VOCs by OH initiates the $\mathrm{O_3}$ formation cycle, $P(\mathrm{O_3})$ continues to rise with increasing OH until $\mathrm{NO_x}$ levels are sufficiently high to result in the net removal of OH via OH + $\mathrm{NO_2}$ (R10). By evaluating the effect of $\mathrm{NO_x}$ on $P(\mathrm{O_3})$ within the F0AM model, the "policy-relevant" transition point corresponding to CarCavAQS observational constraints was found to occur at $L_N/Q \sim 0.62$ (Figure S2).

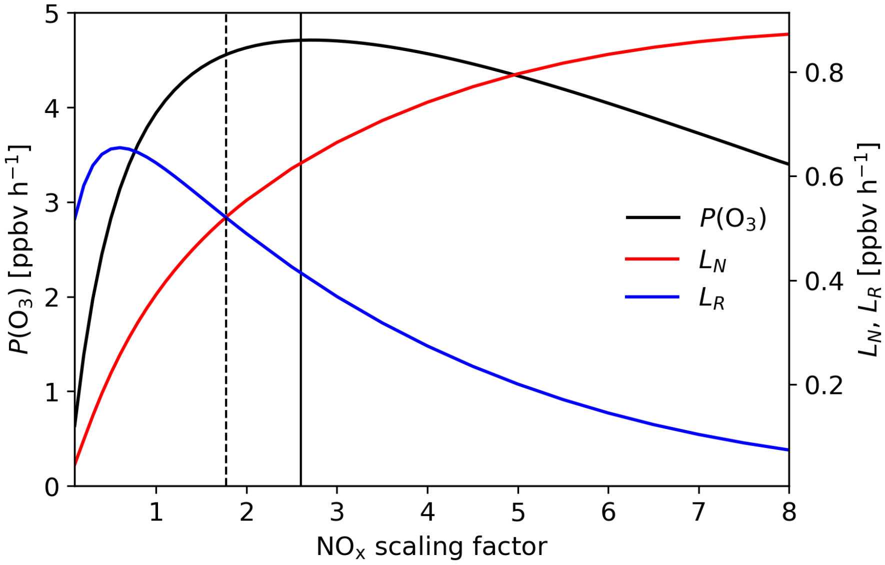

Figure 2.3: Determination of the "policy-relevant" transition point between NO_x-sensitive and VOC-sensitive chemical regimes using the F0AM model. The black trace shows how the daytime (06:00–18:00 LT) mean $P(O_3)$, averaged over eleven modeled days, responds when the observational constraint on NO_x is scaled by a factor of 0.1 to 8. Also shown are L_N (Equation 2.2) and L_R (Equation 2.3) averaged over the same periods. The dashed vertical line marks the chemical transition point (where $L_N = L_R$, or $L_N/Q = 0.5$) and the solid vertical line marks the "policy-relevant" transition point as described by Schroeder et al. (2017), occurring where $P(O_3)$ is maximized. This point corresponds to an L_N/Q value of approximately 0.62.

2.5 HYSPLIT back-trajectories

To examine air mass transport patterns influencing CAVE, back-trajectories were calculated using the NOAA Hybrid Single-Particle Lagrangian Integrated Trajectory model (HYSPLIT; Stein et al., 2015). 12 km horizontal resolution meteorological data from the North American Mesoscale Forecast System (NAM-12) was used. Trajectories were initiated from CAVE at 100 m above model ground level and integrated backwards for 48 h, with a new trajectory initiated every 2 h for the duration of CarCavAQS. Hourly trajectory end points were gridded to a 0.25° × 0.25° horizontal resolution to visualize the most prominent transport patterns on selected groups of days.

Table 2.1: Non-methane VOCs measured at 1 h time resolution by the real-time GC system and PTR-MS during CarCavAQS. Certain species were excluded from the PMF analysis of Pan et al. (2023) due to low signal-to-noise ratios and/or extended periods of missing data. The MCM name is listed for primary VOCs who's degradation schemes are included in MCM v3.3.1.

species	type	instrument	included in Pan et al. (2023) PMF?	MCM name for primary VOCs	k_{OH} (298 K)[1]	reference for k_{OH}
ethane	alkane	real-time GC	yes	C2H6	0.248	Atkinson and Arey (2003)
propane	alkane	real-time GC	yes	C3H8	1.09	Atkinson and Arey (2003)
i-butane	alkane	real-time GC	yes	IC4H10	2.12	Atkinson and Arey (2003)
n-butane	alkane	real-time GC	yes	NC4H10	2.36	Atkinson and Arey (2003)
i-pentane	alkane	real-time GC	yes	IC5H12	3.6	Atkinson and Arey (2003)
n-pentane	alkane	real-time GC	yes	NC5H12	3.8	Atkinson and Arey (2003)
n-hexane	alkane	real-time GC	yes	NC6H14	5.2	Atkinson and Arey (2003)
cyclohexane	alkane	real-time GC	yes	CHEX	6.97	Atkinson and Arey (2003)
cyclopentane	alkane	real-time GC	yes		4.97	Atkinson and Arey (2003)
n-heptane	alkane	real-time GC	yes	NC7H16	6.76	Atkinson and Arey (2003)
n-decane	alkane	real-time GC	yes	NC10H22	11	Atkinson and Arey (2003)
n-nonane	alkane	real-time GC	yes	NC9H20	9.7	Atkinson and Arey (2003)
n-octane	alkane	real-time GC	yes	NC8H18	8.11	Atkinson and Arey (2003)
methylcyclohexane	alkane	real-time GC	yes		9.64	Atkinson and Arey (2003)
2-methylheptane	alkane	real-time GC	yes		9.1	Shaw et al. (2020)
2,2,4-trimethylpentane	alkane	real-time GC	yes		3.34	Atkinson and Arey (2003)
2,3-dimethylpentane	alkane	real-time GC	yes		6.47	Wilson et al. (2006)
2,3,4-trimethylpentane	alkane	real-time GC	yes		6.6	Atkinson and Arey (2003)
2,4-dimethylpentane	alkane	real-time GC	yes		4.77	Atkinson and Arey (2003)
3-methylheptane	alkane	real-time GC	yes		8.57[2]	Stockwell et al. (1997)
3-methylhexane	alkane	real-time GC	yes	M3HEX	7	Sprengnether et al. (2009)
2-methylhexane	alkane	real-time GC	no	M2HEX	6.72	Sprengnether et al. (2009)
ethene	alkene	real-time GC	yes	C2H4	8.52	Atkinson and Arey (2003)
1-butene	alkene	real-time GC	yes	BUT1ENE	31.4	Atkinson and Arey (2003)
propene	alkene	real-time GC	yes	C3H6	26.3	Atkinson and Arey (2003)
cis-2-pentene	alkene	real-time GC	no	CPENT2ENE	65	Atkinson and Arey (2003)
1-hexene	alkene	real-time GC	no	HEX1ENE	37	Atkinson and Arey (2003)
ethyne (acetylene)	alkyne	real-time GC	yes	C2H2	0.88	Atkinson and Aschmann (1984)
benzene	aromatic	real-time GC	yes	BENZENE	1.22	Atkinson and Arey (2003)
toluene	aromatic	real-time GC	yes	TOLUENE	5.63	Atkinson and Arey (2003)
ethylbenzene	aromatic	real-time GC	yes	EBENZ	7	Atkinson and Arey (2003)
m+*p*-xylene	aromatic	real-time GC	yes	MXYL, PXYL	18.7[3]	Atkinson and Arey (2003)
o-xylene	aromatic	real-time GC	yes	OXYL	13.6	Atkinson and Arey (2003)
styrene	aromatic	real-time GC	no	STYRENE	58	Atkinson and Arey (2003)
i-propylbenzene	aromatic	real-time GC	no	IPBENZ	6.3	Atkinson and Arey (2003)
n-propylbenzene	aromatic	real-time GC	no	PBENZ	5.8	Atkinson and Arey (2003)
2-ethyltoluene	aromatic	real-time GC	no	OETHTOL	11.9	Atkinson and Arey (2003)
3-ethyltoluene	aromatic	real-time GC	yes	METHTOL	18.6	Atkinson and Arey (2003)
4-ethyltoluene	aromatic	real-time GC	no	PETHTOL	11.8	Atkinson and Arey (2003)
trichloromethane	halocarbon	real-time GC	yes	CHCL3	0.103	Taylor et al. (1993)
bromodichloromethane	halocarbon	real-time GC	yes		0.167	Orkin et al. (2013)
dibromomethane	halocarbon	real-time GC	yes		0.12	Orlando et al. (1996)
tetrachloroethene	halocarbon	real-time GC	yes	TCE	0.151	Tichenor et al. (2001)
α-pinene	terpene	real-time GC	no	APIN	52.3	Atkinson and Arey (2003)
β-pinene	terpene	real-time GC	no	BPIN	74.3	Atkinson and Arey (2003)
isoprene	isoprene	PTR-MS	yes	C5H8	100	Atkinson and Arey (2003)
acetonitrile	nitrile	PTR-MS	yes		0.024	Hynes and Wine (1991)
acetone	OVOC	PTR-MS	yes	CH3COCH3[4]	0.17	Atkinson and Arey (2003)
methyl ethyl ketone	OVOC	PTR-MS	yes	MEK[4]	1.22	Atkinson and Arey (2003)
methyl vinyl ketone	OVOC	PTR-MS	yes	MVK[4]	20	Atkinson and Arey (2003)
acetaldehyde	OVOC	PTR-MS	no	CH3CHO[4]	15	Atkinson and Arey (2003)
methyl nitrate	alkyl nitrate	real-time GC	yes		0.023	Atkinson and Arey (2003)
ethyl nitrate	alkyl nitrate	real-time GC	yes		0.18	Atkinson and Arey (2003)
i-propyl nitrate	alkyl nitrate	real-time GC	yes		0.29	Atkinson and Arey (2003)
n-propyl nitrate	alkyl nitrate	real-time GC	yes		0.58	Atkinson and Arey (2003)
2-butyl nitrate	alkyl nitrate	real-time GC	yes		0.86	Atkinson and Arey (2003)
2-pentyl nitrate	alkyl nitrate	real-time GC	yes		1.7	Atkinson and Arey (2003)
3-pentyl nitrate	alkyl nitrate	real-time GC	yes		1	Atkinson and Arey (2003)

[1] Unit: 10^{-12} cm^3 molecule^{-1} s^{-1}. [2] Rate coefficient estimated by Stockwell et al. (1997) using structure-reactivity relationships. [3] Average of rate coefficients for *m*- and *p*- isomers. [4] Although these oxygenated VOC (OVOCs) can be treated as primary VOCs in the MCM (http://chmlin9.leeds.ac.uk/MCMv3.3.1/roots.htt), in this study they are mainly considered as secondary species.

Table 2.2: Model treatment of primary non-methane VOCs included in the PMF analysis of Pan et al. (2023). Several species not included in the MCM v3.3.1 were lumped together with other species that have similar rate coefficients with OH (k_{OH}). Acetonitrile was not constrained because the MCM does not include nitrile oxidation chemistry. Missing data for the primary VOC constraints was filled using a least squares regression of NO_x and measured mixing ratios for all measurement points (if the Pearson's correlation coefficient (r) was greater than 0.5). The r value of each VOC with CH_4 is also listed to show that most VOCs were better correlated with NO_x. Data gaps for species poorly correlated with NO_x were filled by linear interpolation of the time series.

species	k_{OH} (298 K)[1]	model treatment	r with CH_4	r with NO_x	slope with NO_x	intercept with NO_x
ethane	0.248	constrained	0.76	0.74	6.065	6.105
propane	1.09	constrained	0.76	0.76	6.539	2.67
i-butane	2.12	constrained	0.75	0.77	1.153	0.341
n-butane	2.36	constrained	0.75	0.78	3.361	0.766
i-pentane	3.6	constrained	0.75	0.78	0.992	0.138
n-pentane	3.8	constrained	0.75	0.78	1.203	0.103
n-hexane	5.2	constrained	0.73	0.78	0.447	-0.092
cyclohexane	6.97	constrained	0.73	0.79	0.194	-0.023
cyclopentane	4.97	lumped with *n*-hexane	0.72	0.79	0.062	0.011
n-heptane	6.76	constrained	0.71	0.77	0.177	-0.071
n-decane	11	constrained	0.56	0.62	0.002	-0.002
n-nonane	9.7	constrained	0.64	0.7	0.012	-0.009
n-octane	8.11	constrained	0.68	0.76	0.056	-0.036
methylcyclohexane	9.64	lumped with *n*-nonane	0.7	0.78	0.197	-0.08
2-methylheptane	9.1	lumped with *n*-nonane	0.71	0.79	0.059	-0.026
2,2,4-trimethylpentane	3.34	lumped with *i*-pentane	0.69	0.76	0.061	-0.023
2,3-dimethylpentane	6.47	lumped with 3-methylhexane	0.72	0.79	0.071	-0.017
2,3,4-trimethylpentane	6.6	lumped with *n*-heptane	0.67	0.75	0.015	-0.008
2,4-dimethylpentane	4.77	lumped with *n*-hexane	0.69	0.74	0.022	-0.004
3-methylheptane	8.57	lumped with *n*-octane	0.7	0.78	0.028	-0.014
3-methylhexane	7	constrained	0.72	0.79	0.108	-0.027
ethene	8.52	constrained	0.7	0.77	0.066	0.093
1-butene	31.4	constrained	0.44	0.41		
propene	26.3	constrained	0.54	0.54	0.009	0.034
ethyne	0.88	constrained	0.68	0.68	0.037	0.079
benzene	1.22	constrained	0.7	0.72	0.066	0.047
toluene	5.63	constrained	0.69	0.74	0.076	-0.033
ethylbenzene	7	constrained	0.65	0.74	0.004	-0.002
m+*p*-xylene	18.7[2]	constrained[3]	0.53	0.65	0.009	-0.006
o-xylene	13.6	constrained	0.52	0.65	0.003	-0.002
3-ethyltoluene	18.6	constrained	0.23	0.28		
trichloromethane	0.112	constrained	0.22	0.13		
bromodichloromethane	0.167	lumped with tetrachloroethene	0.3	0.32		
dibromomethane	0.12	lumped with trichloromethane	0.32	0.31		
tetrachloroethene	0.151	constrained	0.48	0.41		
isoprene	100	constrained	0.58	0.63	0.019	0.074

[1] Unit: 10^{-12} cm^3 $molecule^{-1}$ s^{-1}. See Table 2.1 for rate coefficient references. [2] Average of rate coefficients for *m*- and *p*- isomers. [3] Assumed 50% split between *m*- and *p*- isomers.

Chapter 3

Results and discussion

3.1 Variability in O_3 and its precursors during CarCavAQS

Observations at CAVE during summer 2019 revealed significant day-to-day variability in O_3 and its precursors. Hourly O_3 mixing ratios surpassed 70 ppbv on 7 days between July 30 and September 3, although those days did not always align with elevated NO_x and VOCs (Figure 3.1). This variability is addressed by separating the 35 days of CarCavAQS into three distinct groups: photochemically fresh/O&G-influenced (abbreviated as fresh/O&G), photochemically aged/O&G-influenced (aged/O&G), and photochemically aged/background (aged/bkg). The criteria used to determine these groups are listed in Table 3.1. As discussed in Section 2.3, the NO_x/NO_y ratio was used to infer photochemical age, and eleven days with maximum morning NO_x/NO_y >0.8 were deemed appropriate for O_3 sensitivity analysis using the F0AM model. These eleven days fall into the fresh/O&G group, and represent days when emissions in the surrounding region (including the Permian basin) account for a large portion of photochemical O_3 production. Days with lower NO_x/NO_y (aged/O&G and aged/bkg groups) represent periods of longer-range transport of O_3 and its precursors from upwind emission sources.

Table 3.1: Criteria used to categorize the 35 CarCavAQS days based on photochemical age and emission influence.

group	number of days	maximum morning NO_x/NO_y	median *i*-/*n*-pentane	mean daily maximum 1-h O_3 (ppbv)	mean daily maximum 8-h O_3 (ppbv)
photochemically fresh/ O&G-influenced (fresh/O&G)	11	> 0.8	< 1	64	58
photochemically aged/ O&G-influenced (aged/O&G)	21	< 0.8	< 1	66	60
photochemically aged/ background (aged/bkg)	3	< 0.8	> 1	53	50

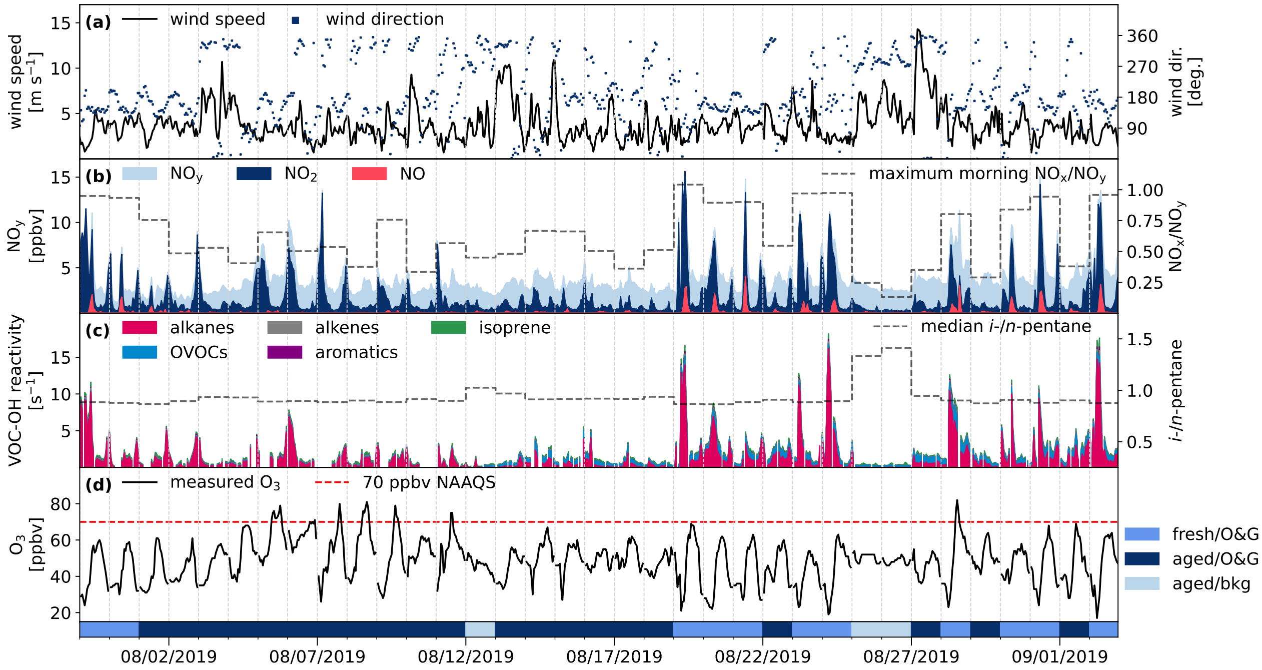

Figure 3.1: Time series of (a) wind speed and direction, (b) NO_y, NO_2, NO, and the maximum morning NO_x/NO_y ratio (calculated between 06:00 and 10:00 LT), (c) contributions of measured VOCs to OH reactivity (grouped by VOC type; Table 2.1) and the daily median *i*-/*n*-pentane ratio, and (d) O_3 mixing ratios observed during CarCavAQS. The colored bars at the bottom panel show which days are grouped together based on photochemical age and emission influence (see text). Ticks on the x-axis are at midnight local time.

The aged/bkg group was further distinguished from the fresh/O&G and aged/O&G groups based on influence from different emission sources, as indicated by the *i*-/*n*-pentane ratio. The *i*-/*n*-pentane ratio has proven to be a reliable indicator for distinguishing between O&G-influenced and urban/vehicle emissions, since *n*-pentane is typically the more prevalent isomer found in natural gas, and the opposite is true for gasoline (Riaz et al., 2011; McGaughey et al., 2004). Therefore, *i*-/*n*-pentane below one is usually associated with O&G influence while ratios of two or more are associated with traffic or other fossil fuel combustion sources. This ratio is independent of photochemical age since both isomers have similar photooxidation lifetimes (Gilman et al., 2013; Swarthout et al., 2013). Both pentane isomers were tightly correlated across the campaign (R^2 = 0.99), with an ODR slope of 0.88, indicating a persistent influence from O&G emissions. However, some variability in *i*-/*n*-pentane was observed at low total VOC mixing ratios. Three days, categorized into the aged/bkg group, had a median *i*-/*n*-pentane above one, which represents background (non-O&G) emissions sources. Days part of the aged/bkg group were also characterized by the lack of a clear morning rise in O_3 and a less pronounced morning-to-afternoon decline in NO_x/NO_y, indicating less active photochemistry than during fresh/O&G and aged/O&G days (Figure 3.2).

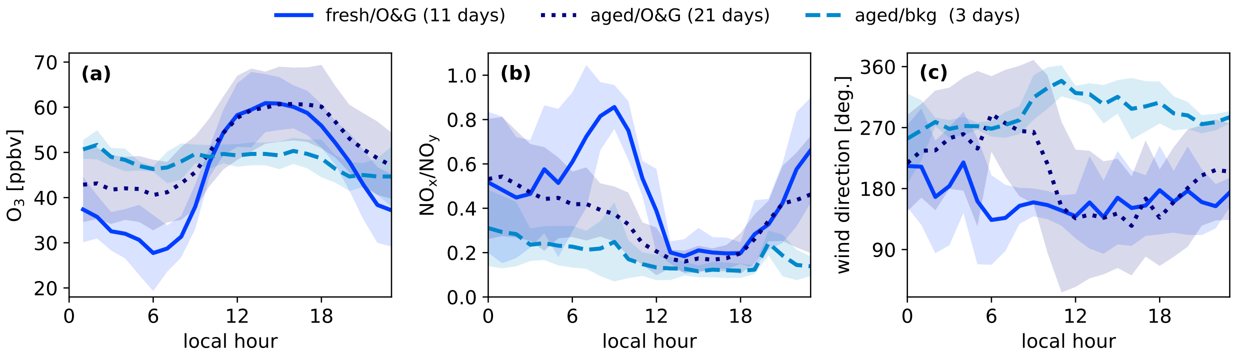

Figure 3.2: Comparison of diurnal variations in measured (a) O_3, (b) NO_x/NO_y, and (c) wind direction across the three groups of CarCavAQS days. The lines show the mean in 1 h bins and the shading represents ± 1 standard deviation.

Distinct diurnal wind direction patterns were observed among the three groups of days (Figure 3.2c). Fresh/O&G days were characterized by primarily southerly/southeasterly winds (the direction of the Permian basin). In contrast, aged/O&G days exhibited a shift in wind direction from westerly/northwesterly in the morning to southeasterly in the afternoon. Aged/bkg days consistently experienced westerly/northwesterly winds throughout the entire day. Wind speeds during aged/bkg days were slightly higher (mean ± 1 standard deviation: 4.3 ± 1.9 m s^{-1}) than both fresh/O&G (3.1 ± 1.3 m s^{-1}) and aged/O&G (3.6 ± 2.3 m s^{-1}) days (campaign-wide mean: 3.5 ± 2.0 m s^{-1}). The observed wind direction patterns indicate variable source influences, and this is further supported by 48 h HYSPLIT back-trajectories. Air masses during fresh/O&G days were predominantly transported from the south/southeast, directly over the Permian basin Figure 3.3a). During aged/O&G days, trajectories displayed more variability but still with substantial transport over the Permian Figure 3.3b). In contrast, aged/bkg days were characterized by exclusively westerly/northwesterly transport and greatly reduced O&G influence (Figure 3.3c). Note that in the case of fresh/O&G days and especially aged/O&G days, occasional longer-range transport patterns suggest a possible influence from other O&G basins besides the Permian, including the Eagle Ford and Barnett shale formations in Texas, as well as the Anadarko basin in Oklahoma.

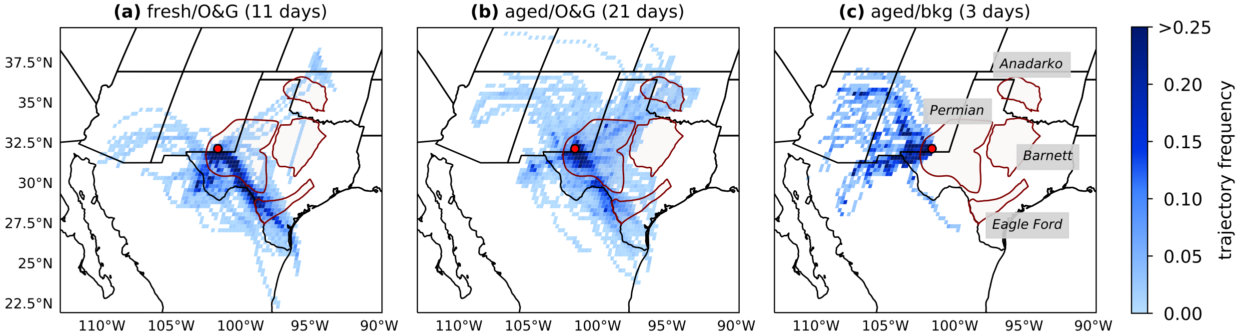

Figure 3.3: Comparison of 48 h HYSPLIT back-trajectory frequencies across the three groups of CarCavAQS days. A new trajectory was initiated from CAVE every 2 h using NAM-12 meteorology. Trajectory frequency is defined as the number of hourly trajectory endpoints within a 0.25 × 0.25° grid cell divided by the total number of trajectories for each group. The red dot represents the location of CAVE, and the maroon polygons outline major O&G basins in the region (https://www.eia.gov/maps/maps.htm).

Figure 3.4 highlights several key differences among the three groups of days in terms of their 24-h mean NO_y and VOC-OH reactivity budgets. It is clear that the observed variability is directly influenced by the differences in photochemical age and emission sources discussed above. NO_x accounted for 58%, 38%, and 20% of 24-h mean NO_y for fresh/O&G, aged/O&G, and aged/bkg days, respectively. Mean ratios of PAN to HNO_3, two NO_x oxidation products, were similar for the fresh/O&G (0.54) and aged/O&G days (0.50), but much lower for the aged/bkg days (0.18). While PAN is efficiently produced from the oxidation of O&G-related VOCs, its lifetime at temperatures observed during CarCavAQS was limited to $\sim$ 1 h (Pollack et al., 2023). Dry and wet deposition are the primary removal processes for HNO_3, giving it a longer lifetime on the order of several days (Trainer et al., 1993). Lower PAN/HNO_3 on aged/bkg days further emphasizes the lack of influence from fresh photochemistry. Additionally, the fraction of NO_y not accounted for by individually measured NO_y compounds (labeled as "remaining NO_z" in Figure 3.4, where $NO_z = NO_y - NO_x$) is largest in the aged/bkg group and smallest in the fresh/O&G group. This gap in the NO_y budget aligns with earlier study findings and is often attributed to organic nitrates and particulate nitrate species not measured individually (Fahey et al., 1986; Day et al., 2003). Regardless of the exact composition, these compounds are expected to form more as the photochemistry proceeds over time (Bertman et al., 1995; Zare et al., 2018).

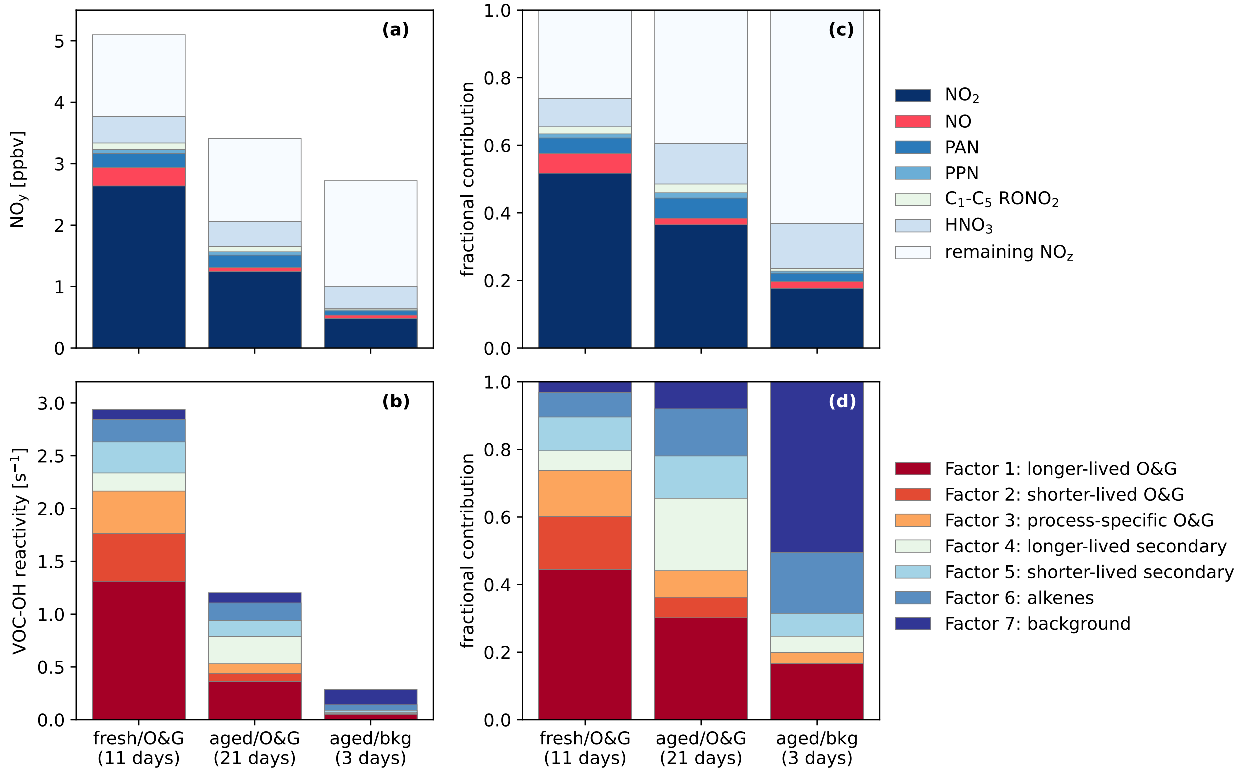

Figure 3.4: Comparison of 24-h mean budgets of (a) measured NO_y compounds and (b) contributions of PMF factors to calculated VOC-OH reactivity across the three groups of CarCavAQS days. Panels (c) and (d) show normalized fractional contributions for NO_y and VOC-OH reactivity, respectively.

The VOC-OH reactivity was calculated as:

$$\mathrm{VOC{-}OH\,reactivity} = k_{\mathrm{OH+X}}[\mathrm{OH}][\mathrm{X}] \tag{3.1}$$

where $k_{\mathrm{OH+X}}$ is the rate coefficient of species X with OH at 298 K, and [X] is the species concentration. Rate coefficients for VOC-OH reactivity calculations are listed in Table 2.1. VOC-OH reactivity is a useful metric for helping assess the potential of a given VOC (or group of VOCs) to contribute to O_3 formation, since the oxidation of VOCs by OH is often the rate-limiting step in the O_3 formation cycle (Gilman et al., 2013; Abeleira et al., 2017; Benedict et al., 2020). Applying this metric to the PMF factor profile helps approximate the relative importance of each factor as a source of O_3 precursors, which may not be evident solely by examining VOC concentrations (Pan et al., 2023). Fresh/O&G days exhibited the largest contributions from the three O&G-related PMF factors to the calculated VOC-OH reactivity budget. Factors 4 and 5, consisting mainly of secondary species formed during photochemical aging, exhibited large contributions on aged/O&G days. Factor 7 (background) was the largest contributor to VOC-OH reactivity on aged/bkg days.

Only three measured OVOCs (acetone, MEK, and MVK) met the data reduction criteria for inclusion in the PMF analysis of Pan et al. (2023), and therefore the contribution of Factors 4 and 5 should be considered as a lower limit of the true contribution of secondary species to total VOC-OH reactivity. Acetaldehyde (measured by the PTR-MS), together with HCHO, propionaldehyde, butyraldehyde, hexaldehyde, and benzaldehyde (measured by the carbonyl cartridges) contributed approximately 1.1, 1.3, and 0.4 s^{-1} of additional daily mean VOC-OH reactivity to fresh/O&G, aged/O&G, and aged/bkg days, respectively (Figure 3.5). Details on how these contributions were estimated are provided below.

Acetaldehyde was measured at an hourly time resolution by the PTR-MS but not included in the PMF analysis of Pan et al. (2023) due to extended periods of missing data. To provide a continuous time series, acetaldehyde data gaps were filled based on linear regression with PTR-MS acetone data (the two species were strongly correlated; $r = 0.90$; Figure B.1). Hourly time series of other OVOCs measured by the carbonyl cartridges were estimated in a similar way as was done for HCHO (described in Section 2.3). Specifically, ratios of OVOCs with acetone, acetaldehyde, and MEK were first calculated from all the cartridge samples. These ratios were then applied to PTR-MS acetone, acetaldehyde, and MEK data depending on which correlation was stronger (Figures B.2, B.3, and B.4). This process provided hourly time series of HCHO, propionaldehyde, butyraldehyde, hexaldehyde, and benzaldehyde in addition to the OVOCs measured by the PTR-MS. VOC-OH reactivity from these species was then calculated per Equation 3.1 (with rate coefficients at 298 K from Atkinson and Arey (2003)) and the 24-h contributions were compared among the three groups of CarCavAQS days (Figure 3.5).

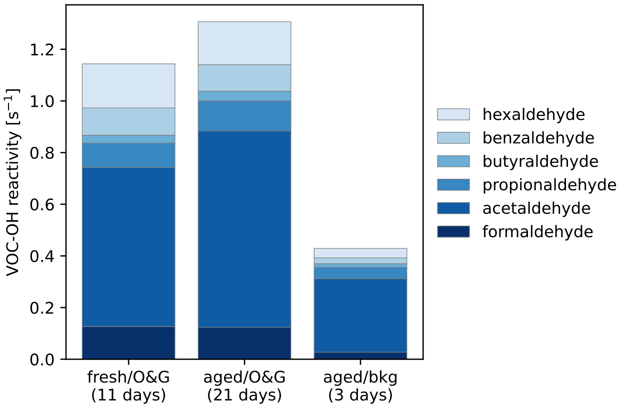

Figure 3.5: Estimated 24-h mean contributions of secondary VOCs not part of the PMF to VOC-OH reactivity across the three groups of CarCavAQS days.

The following three sections examine F0AM box model performance and O_3 production sensitivity on fresh/O&G days. High O_3 days part of the aged/O&G group are examined in Section 3.5. Given the apparent lack of photochemical O_3 formation, aged/bkg days will not be a focus of this thesis.

3.2 Model validation on photochemically fresh days

Figure 3.6 compares O_3, NO_2, and NO simulated by the F0AM box model with observed concentrations for the eleven fresh/O&G days. The model effectively captures day-to-day variations in maximum O_3, reflecting its responsiveness to changing precursor abundances and meteorological conditions used as model constraints. Simulated O_3 concentrations, however, peak slightly earlier in the day and decline more rapidly in the afternoon compared to observations. This is likely due to the application of a constant dilution factor, which does not fully encapsulate the diurnal evolution of PBL mixing processes (Kaser et al., 2017; Lin et al., 2008). The model effectively partitions the observational constraint on NO_x between NO and NO_2, indicating that photolysis rates and O_3 concentrations—the main drivers of the NO/NO_2 ratio—are adequately simulated. One exception is an underestimation of a short peak in NO observed on the afternoon of 8/28/2019. This NO peak, which lasted for ∼ 10 min but was strong enough to elevate the hourly NO average (1 min NO peaked at 66 ppbv), suggests CAVE was briefly impacted by a very fresh plume that had not yet reached photostationary state, and thus the model incorrectly considers most of the NO_x as NO_2.

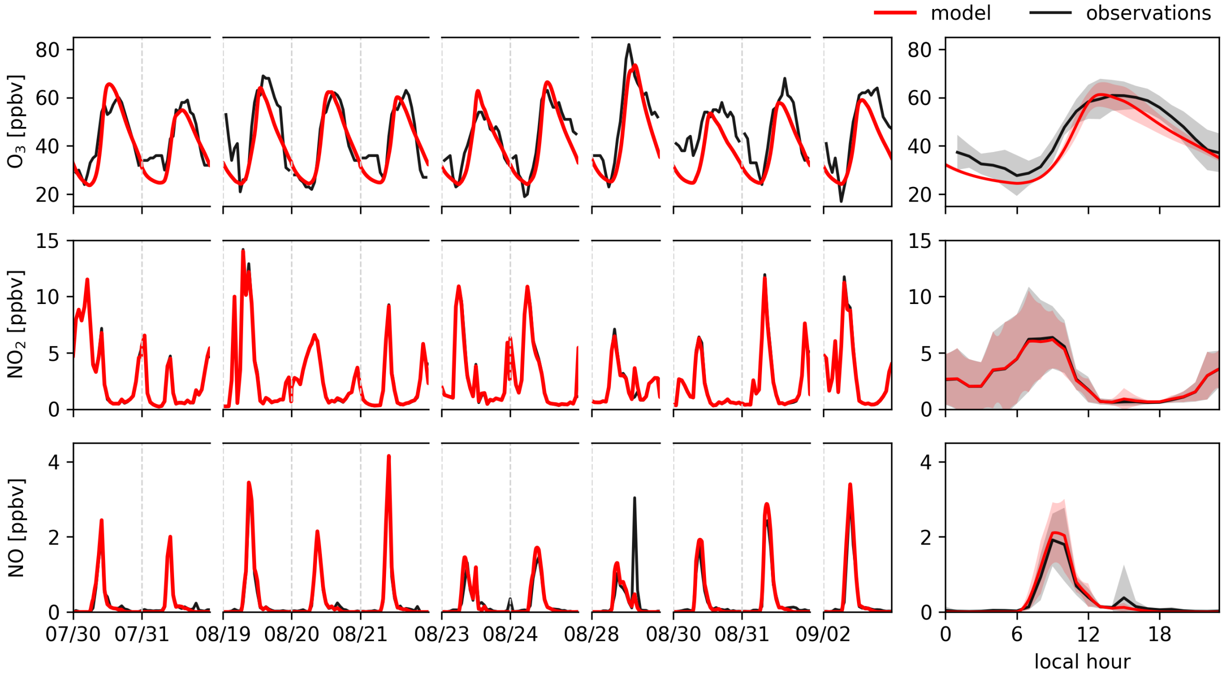

Figure 3.6: Comparison of observed O_3, NO_2, and NO concentrations with those simulated by the F0AM box model as time series and diurnal mean with shading representing ± 1 standard deviation.

Figures 3.7 and 3.8 show model-observation comparisons of unconstrainted secondary VOCs, including PAN, PPN, acetone, acetaldehyde, MEK, and MVK and $C_1 - C_5$ $RONO_2$. The model performs well in regard to simulating the daily photochemical production of these species, although day-to-day discrepancies between the modeled and observed peak concentrations exist, most notably on 8/28/2019. The underestimation of secondary species on this day suggests that a portion of the observed concentrations was not formed locally. Additional VOC precursors to these compounds may also be missing from our observational constraints. Previous box modeling studies have found that constraining OVOCs improves model-observation agreement for PAN, which is expected given that these compounds serve as immediate PAN precursors (Xu et al., 2021; Souri et al., 2023) All OVOCs were left unconstrained within the model due to the significant role that OVOC photolysis can play as a primary source of radicals (Edwards et al., 2014; Wang et al., 2022). Imposing observational constraints on OVOCs could potentially lead to unrealistic radical abundances in model scenarios where primary VOC constraints are reduced from their observed levels. In general, the observed variance in all unconstrained species shown in Figures 3.6, 3.7, and 3.8 is well-captured by the model (median $R^2 = 0.65$; Figure B.5), indicating that *in situ* gas-phase photochemistry at CAVE is reasonably represented. Model deviation from observed concentrations can be attributed to various sources of error associated with box models, including the simplified representation of physical processes, errors in the chemical mechanism, errors in the measurements used as model constraints, and the lack of inclusion of heterogeneous processes that may alter radical abundances (Mao et al., 2013; Song et al., 2022).

A series of tests were carried out to assess the model's sensitivity to select unmeasured parameters described in Section 2.3, including dilution, background O_3, surface albedo, total O_3 column, photolysis rates, initial (midnight) HCHO mixing ratios, and O_3 deposition velocity. Each parameter was independently varied by ± 10%, and the resulting maximum O_3 and daytime mean $P(O_3)$ values were compared with the base case simulation (Table 3.2). These tests showed that simulated O_3 was relatively stable with respect to modest changes in the parameters listed above. The dilution loss rate (k_{dil}) in the base case simulation was tuned to improve model-observation agreement for the observed secondary species—an approach shared by previous box modeling studies (e.g., McDuffie et al., 2016; Ninneman and Jaffe, 2021; Rickly et al., 2023). A +10% / -10% change in k_{dil} impacted maximum O_3 by -1.52 ppbv / 0.36 ppbv or -2.45% / 0.58%. Among all parameters tested, the photolysis rate correction factor (j_{corr}), which is dynamically scaled by *in situ* observations of solar radiation, had the largest effect on both maximum O_3 (5.38% / -7.30%) and $P(O_3)$ (9.65% / 14.15%). While direct measurements of photolysis rates were unavailable, we have confidence that our method of scaling TUV clear-sky calculations is appropriate given the strong model-observation agreement for the NO/NO_2 ratio.

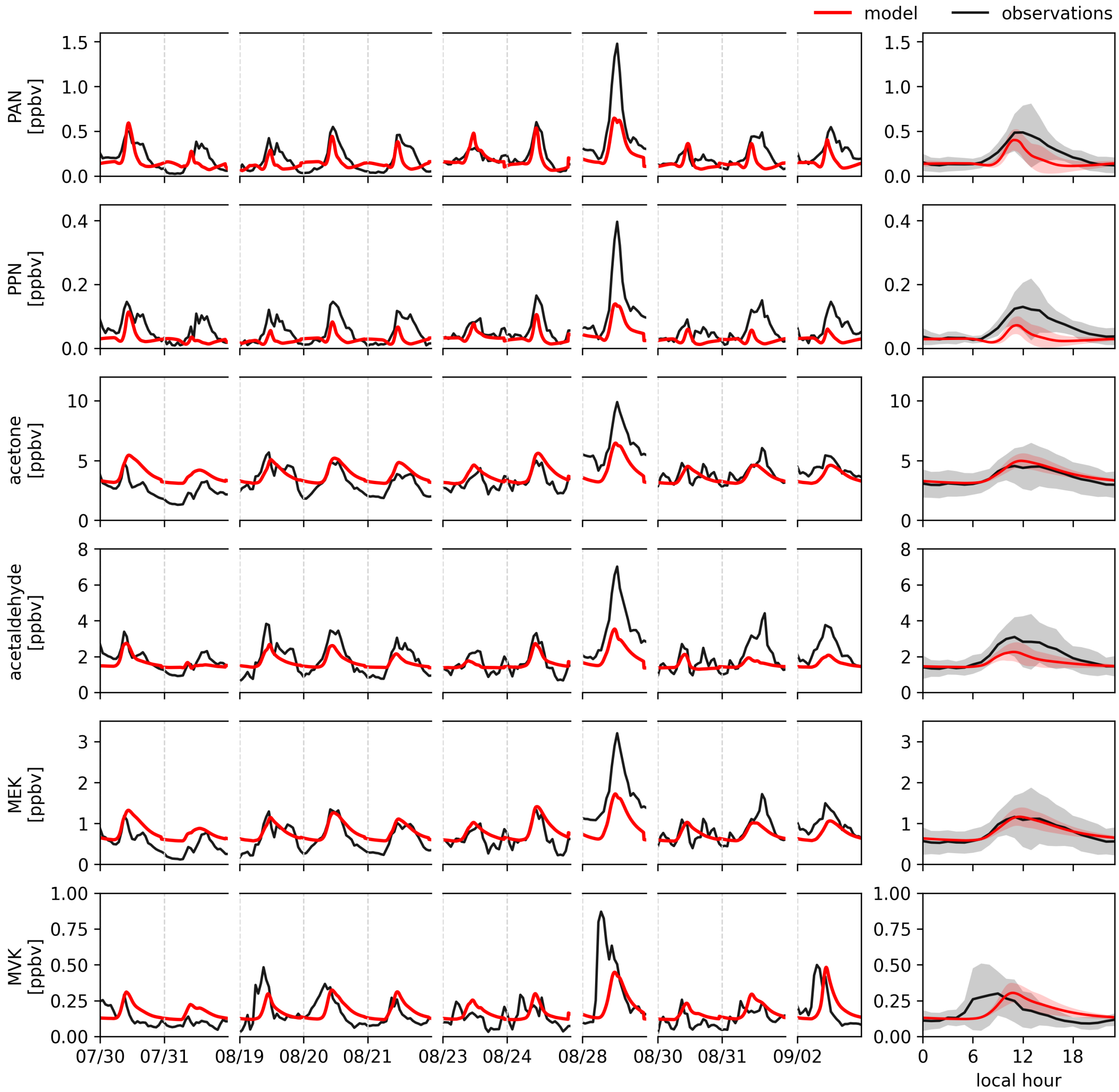

Figure 3.7: Same as Figure 3.6 but for PAN, PPN, acetone, acetaldehyde, MEK and MVK.

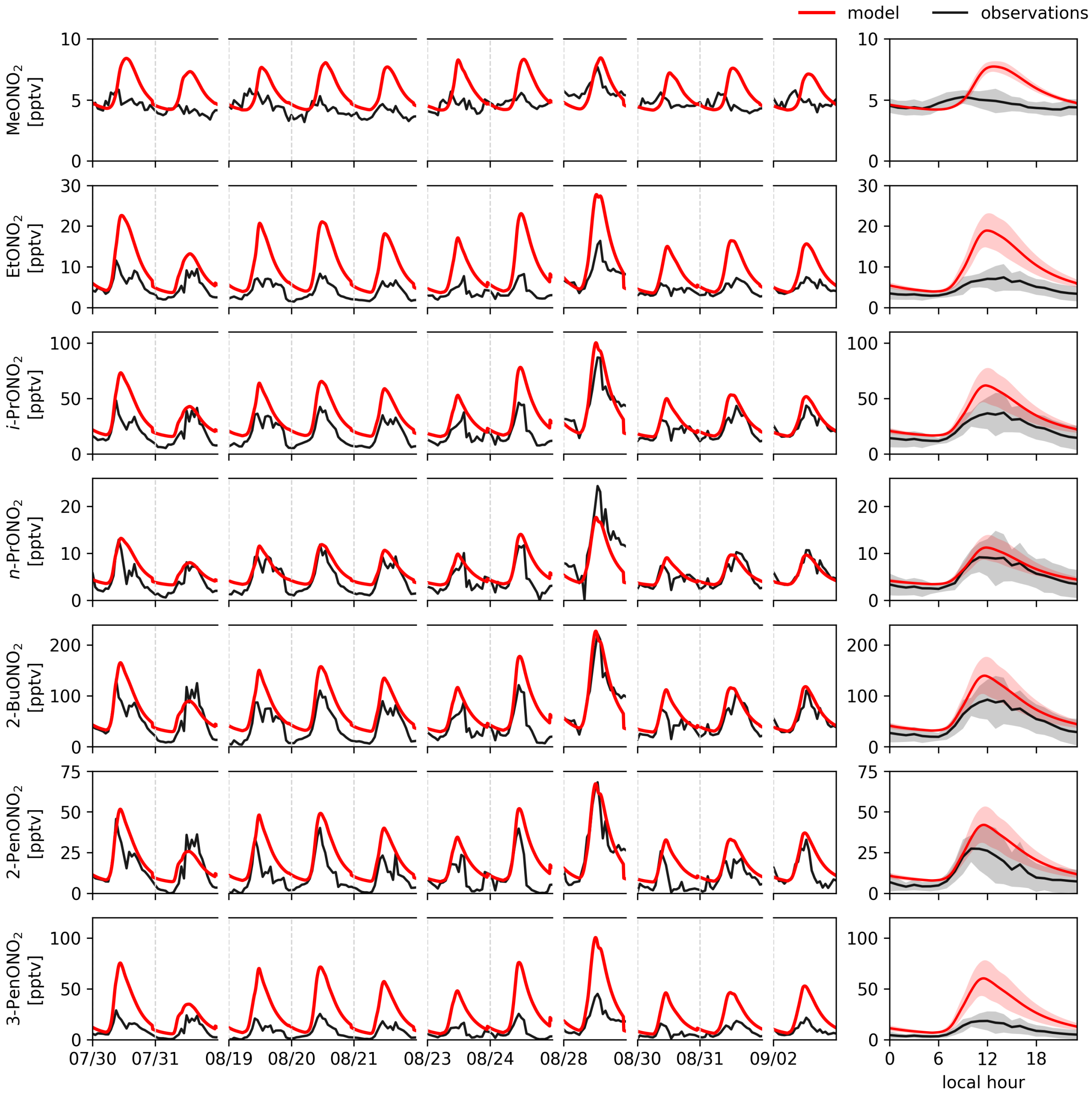

Figure 3.8: Same as Figure 3.6 but for C_1-C_5 $RONO_2$.

Table 3.2: Sensitivity of model-calculated maximum O_3 and daytime (06:00–18:00 LT) mean $P(O_3)$ to select model parameters. Absolute and percent differences were derived by varying each parameter individually by ±10% and comparing results to the base case simulation (constrained to observed levels of NO_x and primary VOCs). Results are shown for the +10% / -10% sensivity runs, and are averaged over the eleven modeled days.

		maximum O_3		daytime mean $P(O_3)$	
parameter	base case value	ppbv	%	ppbv h^{-1}	%
dilution (k_{dil})	5×10^{-5} s^{-1}	-1.52 / 0.36	-2.45 / 0.58	-0.15 / -0.02	-3.81 / -0.59
background O_3	36 ppbv	2.27 / -3.61	3.67 / -5.83	-0.12 / -0.07	-3.04 / -1.75
surface albedo	0.2	0.23 / -1.42	0.37 / -2.29	0.01 / 0.18	0.27 / -4.61
total O_3 column	287 DU	-2.58 / 1.44	-4.16 / 2.23	-0.29 / 0.11	-7.35 / 2.79
TUV photolysis rates correction factor (j_{corr})	scaled by observed solar radiation	-3.33 / -4.52	5.38 / -7.30	0.38 / -0.56	9.65 / -14.15
initial HCHO	0.375 ppbv	-0.59 / 0.74	-0.59 / -1.19	-0.08 / -0.10	-2.14 / -2.61
O_3 deposition velocity	0.8 cm s^{-1}	-1.32 / 0.04	-2.14 / 0.06	-0.09 / -0.10	-2.32 / -2.44

3.3 O_3 production sensitivity

Understanding the chemical regimes that drive O_3 production is essential for devising effective O_3 control strategies. The L_N/Q metric, which describes the fraction of radical termination involving reactions with NO_x, allows for the evaluation of O_3 production sensitivity instantaneously at each model time step. Our results suggest that O_3 production at CAVE cannot be described as exclusively NO_x- or VOC-sensitive, because O_3 production shifts from a VOC-sensitive regime in the morning to a primarily NO_x-sensitive regime in the afternoon (Figure 3.9). This diurnal regime shift is consistent across the eleven modeled days and is independent of whether the chemical or "policy-relevant" L_N/Q transition threshold is considered (see Section 2.4). Similar sub-daily variations in chemical regime have been previously reported at various sites impacted by large NO_x emissions, including urban and suburban areas (Sakamoto et al., 2019; Mao et al., 2010; Sillman and West, 2009; Rickly et al., 2023), as well as rural sites downwind of urban regions (Pan et al., 2015).

This diurnal shift in O_3 production regime is further analyzed by examining the evolution of primary radical production ($P(RO_x)$) and termination ($L(RO_x)$) budgets throughout the day (Figure 3.10), where $RO_x = OH + HO_2 + RO_2$. In the initial hours after sunrise (06:00–09:00 LT), as the

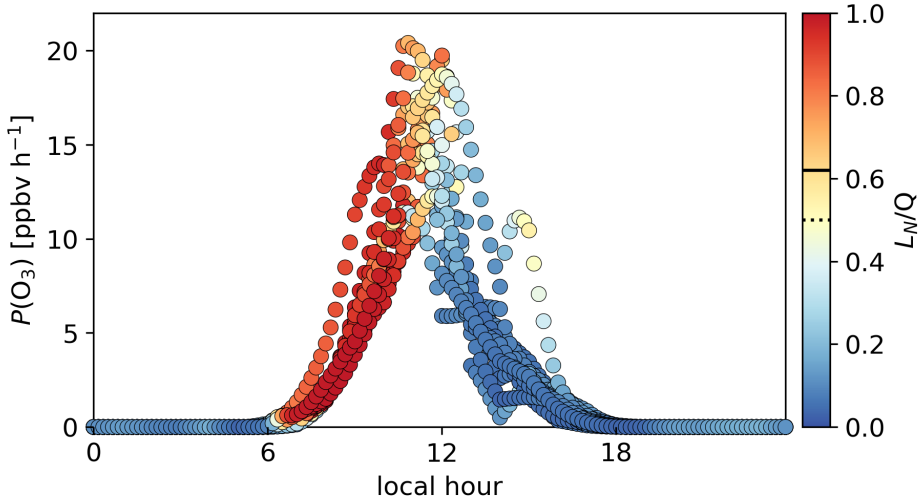

Figure 3.9: The instantaneous O_3 production rate ($P(O_3)$) at each model time step for the eleven modeled days. Each point is colored by the corresponding L_N/Q value. The dashed line on the color bar indicates the chemical transition point ($L_N/Q = 0.5$), and the solid vertical line marks the "policy-relevant" transition point (L_N/Q = 0.62) as determined from Figure 2.3. O3 formation at L_N/Q values below (above) this transition point is NO_x-sensitive (VOC-sensitive).

radical pool begins to grow through photolysis of O_3, HCHO, and other OVOCs, enough NO_x is present to dominate radical termination. This occurs primarily through HNO_3 formation, with additional contributions from net $RONO_2$ and RO_2NO_2 formation (the sum of these three pathways is considered in the L_N term Equation 2.2). We note that the model does a good job of simulating observed 24-h mean PAN/HNO_3 ratios (Figure 3.11), which provides confidence in the model-calculated radical termination pathways. Deviations of modeled PAN/HNO_3 from observations likely stem from the advection of either compound from distant sources (i.e., not formed by *in situ* photochemistry) or because the model does not consider heterogeneous HNO_3 chemistry (e.g., removal by ammonium nitrate formation, formation by N_2O_5 hydrolysis). Around 9:00 LT, NO_x levels begin to rapidly decline due to photochemical consumption, making way for radical-radical interactions (L_R; Equation 2.3) to take over as the primary mechanism of radical termination. Organic hydroperoxides (ROOH) and, to a lesser extent, hydrogen peroxide (H_2O_2), become the dominant radical combination species. O_3 production now proceeds in a NO_x-sensitive regime that persists throughout the remaining daylight hours.

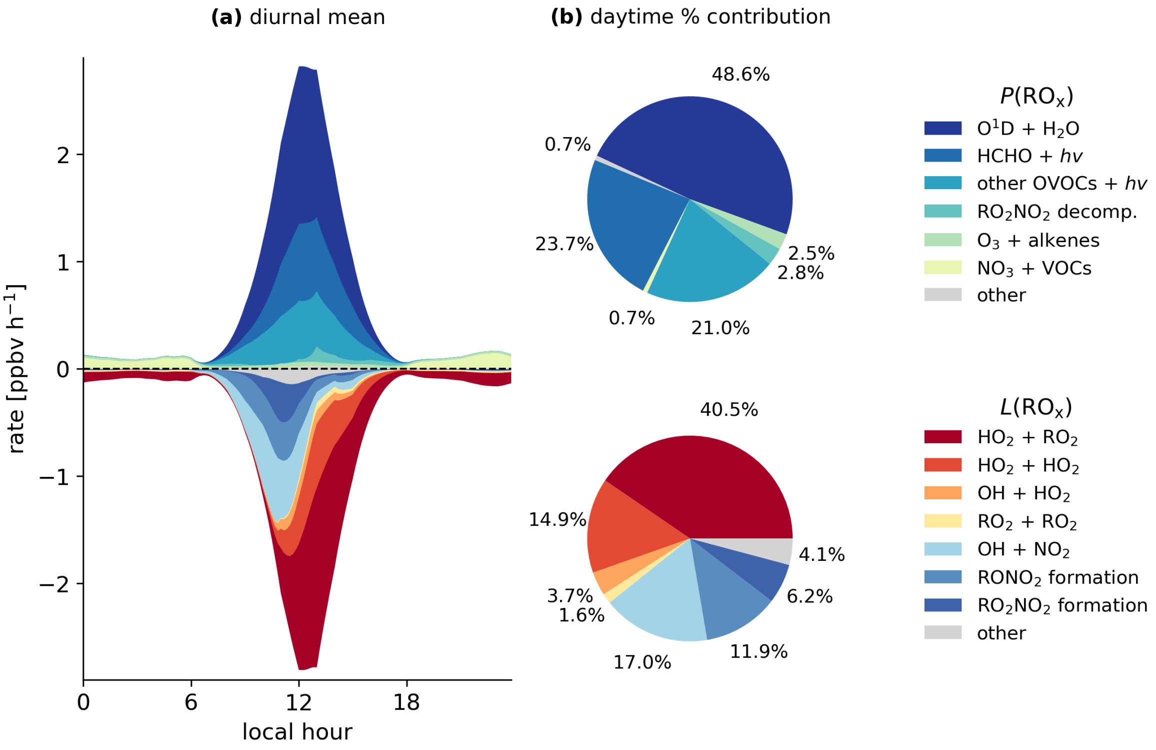

Figure 3.10: (a) Model-calculated mean diurnal profile of primary radical production ($P(RO_x)$) and termination ($L(RO_x)$) pathways across the eleven modeled days. (b) Daytime (06:00–18:00 LT) percent contribution of each RO_x production/termination pathway summed across the eleven modeled days.

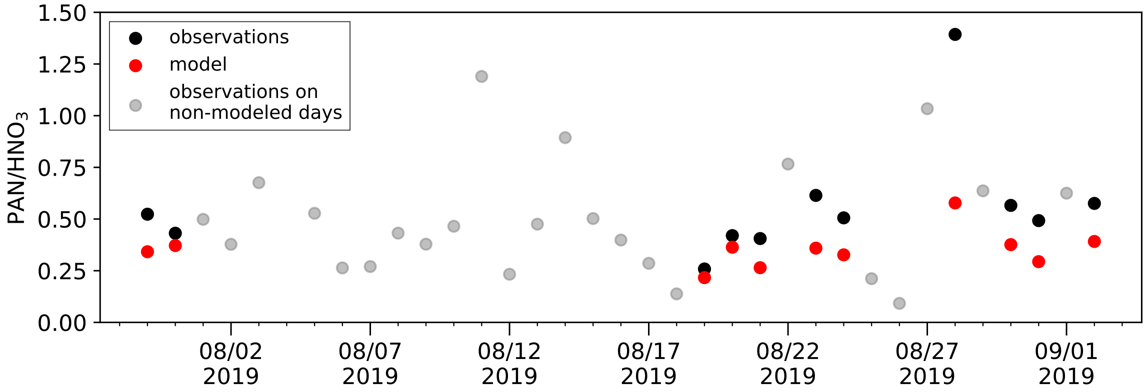

Figure 3.11: Model-observation comparison of 24-h mean PAN/HNO_3 ratios. Modeled values are shown in red. Observed values for the eleven modeled days and all other days are shown in black and gray, respectively. The Pearson's correlation coefficient (*r*) between modeled and observed values for the eleven days is 0.91.

To examine how O_3 responds to changes in NO_x and VOC abundances, isopleth diagrams were constructed for each of the eleven modeled days. This was done by running simulations across a 20

× 20 matrix of independently scaled NO_x and primary non-methane VOC constraints. Constraints were scaled from their observed levels by factors ranging from 0.1 to 2.0. Isopleths constructed using this methodology can be configured to show either the model-predicted daily maximum O_3 concentrations (e.g., Edwards et al., 2014; Rickly et al., 2023) or the instantaneous O_3 production rate ($P(O_3)$) averaged over photochemically active hours (e.g., Nelson et al., 2021). Each choice has its advantages and disadvantages. Isopleths depicting absolute O_3 concentrations are more intuitive and directly relevant for policy goals such as reducing maximum O_3 to meet the NAAQS. These interpretations, however, should be approached with caution given that observationally constrained box models are inherently diagnostic tools rather than predictive ones (Cardelino and Chameides, 1995). Additionally, real-world O_3 concentrations vary based on physical processes that are highly simplified in box models (see Section 2.3). Displaying isopleths in terms of $P(O_3)$ does not make the model any more predictive, but in this case, the isopleth purely illustrates how photochemical O_3 production varies with changing NO_x and VOCs.

Average isopleths for the eleven modeled days are shown both in terms of maximum O_3 (Figure 3.12) and daytime mean $P(O_3)$ (Figure 3.13). These diagrams reveal that O_3 was primarily sensitive to NO_x, as NO_x reductions led to a steeper decline in O_3 than VOC reductions. The prevalence of NO_x-sensitive conditions can also be inferred from the pie charts in Figure 3.10, where reactions encompassed by the L_N term account for less than half (35%) of total $L(RO_x)$ during daytime (06:00–18:00 LT). That said, Figures 3.12 and 3.13 show that maximum O_3 was still responsive to VOC reductions, albeit to a lesser extent than NO_x, indicating proximity to the transition between NO_x-sensitive and VOC-sensitive regimes.

The isopleth diagrams in Figures 3.12 and 3.13 represent an average of eleven modeled days, and individual days varied as to where O_3 formation at observed NO_x and VOC levels laid relative to the regime transition point (i.e., the O_3 “ridge” on the isopleth diagram). Isopleths for each individual day are shown in Figures 3.14 and 3.15. We can further examine two days with distinctly different isopleths: 8/19/2019 as an example where O_3 formation was more sensitive to VOCs than to NO_x, and 8/28/2019 as an example where O_3 formation was more strictly NO_x-sensitive. Figure

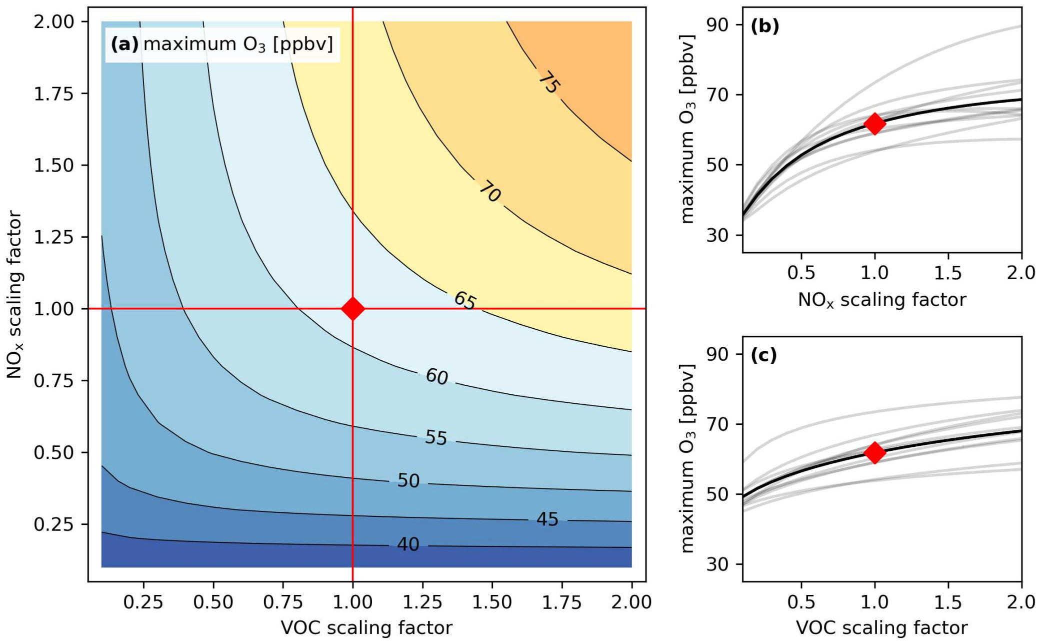

Figure 3.12: (a) Maximum O_3 isopleth (mean of eleven modeled days) derived by scaling NO_x and non-methane VOC constraints by factors ranging from 0.1 to 2.0. Panels (b) and (c) show the modeled maximum O_3 as a function of the NO_x and VOC scaling factors, respectively, with black lines showing the 11-day mean and the gray lines showing individual day's simulations. The diamond symbol in the center of each panel represents the model maximum O3 at observed NOx_x and VOC levels.

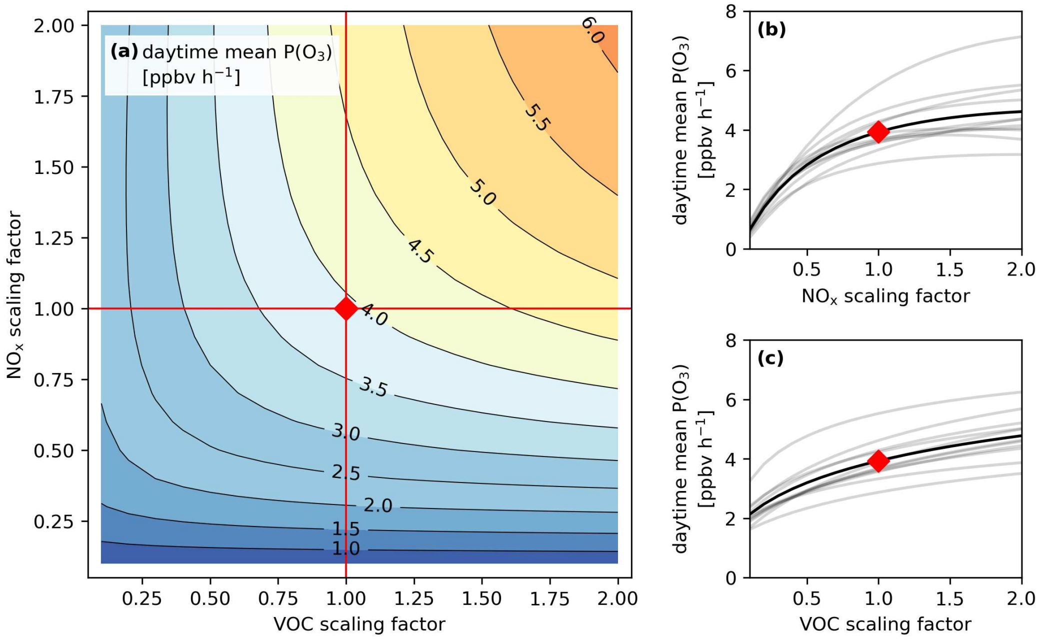

Figure 3.13: Same as Figure 3.12 except in terms of daytime (06:00–18:00 LT) mean $P(O_3)$.

3.16 showcases the differences in NO_x/NO_y ratios and VOC-OH reactivities between 8/19/2019 and 8/28/2019. NO_x/NO_y was notably high ($\sim$1.0) in the morning of 8/19, suggesting influence from a very fresh air mass. The campaign-wide maximum 1-h NO_x concentration of 15.6 ppbv was also observed on 8/19. More than 95% of VOC-OH reactivity during the morning hours (06:00–10:00 LT) of 8/19 was attributed to the three O&G-related PMF factors, including a significant (19%) contribution from the process-specific O&G factor (Factor 3). As Factor 3 is composed of highly reactive primary VOCs (C_8-C_{10} alkanes, ethylbenzene, and xylenes), its contribution to total VOC-OH reactivity is expected to rapidly decrease with photochemical age. Many previous studies have observed a shift from VOC-sensitive conditions close to emission sources (due to titration of O_3 by NO and efficient removal of OH by NO_2) to NO_x-sensitive conditions further downwind (Sillman, 1999; Kleinman et al., 2000). This influence from a fresh air mass on 8/19 helps explain the apparent VOC sensitivity. 8/28 also had high NO_x/NO_y in the morning, meeting the 0.8 threshold that categorizes this day as fresh/O&G, although not as high as 8/19. Observed NO_x concentrations were also lower on 8/28, peaking at 7.5 ppbv. Even though the three O&G-related PMF factors still dominated VOC-OH reactivity in the morning (81%), 8/28 was different from 8/19 in that very little reactivity was contributed from the process-specific O&G factor (4%). Additionally, observed levels of secondary VOCs were much larger on 8/28 than 8/19 (Figure 3.7). In summary, lower NO_x/NO_y, lower reactive primary VOCs, and greater levels of secondary VOCs suggest that more photochemically aged conditions likely drive the strong NO_x sensitivity observed on this day.

On average, our model results indicate that NO_x emission reductions would be most effective at reducing O_3 at CAVE, although reduction of VOC emissions may still be important, especially when photochemically fresh air masses rich in NO_x impact CAVE. This mixed sensitivity result is consistent with findings in various urban areas (e.g., Koplitz et al., 2022; Jin and Holloway, 2015; Berezina et al., 2020), as well as at a site near the Denver-Julesburg O&G basin in northern Colorado. Earlier box modeling studies conducted at the Boulder Atmospheric Observatory (BAO) showed that summertime O_3 formation was primarily sensitive to NO_x but still responded

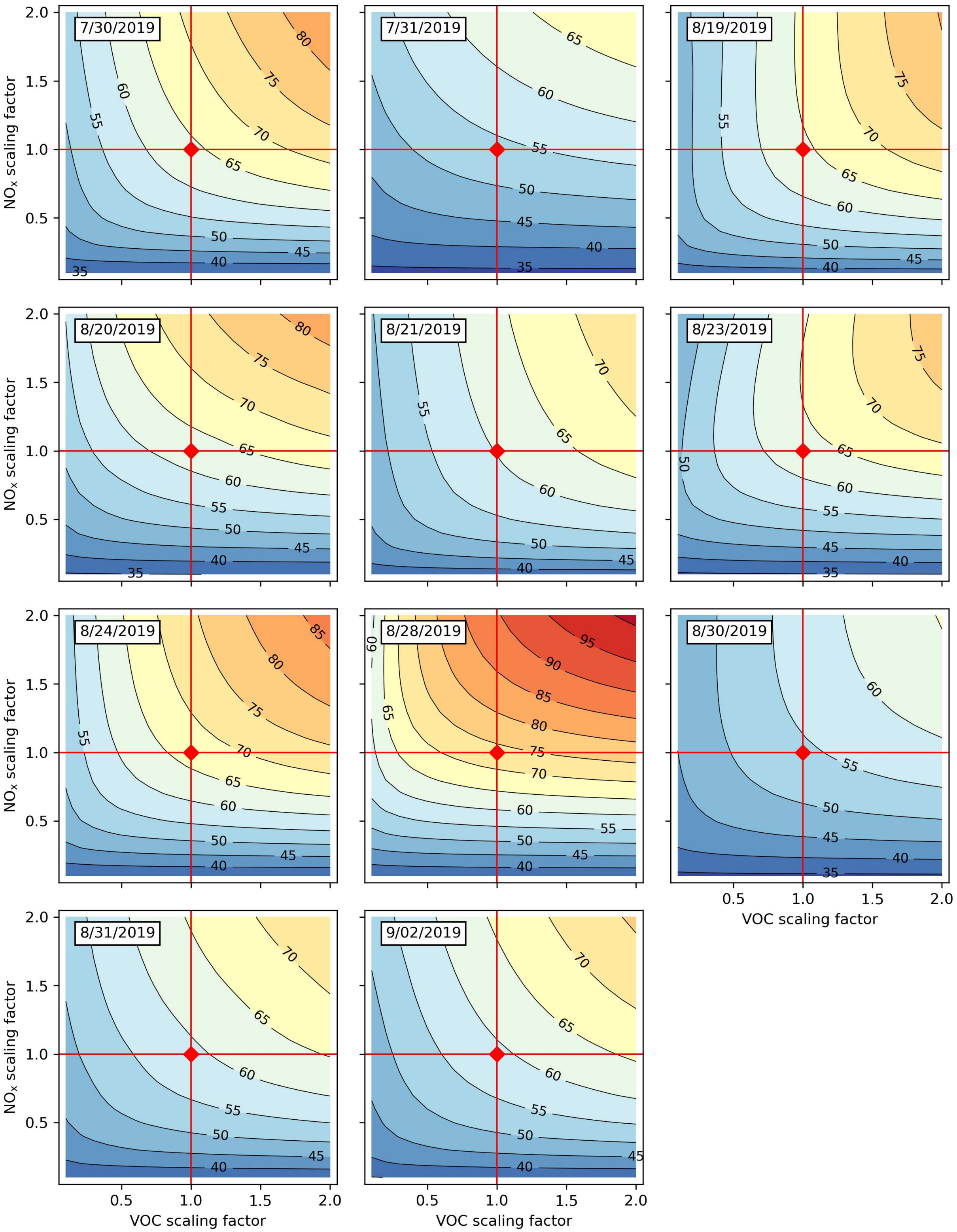

Figure 3.14: Maximum O_3 isopleths (ppbv) for each of the eleven modeled days. The red symbol in the center of each subplot represents the model maximum O_3 at observed NO_x and VOC levels for that day.

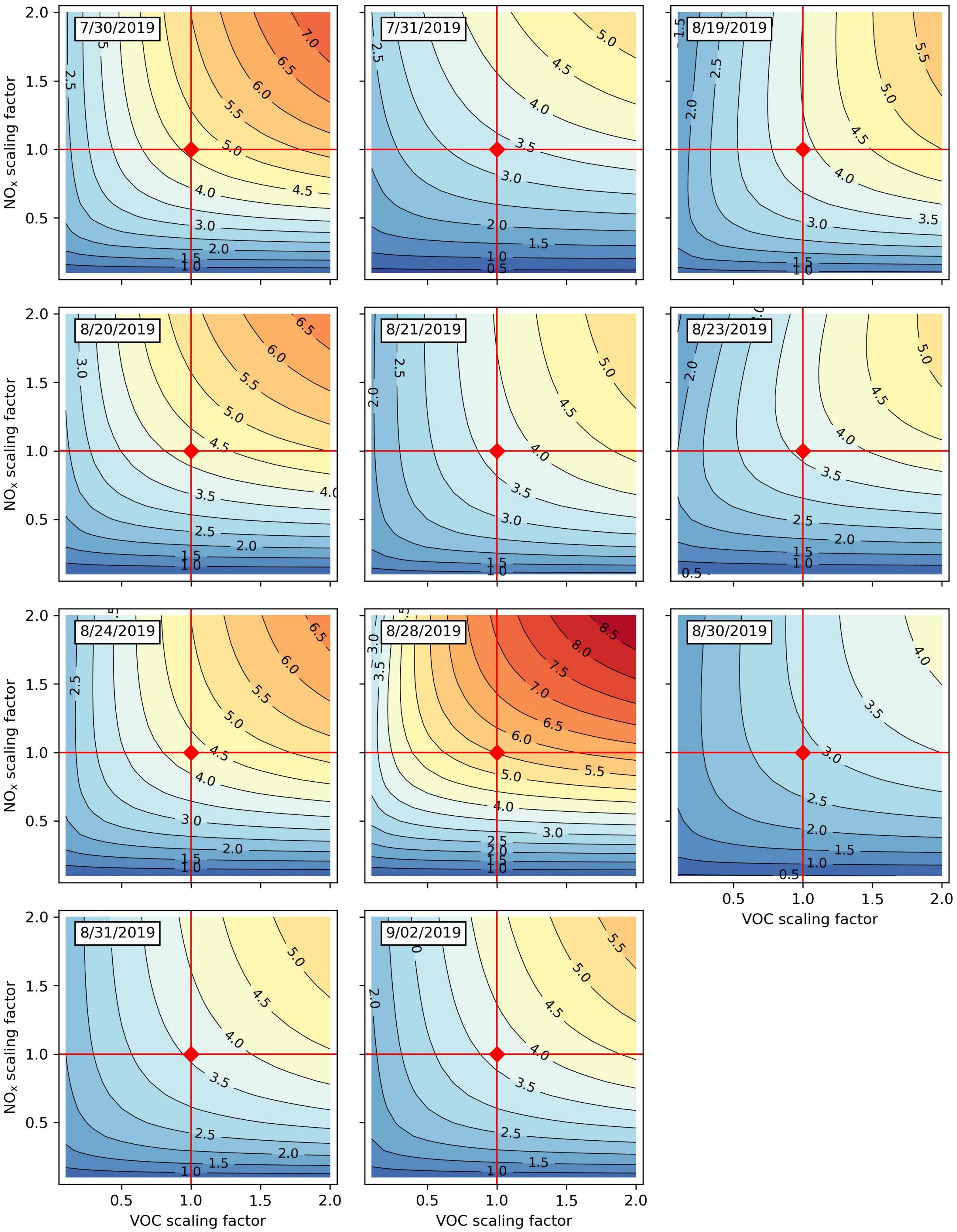

Figure 3.15: Same as Figure 3.14 except in terms of daytime (06:00–18:00 LT) mean *P*(O_3) (ppbv h^{-1}).

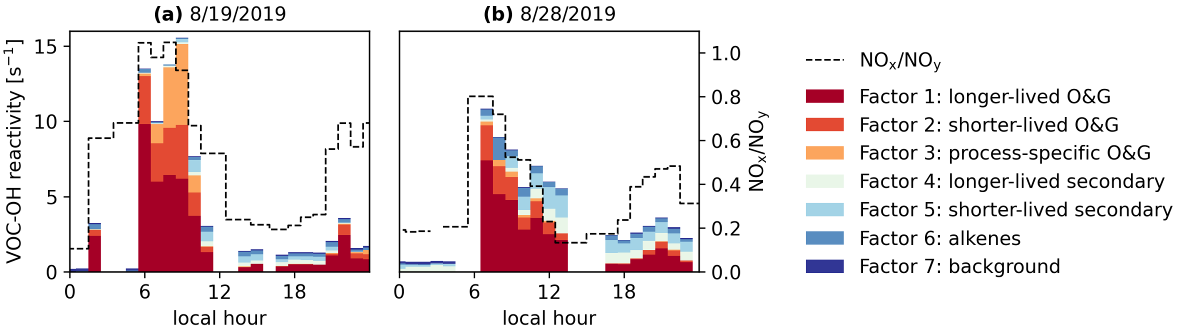

Figure 3.16: Hourly contributions of PMF factors to VOC-OH reactivity (left axis) and the observed NO_x/NO_y ratio (right axis) on (a) 8/19/2019 and (b) 8/28/2019.

to changes in O&G-related VOCs due to their significant contributions to VOC-OH reactivity (McDuffie et al., 2016; Lindaas et al., 2019).

3.4 Precursor-specific impacts on O_3

To examine how specific precursors impact O_3 at CAVE, we employ the relative incremental reactivity (RIR) metric (Cardelino and Chameides, 1995; Carter and Atkinson, 1989). The RIR of an O_3 precursor X (or group of precursors) is defined as the percent change in daytime mean $P(O_3)$ per percent change in precursor level:

$$\mathrm{RIR(X)} = \frac{\Delta P(\mathrm{O_3})(\mathrm{X})/P(\mathrm{O_3})(\mathrm{X})}{\Delta S(\mathrm{X})/S(\mathrm{X})} \tag{3.2}$$

The change in precursor level ($\Delta\ S(X)/S(X)$) was set to a 20% reduction in this study, and the resulting $P(O_3)$ was compared to the base case simulation, where NO_x and VOC constraints were unadjusted from their observed levels. To ensure the relevance of this analysis to realistic emission reduction scenarios, VOC constraints were adjusted in groups based on the PMF source factors described by Pan et al. (2023), while unapportioned VOCs not part of the PMF solution were left unscaled. The PMF-reconstructed concentrations accounted for 96.3 ± 0.04% (mean ± 1 standard deviation) of the total measured VOC mixing ratio across the eleven modeled days. PMF Factors 4 (longer-lived secondary) and 5 (shorter-lived secondary) were excluded from the RIR analysis

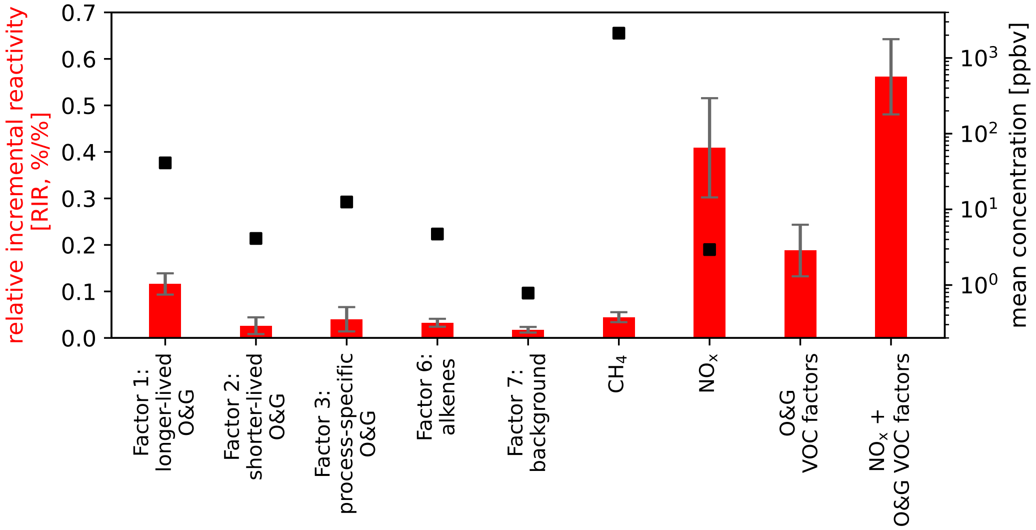

Figure 3.17: Relative incremental reactivity (RIR; left axis) and mean concentration (right axis, log scale) of primary VOC PMF source factors, CH_4, and NO_x. Results are averaged over the eleven modeled days with error bars representing ± 1 standard deviation. RIR is defined as the response of modeled $P(O_3)$ to a 20% reduction in precursor(s) (Equation 3.2). Also shown are RIR results based on a 20% reduction in all O&G factors (sum of PMF Factors 1–3) and a combined 20% reduction in O&G factors together with NO_x.

because these factors mainly consisted of secondary species (OVOCs and $RONO_2$) that were not constrained within the model.

Figure 3.17 shows that NO_x had the largest RIR (0.41) averaged over the eleven modeled days, surpassing the RIR of each of the three O&G PMF factors (0.12, 0.03, 0.04 for Factors 1, 2, and 3, respectively), which collectively accounted for the majority of the total VOC mixing ratio and the calculated VOC-OH reactivity. To put these RIR values into context, the 0.41 RIR for NOx implies that a 20% reduction in the NO_x constraint yielded an 8.2% reduction in daytime mean $P(O_3)$, which corresponds to a 2.7 ppbv reduction in model maximum O_3. The larger RIR for NO_x is consistent with O_3 production being predominantly NO_x-sensitive at CAVE, as discussed in the previous section. We note that CH_4, although abundantly emitted from O&G operations in the Permian basin (Veefkind et al., 2023; Zhang et al., 2020), had a relatively minor impact on simulated O_3 due to its lower reactivity compared to larger, more reactive VOCs. Figure 3.17 also includes RIR results for two additional precursor reduction scenarios: a 20% reduction in all O&G factors (sum of PMF Factors 1–3) and a combined 20% reduction in the O&G factors together with

NO_x. Our simulations indicate that reducing NO_x alone is approximately 120% more effective at reducing $P(O_3)$ compared to reducing the O&G factors alone. However, the combined reduction of NO_x and the O&G factors leads to an approximately 40% greater reduction in $P(O_3)$ compared to solely reducing NO_x.

While the RIR results presented in Figure 3.17 provide an average perspective over the eleven modeled days, it is worth highlighting several notable day-to-day differences (Figure 3.18). On each individual day, the RIR of NO_x consistently surpassed the RIR of any of the primary PMF VOC factors. The RIR of NO_x also exceeded the RIR of the summed O&G factors on all days except 8/19/2019. This is the same day examined in the previous section, on which CAVE was likely impacted by a very photochemically fresh air mass and thus exhibited VOC-sensitive behavior. On 8/19/2019, the combined 20% reduction in both NO_x and the O&G factors resulted in a 70% (100%) greater RIR than through reductions in the O&G factors alone (NO_x alone). This analysis thereby reinforces our conclusion that while the general picture of O_3 production at CAVE is NO_x-sensitive, both NO_x and VOC emission reductions would help lower O_3. Targeting emissions from regional O&G activities should be a priority for O_3 reduction since these activities are the dominant source of both NO_x and VOCs to CAVE (Pan et al., 2023; Pollack et al., 2023). This is supported by robust correlations between NO_x and the three O&G factor contributions from the PMF analysis, along with strong correlations between NO_x and individual O&G tracer species (C_1-C_3 alkanes; Pollack et al., 2023). Additionally, both NO_x and O&G-related VOCs were primarily associated with the southeast wind sector, where there are no major cities within $\sim$ 200 km. The absence of weekday-weekend differences in NO_x, which would typically indicate an urban combustion source, further indicates that contributions from urban NO_x sources are minor (Pollack et al., 2023).

3.5 High O_3 on photochemically aged days

Although the O_3 production sensitivity results discussed above are based on the eleven fresh/O&G days deemed appropriate for treatment with a box model, this does not include all high O_3 days

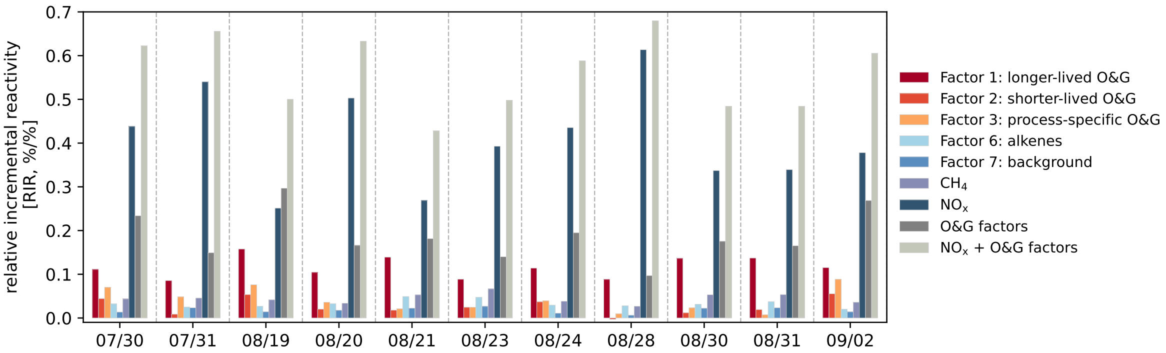

Figure 3.18: Relative incremental reactivity (RIR; Equation 3.2) of primary VOC PMF source factors, CH_4, and NOx for each of the eleven modeled days. Also shown are RIR results based on a 20% reduction in all O&G factors (sum of PMF Factors 1–3) and a combined 20% reduction in O&G factors together with NO_x.

observed during CarCavAQS. In this section, we examine a 5-day episode (8/5/2019–8/10/2019) during which hourly O_3 mixing ratios surpassed 70 ppbv on each day. Based on NO_x/NO_y and *i*-/*n*-pentane ratios (Section 3.1), these days were sorted into the aged/O&G group.

Figure 3.19 presents a time series of this 5-day episode. Despite observed variations in local wind direction, near-constant *i*-/*n*-pentane below one indicates that the air masses impacting CAVE during this period were consistently influenced by O&G emissions. Moreover, 48 h HYSPLIT back-trajectories for each day show consistent transport over the Permian basin and, occasionally, over more distant O&G basins (Figure 3.20). F0AM model simulations for these five days under the same configurations employed for previously discussed model results (i.e., constrained to observed NO_x and primary VOCs, constant dilution rate, constant background O_3) substantially underestimate O_3 in comparison to observations. This indicates that locally observed O_3 precursor abundances cannot explain these high O_3 levels. Significant O_3 on these days must have formed during photochemical processing upwind. This is consistent with the markers of strong photochemical aging, including lower NO_x/NO_y ratios (maximum morning NO_x/NO_y ranged from 0.38 to 0.76) and enhanced secondary VOC levels (longer- and shorter-lived secondary PMF factors contributed 22% and 14% to the 24-h mean VOC-OH reactivity budget, respectively). Model results show that *in situ* photochemical O_3 formation on top of the transported O_3 during this period is definitively NO_x-sensitive, with only 10% of daytime radical termination occurring by reaction with NO_x (in contrast to 35% during fresh/O&G days). Based on our understanding of how O_3 production sensitivity evolves over time, it is likely that emissions of both NO_x and VOCs contributed to these high O_3 days despite the NO_x-sensitivity of *in situ* O_3 production. A fraction of the transported O_3 may have formed under VOC-sensitive conditions when closer to fresh NO_x sources.

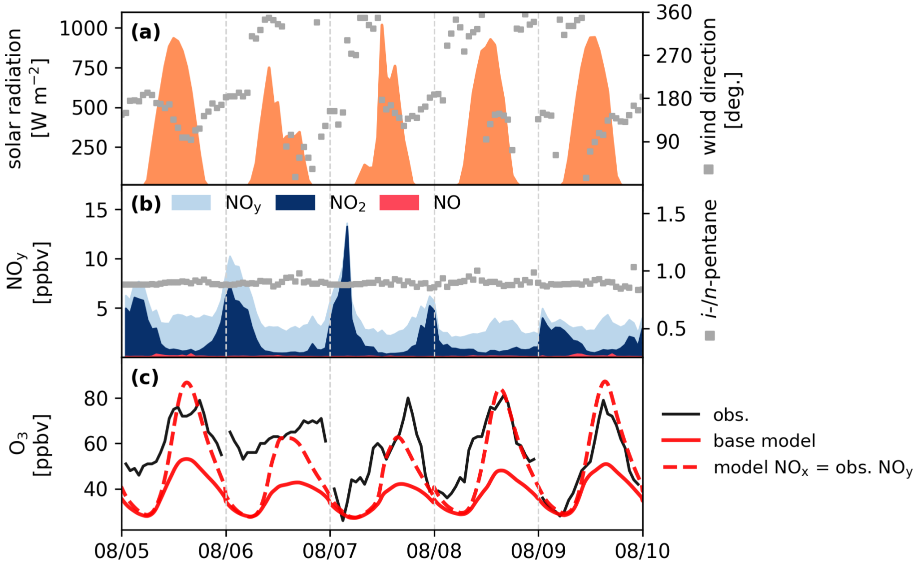

Figure 3.19: Time series of (a) solar radiation (left axis) and wind direction (right axis), (b) NO_y, NO_2, NO (left axis) and hourly *i*/*n*-pentane ratios (right axis), and (c) O_3 mixing ratios during five high consecutive high O_3 days observed at CAVE. Also shown in (c) are modeled O_3 mixing ratios under the base case conditions (see text), and under a second model scenario in which the model NO_x was constrained with observed NO_x mixing ratios.

To investigate whether sufficient NO_x could have been present in the air mass to account for upwind O_3 formation during transport to CAVE, we re-ran the F0AM simulations constraining the model NO_x with observed NO_y concentrations for this 5-day episode (Figure 3.19). NO_y acts as an estimate of the amount of NO_x at time of emission, assuming minimal depositional loss of HNO_3 or other NO_z compounds during transport (e.g., Trainer et al., 1993). We note that this model scenario should be interpreted qualitatively since it does not account for the upwind photochemical oxidation of primary VOCs. Modeled O_3 in this scenario much more closely aligns with observed O_3, indicating that most of the observed O_3 was formed during transport rather than *in situ*. Discrepancies between observed and modeled O_3 in this scenario persist, particularly on 8/6 and 8/7, which can be attributed to the suppression of photochemical activity by cloud cover (see solar radiation time series in Figure 3.19). O_3 levels predicted by the box model depend on the chosen dilution rate and background O_3 levels, which, given mixing effects, are not expected to be constant throughout the trajectory of the air masses. A more comprehensive assessment of the photochemical evolution of long-range transported air masses from time of emission to arrival at CAVE would require a 3-D chemical transport model (CTM). Future CTM studies would, however, need to thoroughly characterize the uncertainties and biases associated with the chosen emissions inventory (e.g., Ahmadov et al., 2015; Francoeur et al., 2021; Kim et al., 2022).

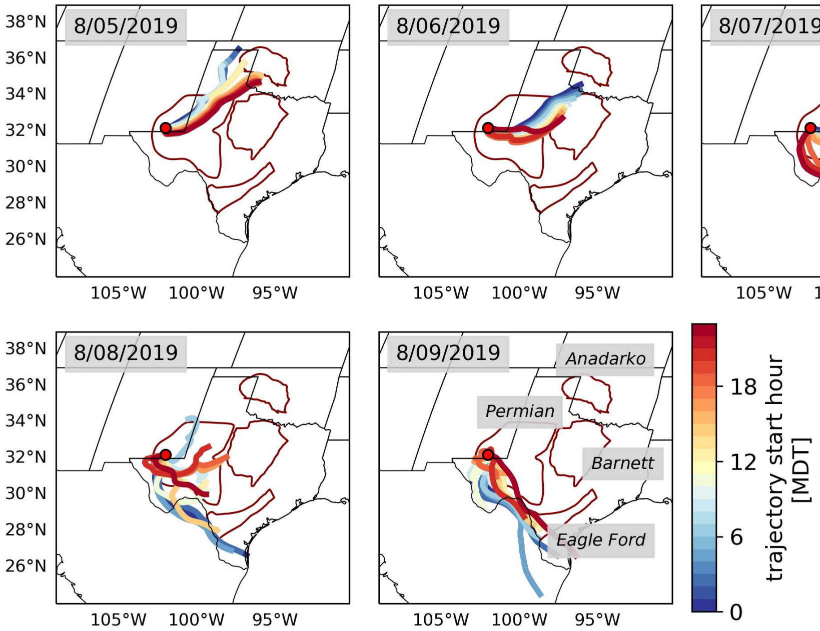

Figure 3.20: 48 h HYSPLIT back trajectories across the five high O_3 days shown in Figure 3.19. A new trajectory was initiated from CAVE every 2 h using NAM-12 meteorology. Each trajectory is colored by the start hour in Mountain Daylight Time (MDT). The red dot represents the location of CAVE, and the maroon polygons outline major O&G basins in the region (https://www.eia.gov/maps/maps.htm).

Chapter 4

Conclusions and future research directions

4.1 Conclusions

This thesis applied a photochemical box model to an extensive O_3 precursor data set collected at CAVE during summer 2019. Days during the study period were divided into three groups based on variations in photochemical age and emission source: fresh/O&G, aged/O&G, and aged/bkg. Fresh/O&G days were marked by high morning NO_x/NO_y ratios (>0.8), the predominant influence of O&G-related VOCs to VOC-OH reactivity, and consistent air mass back-trajectories indicating transport from the Permian basin. Aged/O&G days had lower morning NO_x/NO_y, a greater contribution of secondary VOCs to VOC-OH reactivity, and transport patterns that, while more variable, still indicated influence from O&G-producing regions. Aged/bkg days exhibited considerably less active photochemistry, with no clear diurnal patterns in O_3 or NO_x/NO_y, much lower total VOC levels, and persistent westerly/northwesterly transport, consistent with greatly reduced O&G influence. Given the limitations of 0-D models in accounting for transport effects, our analysis primarily focuses on the eleven fresh/O&G days, which represent periods when most of the observed O_3 at CAVE can be attributed to *in situ* photochemical production.

An analysis of model-calculated radical loss rates suggests that NO_x levels were high enough to impose VOC sensitivity on O_3 formation in the morning hours, while afternoon NO_x loss through photochemical consumption led to NO_x-sensitive conditions. O_3 isopleth diagrams constructed for the eleven fresh/O&G days indicate that daily maximum O_3 was most sensitive to NO_x, but close to the transition between NO_x- and VOC-sensitive regimes. Therefore, *in situ* O_3 formation is subject to changing sensitivity with relatively small variations in the NO_x/VOC ratio. We observed day-to-day variability in the O_3 production regime, with one day out of the eleven simulated being more sensitive to VOCs than NO_x. RIR analysis performed on NO_x and PMF-reconstructed VOC factors showed that reductions in both NO_x and O&G-related VOC can help reduce O_3 formation at CAVE, but NO_x reductions are generally more effective.

An important caveat is that in a scenario where nearby precursor emissions are reduced, CAVE may still experience high O_3 during influence from photochemically aged air masses carrying O_3 and additional precursors from more distant O&G production regions. Using the measured total NO_y as a proxy for NO_x at time of emission significantly improves model performance for a five 5-day high O_3 episode when air masses were both photochemically aged and influenced by O&G. This confirms that a large portion of the O_3 observed on these days was not formed locally but instead during transport to CAVE. While these aged air masses were definitively NO_x sensitive upon arrival at CAVE, it is likely that VOC emissions also contributed to O_3 formation along the air mass' trajectory when closer to fresh NO_x sources.

Long-term attainment of O_3 at CAVE would benefit from regulation of precursor emissions not only from the Permian but also from other upwind O&G basins (e.g., Eagle Ford, Barnett, Anadarko). Reducing NO_x emissions from O&G activities might be most efficiently realized through a targeted reduction of emissions from well drilling and completion activities, as indicated by a recent satellite-based analysis of NO_x emissions from the Permian basin during the COVID-19 pandemic. Reduced O&G demand in early 2020 led to a temporary decline in production and drilling activities, resulting in lower NO_x emissions particularly in areas with intensive drilling compared to areas with only production (Serrano-Calvo et al., 2023). A path for reducing emissions from drilling operations without removing those activities is the implementation of electrified, grid-powered drill rigs (Ericson et al., 2019).

4.2 Future research directions

The box modeling results presented in this thesis, together with a VOC source apportionment analysis (Pan et al., 2023), an observational-based analysis (Pollack et al., 2023), and an earlier screening study (Benedict et al., 2020) collectively establish regional O&G activities as the principal factor contributing to the recent high O_3 levels observed at CAVE.

A subsequent field campaign was conducted at CAVE during the summer of 2021 as part of the Southeastern New Mexico Air Quality Study (SENMAQS), in collaboration with the EPA. This campaign involved similar measurements at CAVE compared to CarCavAQS, including the same real-time GC system and NO_x/NO_y instruments in addition to continuous measurements of O_3 and meteorological parameters by the NPS. While the results presented in this thesis focus exclusively on the 2019 study, the 2021 data set warrants further investigation. Specifically, it provides an opportunity to compare VOC measurements between the two campaigns and assess any potential differences associated with increasing O&G productivity in the Permian basin. A PMF source apportionment analysis can be performed on the 2021 data set and compared with the findings of Pan et al. (2023) to determine if source profiles are consistent. Several external factors, such as potential influence from long-range transported wildfire smoke (2021 was a much more active fire year for the western US than 2019; https://www.ncei.noaa.gov/access/monitoring/monthly-report/fire/202113) and a stronger North American monsoon (https://www.weather.gov/psr/2021MonsoonReview), should also be considered. Additionally, O_3 precursor measurements collected in 2021 can be used to constrain a box model employing a similar methodology to that used in this thesis, to investigate if O_3 production sensitivity results presented here remain consistent with this more recent data set. It is worth noting, however, that without measurements of OVOCs, the influence of pyrogenic VOCs may be underestimated in these simulations (Rickly et al., 2023).

Differences in NO_x/VOC abundances between these two campaigns could be further explored by examining satellite measurements of O_3 precursors over the Permian basin. Dix et al. (2020) used data from the Ozone Monitoring Instrument (OMI) and the Tropospheric Monitoring Instrument (TROPOMI) to create a continuous time series of top-down-estimated NO_x emissions from the Permian basin from 2007-2018. More recent satellite data can be used to extend this NO_x emissions record to 2021. Further, the satellite-measured $HCHO/NO_2$ ratio—a proxy for the VOC/NO_x ratio—can augment conclusions drawn from ground-based observations by providing insight into how O_3 production sensitivity differs closer to emission sources or further downwind of the Permian. While there are uncertainties associated with using HCHO/NO_2 to diagnose photochemical regimes, such as cases where a wide range of HCHO/NO_2 values can indicate a "transitional" or mixed-sensitivity regime, it can still serve as a valuable tool for analyzing spatiotemporal trends in O_3 production sensitivity (Schroeder et al., 2017; Souri et al., 2023).

A limitation of this thesis is its reliance on box model results, which do not explicitly account for transport. Given that some of the highest O_3 days during CarCavAQS were associated with photochemically aged masses transported over long distances, future studies on O_3 formation downwind of the Permian may consider utilizing a 3-D chemical transport model. Recent efforts to improve VOC emission inventories from the O&G activities have employed tracer/tracer regression analyses with data collected from aircraft campaigns, along with NO_x emission estimates derived from satellite observations (Francoeur et al., 2021; Dix et al., 2022). Future 3-D modeling studies comparing these updated inventories with existing ones like the National Emissions Inventory (NEI) could use the O_3 precursor data sets collected at CAVE for model validation. A previous 3-D modeling study that compared a regression analysis-estimated top-down emission inventory with the NEI found that simulations based on the NEI, in contrast to the top-down inventory, were unable to reproduce high O_3 episodes observed in Utah's Uinta O&G basin (Ahmadov et al., 2015). This underscores the importance of refining inventories for more accurate O_3 modeling in regions impacted by O&G emissions.

References

Abeleira, A., Pollack, I. B., Sive, B., Zhou, Y., Fischer, E. V., and Farmer, D. K.: Source characterization of volatile organic compounds in the Colorado Northern Front Range Metropolitan Area during spring and summer 2015, Journal of Geophysical Research: Atmospheres, 122, 3595–3613, https://doi.org/10.1002/2016JD026227, 2017.

Ahmadov, R., McKeen, S., Trainer, M., Banta, R., Brewer, A., Brown, S., Edwards, P. M., De Gouw, J. A., Frost, G. J., Gilman, J., Helmig, D., Johnson, B., Karion, A., Koss, A., Langford, A., Lerner, B., Olson, J., Oltmans, S., Peischl, J., Pétron, G., Pichugina, Y., Roberts, J. M., Ryerson, T., Schnell, R., Senff, C., Sweeney, C., Thompson, C., Veres, P. R., Warneke, C., Wild, R., Williams, E. J., Yuan, B., and Zamora, R.: Understanding high wintertime ozone pollution events in an oil- and natural gas-producing region of the western US, Atmospheric Chemistry and Physics, 15, 411–429, https://doi.org/10.5194/acp-15-411-2015, 2015.

Akimoto, H.: Atmospheric Reaction Chemistry, Springer, Tokyo, Japan, 2014.

Allen, D. T.: Emissions from oil and gas operations in the United States and their air quality implications, Journal of the Air & Waste Management Association, 66, 549–575, https://doi.org/10.1080/10962247.2016.1171263, 2016.

Atkinson, R. and Arey, J.: Atmospheric Degradation of Volatile Organic Compounds, Chemical Reviews, 103, 4605–4638, https://doi.org/10.1021/cr0206420, 2003.

Atkinson, R. and Aschmann, S. M.: Rate constants for the reactions of O3 and OH radicals with a series of alkynes, International Journal of Chemical Kinetics, 16, 259–268, https://doi.org/10.1002/kin.550160308, 1984.

Barkley, Z., Davis, K., Miles, N., Richardson, S., Deng, A., Hmiel, B., Lyon, D., and Lauvaux, T.: Quantification of oil and gas methane emissions in the Delaware and Marcellus basins using a network of continuous tower-based measurements, Atmospheric Chemistry and Physics, 23, 6127–6144, https://doi.org/10.5194/acp-23-6127-2023, 2023.

Benck, K. M., Allen, K., Nadeau, A. J., Hutchins, H., Davis, A. M., and Robertson, A.: Carlsbad Caverns National Park: Natural resource condition assessment, Natural Resource Report NPS/CAVE/NRR 1466, National Park Service, Fort Collins, Colorado, 2017.

Benedict, K. B., Zhou, Y., Sive, B. C., Prenni, A. J., Gebhart, K. A., Fischer, E. V., Evanoski-Cole, A., Sullivan, A. P., Callahan, S., Schichtel, B. A., Mao, H., Zhou, Y., and Collett Jr., J. L.: Volatile organic compounds and ozone in Rocky Mountain National Park during FRAPPÉ, Atmospheric Chemistry and Physics, 19, 499–521, https://doi.org/10.5194/acp-19-499-2019, 2019.

Benedict, K. B., Prenni, A. J., El-Sayed, M. M., Hecobian, A., Zhou, Y., Gebhart, K. A., Sive, B. C., Schichtel, B. A., and Collett, J. L.: Volatile organic compounds and ozone at four national parks in the southwestern United States, Atmospheric Environment, 239, 117 783, https://doi.org/10.1016/j.atmosenv.2020.117783, 2020.

Berezina, E., Moiseenko, K., Skorokhod, A., Pankratova, N. V., Belikov, I., Belousov, V., and Elansky, N. F.: Impact of VOCs and NOx on Ozone Formation in Moscow, Atmosphere, 11, 1262, https://doi.org/10.3390/atmos11111262, 2020.

Bertman, S. B., Roberts, J. M., Parrish, D. D., Buhr, M. P., Goldan, P. D., Kuster, W. C., Fehsenfeld, F. C., Montzka, S. A., and Westberg, H.: Evolution of alkyl nitrates with air mass age, Journal of Geophysical Research, 100, 22 805, https://doi.org/10.1029/95JD02030, 1995.

Cardelino, C. and Chameides, W.: An Observation-Based Model for Analyzing Ozone Precursor Relationships in the Urban Atmosphere, Journal of the Air & Waste Management Association, 45, 161–180, https://doi.org/10.1080/10473289.1995.10467356, 1995.

Carter, W. P. and Seinfeld, J. H.: Winter ozone formation and VOC incremental reactivities in the Upper Green River Basin of Wyoming, Atmospheric Environment, 50, 255–266, https://doi.org/10.1016/j.atmosenv.2011.12.025, 2012.

Carter, W. P. L. and Atkinson, R.: Computer modeling study of incremental hydrocarbon reactivity, Enivornmental Science & Technology, 23, 864–880, https://doi.org/https://doi.org/10.1021/es00065a017, 1989.

Chen, T., Xue, L., Zheng, P., Zhang, Y., Liu, Y., Sun, J., Han, G., Li, H., Zhang, X., Li, Y., Li, H., Dong, C., Xu, F., Zhang, Q., and Wang, W.: Volatile organic compounds and ozone air pollution in an oil production region in northern China, Atmospheric Chemistry and Physics, 20, 7069–7086, https://doi.org/10.5194/acp-20-7069-2020, 2020.

Cohen, A. J., Brauer, M., Burnett, R., Anderson, H. R., Frostad, J., Estep, K., Balakrishnan, K., Brunekreef, B., Dandona, L., Dandona, R., Feigin, V., Freedman, G., Hubbell, B., Jobling, A., Kan, H., Knibbs, L., Liu, Y., Martin, R., Morawska, L., Pope, C. A., Shin, H., Straif, K., Shaddick, G., Thomas, M., Van Dingenen, R., Van Donkelaar, A., Vos, T., Murray, C. J. L., and Forouzanfar, M. H.: Estimates and 25-year trends of the global burden of disease attributable to ambient air pollution: an analysis of data from the Global Burden of Diseases Study 2015, The Lancet, 389, 1907–1918, https://doi.org/10.1016/S0140-6736(17)30505-6, 2017.

Crosman, E.: Meteorological Drivers of Permian Basin Methane Anomalies Derived from TROPOMI, Remote Sensing, 13, 896, https://doi.org/10.3390/rs13050896, 2021.

Dalsøren, S. B., Myhre, G., Hodnebrog, , Myhre, C. L., Stohl, A., Pisso, I., Schwietzke, S., Höglund-Isaksson, L., Helmig, D., Reimann, S., Sauvage, S., Schmidbauer, N., Read, K. A., Carpenter, L. J., Lewis, A. C., Punjabi, S., and Wallasch, M.: Discrepancy between simulated and observed ethane and propanelevels explained by underestimated fossil emissions, Nature Geoscience, 11, 178–184, https://doi.org/10.1038/s41561-018-0073-0, 2018.

Day, D. A., Dillon, M. B., Wooldridge, P. J., Thornton, J. A., Rosen, R. S., Wood, E. C., and Cohen, R. C.: On alkyl nitrates, O3 , and the “missing NOy", Journal of Geophysical Research, 108, 4501, https://doi.org/10.1029/2003JD003685, 2003.

Dix, B., De Bruin, J., Roosenbrand, E., Vlemmix, T., Francoeur, C., Gorchov-Negron, A., McDonald, B., Zhizhin, M., Elvidge, C., Veefkind, P., Levelt, P., and De Gouw, J.: Nitrogen Oxide

Emissions from U.S. Oil and Gas Production: Recent Trends and Source Attribution, Geophysical Research Letters, 47, e2019GL085 866, https://doi.org/10.1029/2019GL085866, 2020.

Dix, B., Francoeur, C., Li, M., Serrano-Calvo, R., Levelt, P. F., Veefkind, J. P., McDonald, B. C., and De Gouw, J.: Quantifying NO $_x$ Emissions from U.S. Oil and Gas Production Regions Using TROPOMI NO $_2$, ACS Earth and Space Chemistry, 6, 403–414, https://doi.org/10.1021/acsearthspacechem.1c00387, 2022.

Edwards, P. M., Young, C. J., Aikin, K., deGouw, J., Dubé, W. P., Geiger, F., Gilman, J., Helmig, D., Holloway, J. S., Kercher, J., Lerner, B., Martin, R., McLaren, R., Parrish, D. D., Peischl, J., Roberts, J. M., Ryerson, T. B., Thornton, J., Warneke, C., Williams, E. J., and Brown, S. S.: Ozone photochemistry in an oil and natural gas extraction region during winter: simulations of a snow-free season in the Uintah Basin, Utah, Atmospheric Chemistry and Physics, 13, 8955–8971, https://doi.org/10.5194/acp-13-8955-2013, 2013.

Edwards, P. M., Brown, S. S., Roberts, J. M., Ahmadov, R., Banta, R. M., deGouw, J. A., Dubé, W. P., Field, R. A., Flynn, J. H., Gilman, J. B., Graus, M., Helmig, D., Koss, A., Langford, A. O., Lefer, B. L., Lerner, B. M., Li, R., Li, S.-M., McKeen, S. A., Murphy, S. M., Parrish, D. D., Senff, C. J., Soltis, J., Stutz, J., Sweeney, C., Thompson, C. R., Trainer, M. K., Tsai, C., Veres, P. R., Washenfelder, R. A., Warneke, C., Wild, R. J., Young, C. J., Yuan, B., and Zamora, R.: High winter ozone pollution from carbonyl photolysis in an oil and gas basin, Nature, 514, 351–354, https://doi.org/10.1038/nature13767, 2014.

Ericson, S., Engel-Cox, J., and Arent, D.: Approaches for Integrating Renewable Energy Technologies in Oil and Gas Operations, Technical Report, Joint Institue for Strategic Energy Analysis, Golden, Colorado, 2019.

Fahey, D. W., Hübler, G., Parrish, D. D., Williams, E. J., Norton, R. B., Ridley, B. A., Singh, H. B., Liu, S. C., and Fehsenfeld, F. C.: Reactive nitrogen species in the troposphere: Measurements of NO, NO $_2$, HNO $_3$, particulate nitrate, peroxyacetyl nitrate (PAN), O $_3$, and total reactive odd nitrogen (NO $_y$) at Niwot Ridge, Colorado, Journal of Geophysical Research, 91, 9781, https://doi.org/10.1029/JD091iD09p09781, 1986.

Fedak, K. M., Good, N., Dahlke, J., Hecobian, A., Sullivan, A., Zhou, Y., Peel, J. L., and Volckens, J.: Chemical Composition and Emissions Factors for Cookstove Startup (Ignition) Materials, Environmental Science & Technology, 52, 9505–9513, https://doi.org/10.1021/acs.est.8b02218, 2018.

Finlayson-Pitts, B. J. and Pitts, J. N. J.: Chemistry of the Upper and Lower Atmosphere, Academic Press, 2000.

Flocke, F. M., Weinheimer, A. J., Swanson, A. L., Roberts, J. M., Schmitt, R., and Shertz, S.: On the Measurement of PANs by Gas Chromatography and Electron Capture Detection, Journal of Atmospheric Chemistry, 52, 19–43, https://doi.org/10.1007/s10874-005-6772-0, 2005.

Francoeur, C. B., McDonald, B. C., Gilman, J. B., Zarzana, K. J., Dix, B., Brown, S. S., De Gouw, J. A., Frost, G. J., Li, M., McKeen, S. A., Peischl, J., Pollack, I. B., Ryerson, T. B., Thompson, C., Warneke, C., and Trainer, M.: Quantifying Methane and Ozone Precursor Emissions from

Oil and Gas Production Regions across the Contiguous US, Environmental Science & Technology, 55, 9129–9139, https://doi.org/10.1021/acs.est.0c07352, 2021.

Gaudel, A., Cooper, O. R., Ancellet, G., Barret, B., Boynard, A., Burrows, J. P., Clerbaux, C., Coheur, P.-F., Cuesta, J., Cuevas, E., Doniki, S., Dufour, G., Ebojie, F., Foret, G., Garcia, O., Granados-Muñoz, M. J., Hannigan, J. W., Hase, F., Hassler, B., Huang, G., Hurtmans, D., Jaffe, D., Jones, N., Kalabokas, P., Kerridge, B., Kulawik, S., Latter, B., Leblanc, T., Le Flochmoën, E., Lin, W., Liu, J., Liu, X., Mahieu, E., McClure-Begley, A., Neu, J. L., Osman, M., Palm, M., Petetin, H., Petropavlovskikh, I., Querel, R., Rahpoe, N., Rozanov, A., Schultz, M. G., Schwab, J., Siddans, R., Smale, D., Steinbacher, M., Tanimoto, H., Tarasick, D. W., Thouret, V., Thompson, A. M., Trickl, T., Weatherhead, E., Wespes, C., Worden, H. M., Vigouroux, C., Xu, X., Zeng, G., and Ziemke, J.: Tropospheric Ozone Assessment Report: Present-day distribution and trends of tropospheric ozone relevant to climate and global atmospheric chemistry model evaluation, Elementa: Science of the Anthropocene, 6, 39, https://doi.org/10.1525/elementa.291, 2018.

Gelaro, R., McCarty, W., Suárez, M. J., Todling, R., Molod, A., Takacs, L., Randles, C. A., Darmenov, A., Bosilovich, M. G., Reichle, R., Wargan, K., Coy, L., Cullather, R., Draper, C., Akella, S., Buchard, V., Conaty, A., Da Silva, A. M., Gu, W., Kim, G.-K., Koster, R., Lucchesi, R., Merkova, D., Nielsen, J. E., Partyka, G., Pawson, S., Putman, W., Rienecker, M., Schubert, S. D., Sienkiewicz, M., and Zhao, B.: The Modern-Era Retrospective Analysis for Research and Applications, Version 2 (MERRA-2), Journal of Climate, 30, 5419–5454, https://doi.org/10.1175/JCLI-D-16-0758.1, 2017.

Gilman, J. B., Lerner, B. M., Kuster, W. C., and De Gouw, J. A.: Source Signature of Volatile Organic Compounds from Oil and Natural Gas Operations in Northeastern Colorado, Environmental Science & Technology, 47, 1297–1305, https://doi.org/10.1021/es304119a, 2013.

He, C., Lu, X., Wang, H., Wang, H., Li, Y., He, G., He, Y., Wang, Y., Zhang, Y., Liu, Y., Fan, Q., and Fan, S.: The unexpected high frequency of nocturnal surface ozone enhancement events over China: characteristics and mechanisms, Atmospheric Chemistry and Physics, 22, 15 243–15 261, https://doi.org/10.5194/acp-22-15243-2022, 2022.

Helmig, D., Rossabi, S., Hueber, J., Tans, P., Montzka, S. A., Masarie, K., Thoning, K., Plass-Duelmer, C., Claude, A., Carpenter, L. J., Lewis, A. C., Punjabi, S., Reimann, S., Vollmer, M. K., Steinbrecher, R., Hannigan, J. W., Emmons, L. K., Mahieu, E., Franco, B., Smale, D., and Pozzer, A.: Reversal of global atmospheric ethane and propane trends largely due to US oil and natural gas production, Nature Geoscience, 9, 490–495, https://doi.org/10.1038/ngeo2721, 2016.

Hogsett, W. E., Weber, J. E., and Tingey, D.: ENVIRONMENTAL AUDITING: An Approach for Characterizing Tropospheric Ozone Risk to Forests, Environmental Management, 21, 105–120, https://doi.org/10.1007/s002679900010, 1997.

Hynes, A. J. and Wine, P. H.: Kinetics and mechanism of the reaction of hydroxyl radicals with acetonitrile under atmospheric conditions, The Journal of Physical Chemistry, 95, 1232–1240, https://doi.org/10.1021/j100156a037, 1991.

Jaffe, D. A., Ninneman, M., and Chan, H. C.: NO $_x$ and O $_3$ Trends at U.S. Non-Attainment Areas for 1995–2020: Influence of COVID-19 Reductions and Wildland Fires on Policy-Relevant Concentrations, Journal of Geophysical Research: Atmospheres, 127, e2021JD036 385, https://doi.org/10.1029/2021JD036385, 2022.

Jenkin, M. E., Young, J. C., and Rickard, A. R.: The MCM v3.3.1 degradation scheme for isoprene, Atmospheric Chemistry and Physics, 15, 11 433–11 459, https://doi.org/10.5194/acp-15-11433-2015, 2015.

Jin, X. and Holloway, T.: Spatial and temporal variability of ozone sensitivity over China observed from the Ozone Monitoring Instrument: OZONE SENSITIVITY OVER CHINA, Journal of Geophysical Research: Atmospheres, 120, 7229–7246, https://doi.org/10.1002/2015JD023250, 2015.

Kaiser, J., Skog, K. M., Baumann, K., Bertman, S. B., Brown, S. B., Brune, W. H., Crounse, J. D., De Gouw, J. A., Edgerton, E. S., Feiner, P. A., Goldstein, A. H., Koss, A., Misztal, P. K., Nguyen, T. B., Olson, K. F., St. Clair, J. M., Teng, A. P., Toma, S., Wennberg, P. O., Wild, R. J., Zhang, L., and Keutsch, F. N.: Speciation of OH reactivity above the canopy of an isoprene-dominated forest, Atmospheric Chemistry and Physics, 16, 9349–9359, https://doi.org/10.5194/acp-16-9349-2016, 2016.

Kaser, L., Patton, E. G., Pfister, G. G., Weinheimer, A. J., Montzka, D. D., Flocke, F., Thompson, A. M., Stauffer, R. M., and Halliday, H. S.: The effect of entrainment through atmospheric boundary layer growth on observed and modeled surface ozone in the Colorado Front Range, Journal of Geophysical Research: Atmospheres, 122, 6075–6093, https://doi.org/10.1002/2016JD026245, 2017.

Kim, H., Park, R. J., Kim, S., Brune, W. H., Diskin, G. S., Fried, A., Hall, S. R., Weinheimer, A. J., Wennberg, P., Wisthaler, A., Blake, D. R., and Ullmann, K.: Observed versus simulated OH reactivity during KORUS-AQ campaign: Implications for emission inventory and chemical environment in East Asia, Elementa: Science of the Anthropocene, 10, 00 030, https://doi.org/10.1525/elementa.2022.00030, 2022.

Kleinman, L. I.: The dependence of tropospheric ozone production rate on ozone precursors, Atmospheric Environment, 39, 575–586, https://doi.org/10.1016/j.atmosenv.2004.08.047, 2005.

Kleinman, L. I., Daum, P. H., Imre, D. G., Lee, J. H., Lee, Y.-N., Nunnermacker, L. J., Springston, S. R., Weinstein-Lloyd, J., and Newman, L.: Ozone production in the New York City urban plume, Journal of Geophysical Research: Atmospheres, 105, 14 495–14 511, https://doi.org/10.1029/2000JD900011, 2000.

Kleinman, L. I., Springston, S. R., Daum, P. H., Weinstein-Lloyd, J., Alexander, M. L., Hubbe, J., Ortega, J., Canagaratna, M. R., and Jayne, J.: The time evolution of aerosol composition over the Mexico City plateau, Atmos. Chem. Phys., 8, https://doi.org/https://doi.org/10.5194/acp-8-1559-2008, 2008.

Kohut, R.: Assessing the risk of foliar injury from ozone on vegetation in parks in the U.S. National Park Service's Vital Signs Network, Environmental Pollution, 149, 348–357, https://doi.org/10.1016/j.envpol.2007.04.022, 2007.

Koplitz, S., Simon, H., Henderson, B., Liljegren, J., Tonnesen, G., Whitehill, A., and Wells, B.: Changes in Ozone Chemical Sensitivity in the United States from 2007 to 2016, ACS Environmental Au, 2, 206–222, https://doi.org/10.1021/acsenvironau.1c00029, 2022.

Kort, E. A., Smith, M. L., Murray, L. T., Gvakharia, A., Brandt, A. R., Peischl, J., Ryerson, T. B., Sweeney, C., and Travis, K.: Fugitive emissions from the Bakken shale illustrate role of shale production in global ethane shift, Geophysical Research Letters, 43, 4617–4623, https://doi.org/10.1002/2016GL068703, 2016.

Lee, Y., Huey, L. G., Wang, Y., Qu, H., Zhang, R., Ji, Y., Tanner, D. J., Wang, X., Tang, J., Song, W., Hu, W., and Zhang, Y.: Photochemistry of Volatile Organic Compounds in the Yellow River Delta, China: Formation of O_3 and Peroxyacyl Nitrates, Journal of Geophysical Research: Atmospheres, 126, e2021JD035 296, https://doi.org/10.1029/2021JD035296, 2021.

Li, S.-M., Leithead, A., Moussa, S. G., Liggio, J., Moran, M. D., Wang, D., Hayden, K., Darlington, A., Gordon, M., Staebler, R., Makar, P. A., Stroud, C. A., McLaren, R., Liu, P. S. K., O'Brien, J., Mittermeier, R. L., Zhang, J., Marson, G., Cober, S. G., Wolde, M., and Wentzell, J. J. B.: Differences between measured and reported volatile organic compound emissions from oil sands facilities in Alberta, Canada, Proceedings of the National Academy of Sciences, 114, https://doi.org/10.1073/pnas.1617862114, 2017.

Lin, J., Youn, D., Liang, X., and Wuebbles, D.: Global model simulation of summertime U.S. ozone diurnal cycle and its sensitivity to PBL mixing, spatial resolution, and emissions, Atmospheric Environment, 42, 8470–8483, https://doi.org/10.1016/j.atmosenv.2008.08.012, 2008.

Lindaas, J., Farmer, D. K., Pollack, I. B., Abeleira, A., Flocke, F., and Fischer, E. V.: Acyl Peroxy Nitrates Link Oil and Natural Gas Emissions to High Ozone Abundances in the Colorado Front Range During Summer 2015, Journal of Geophysical Research: Atmospheres, 124, 2336–2350, https://doi.org/10.1029/2018JD028825, 2019.

Lu, X., Jacob, D. J., Zhang, Y., Shen, L., Sulprizio, M. P., Maasakkers, J. D., Varon, D. J., Qu, Z., Chen, Z., Hmiel, B., Parker, R. J., Boesch, H., Wang, H., He, C., and Fan, S.: Observation-derived 2010-2019 trends in methane emissions and intensities from US oil and gas fields tied to activity metrics, Proceedings of the National Academy of Sciences, 120, e2217900 120, https://doi.org/10.1073/pnas.2217900120, 2023.

Mao, J., Ren, X., Chen, S., Brune, W. H., Chen, Z., Martinez, M., Harder, H., Lefer, B., Rappenglück, B., Flynn, J., and Leuchner, M.: Atmospheric oxidation capacity in the summer of Houston 2006: Comparison with summer measurements in other metropolitan studies, Atmospheric Environment, 44, 4107–4115, https://doi.org/10.1016/j.atmosenv.2009.01.013, 2010.

Mao, J., Fan, S., Jacob, D. J., and Travis, K. R.: Radical loss in the atmosphere from Cu-Fe redox coupling in aerosols, Atmospheric Chemistry and Physics, 13, 509–519, https://doi.org/10.5194/acp-13-509-2013, 2013.

Mayhew, A. W., Lee, B. H., Thornton, J. A., Bannan, T. J., Brean, J., Hopkins, J. R., Lee, J. D., Nelson, B. S., Percival, C., Rickard, A. R., Shaw, M. D., Edwards, P. M., and Hamilton, J. F.: Evaluation of isoprene nitrate chemistry in detailed chemical mechanisms, Atmospheric Chemistry and Physics, 22, 14 783–14 798, https://doi.org/10.5194/acp-22-14783-2022, 2022.

McDuffie, E. E., Edwards, P. M., Gilman, J. B., Lerner, B. M., Dubé, W. P., Trainer, M., Wolfe, D. E., Angevine, W. M., deGouw, J., Williams, E. J., Tevlin, A. G., Murphy, J. G., Fischer, E. V., McKeen, S., Ryerson, T. B., Peischl, J., Holloway, J. S., Aikin, K., Langford, A. O., Senff, C. J., Alvarez, R. J., Hall, S. R., Ullmann, K., Lantz, K. O., and Brown, S. S.: Influence of oil and gas emissions on summertime ozone in the Colorado Northern Front Range: COLORADO O&G AND SUMMERTIME OZONE, Journal of Geophysical Research: Atmospheres, 121, 8712–8729, https://doi.org/10.1002/2016JD025265, 2016.

McGaughey, G. R., Desai, N. R., Allen, D. T., Seila, R. L., Lonneman, W. A., Fraser, M. P., Harley, R. A., Pollack, A. K., Ivy, J. M., and Price, J. H.: Analysis of motor vehicle emissions in a Houston tunnel during the Texas Air Quality Study 2000, Atmospheric Environment, 38, 3363–3372, https://doi.org/10.1016/j.atmosenv.2004.03.006, 2004.

Monks, P. S., Archibald, A. T., Colette, A., Cooper, O., Coyle, M., Derwent, R., Fowler, D., Granier, C., Law, K. S., Mills, G. E., Stevenson, D. S., Tarasova, O., Thouret, V., Von Schneidemesser, E., Sommariva, R., Wild, O., and Williams, M. L.: Tropospheric ozone and its precursors from the urban to the global scale from air quality to short-lived climate forcer, Atmospheric Chemistry and Physics, 15, 8889–8973, https://doi.org/10.5194/acp-15-8889-2015, 2015.

Morris, G. A., Ford, B., Rappenglück, B., Thompson, A. M., Mefferd, A., Ngan, F., and Lefer, B.: An evaluation of the interaction of morning residual layer and afternoon mixed layer ozone in Houston using ozonesonde data, Atmospheric Environment, 44, 4024–4034, https://doi.org/10.1016/j.atmosenv.2009.06.057, 2010.

Naimie, L. E., Sullivan, A. P., Benedict, K., Prenni, A. J., Sive, B., Schichtel, B. A., Fischer, E. V., Pollack, I., and Collett, J.: PM $_{2.5}$ in Carlsbad Caverns National Park: Composition, sources, and visibility impacts, Journal of the Air & Waste Management Association, 72, 1201–1218, https://doi.org/10.1080/10962247.2022.2081634, 2022.

Nelson, B. S., Stewart, G. J., Drysdale, W. S., Newland, M. J., Vaughan, A. R., Dunmore, R. E., Edwards, P. M., Lewis, A. C., Hamilton, J. F., Acton, W. J., Hewitt, C. N., Crilley, L. R., Alam, M. S., Şahin, A., Beddows, D. C. S., Bloss, W. J., Slater, E., Whalley, L. K., Heard, D. E., Cash, J. M., Langford, B., Nemitz, E., Sommariva, R., Cox, S., Shivani, Gadi, R., Gurjar, B. R., Hopkins, J. R., Rickard, A. R., and Lee, J. D.: In situ ozone production is highly sensitive to volatile organic compounds in Delhi, India, Atmospheric Chemistry and Physics, 21, 13 609–13 630, https://doi.org/10.5194/acp-21-13609-2021, 2021.

Neuman, J. A., Ryerson, T. B., Huey, L. G., Jakoubek, R., Nowak, J. B., Simons, C., and Fehsenfeld, F. C.: Calibration and Evaluation of Nitric Acid and Ammonia Permeation Tubes by UV Optical Absorption, Environmental Science & Technology, 37, 2975–2981, https://doi.org/10.1021/es026422l, 2003.

Ninneman, M. and Jaffe, D. A.: The impact of wildfire smoke on ozone production in an urban area: Insights from field observations and photochemical box modeling, Atmospheric Environment, 267, 118 764, https://doi.org/10.1016/j.atmosenv.2021.118764, 2021.

Orkin, V. L., Khamaganov, V. G., Kozlov, S. N., and Kurylo, M. J.: Measurements of Rate Constants for the OH Reactions with Bromoform ($CHBr_3$), $CHBr_2Cl$, $CHBrCl_2$, and Epichlorohydrin (C_3H_5ClO), The Journal of Physical Chemistry A, 117, 3809–3818, https://doi.org/10.1021/jp3128753, 2013.

Orlando, J. J., Tyndall, G. S., Wallington, T. J., and Dill, M.: Atmospheric chemistry of CH2BR2: Rate coefficients for its reaction with Cl atoms and OH and the chemistry of the CHBr2O radical, International Journal of Chemical Kinetics, 28, 433–442, https://doi.org/10.1002/(SICI)1097-4601(1996)28:6<433::AID-KIN5>3.0.CO;2-W, 1996.

Paatero, P.: Least squares formulation of robust non-negative factor analysis, Chemometrics and Intelligent Laboratory Systems, 37, 23–35, https://doi.org/10.1016/S0169-7439(96)00044-5, 1997.

Pan, D., Pollack, I. B., Sive, B. C., Marsavin, A., Naimie, L. E., Benedict, K., Zhou, Y., Sullivan, A. P., Prenni, A. J., Cope, E. J., Juncosa Calahorrano, J. F., Fischer, E. V., Prenni, A. J., Schichtel, B. A., and Collett Jr., J. L.: Source Characterization of Volatile Organic Compounds at Carlsbad Caverns National Park, Journal of the Air & Waste Management Association, https://doi.org/https://doi.org/10.1080/10962247.2023.2266696, 2023.

Pan, X., Kanaya, Y., Tanimoto, H., Inomata, S., Wang, Z., Kudo, S., and Uno, I.: Examining the major contributors of ozone pollution in a rural area of the Yangtze River Delta region during harvest season, Atmospheric Chemistry and Physics, 15, 6101–6111, https://doi.org/10.5194/acp-15-6101-2015, 2015.

Pelgrum, H., Schmugge, T., Rango, A., Ritchie, J., and Kustas, B.: Length-Scale analysis of surface albedo, temperature, and normalized difference vegetation index in desert grassland, Water Resources Research, 36, 1757–1765, https://doi.org/10.1029/2000WR900028, 2000.

Pollack, I. B., Pan, D., Marsavin, A., Cope, E. J., Juncosa Calahorrano, J. F., Naimie, L. E., Benedict, K., Sullivan, A. P., Zhou, Y., Sive, B. C., Prenni, A. J., Schichtel, B. A., Collett Jr., J. L., and Fischer, E. V.: Observations of ozone, acyl peroxy nitrates, and their precursors during summer 2019 at Carlsbad Caverns National Park, New Mexico, Journal of the Air & Waste Management Association, https://doi.org/https://doi.org/10.1080/10962247.2023.2271436, 2023.

Porter, W. C. and Heald, C. L.: The mechanisms and meteorological drivers of the summertime ozone–temperature relationship, Atmospheric Chemistry and Physics, 19, 13 367–13 381, https://doi.org/10.5194/acp-19-13367-2019, 2019.

Pozzer, A., Schultz, M. G., and Helmig, D.: Impact of U.S. Oil and Natural Gas Emission Increases on Surface Ozone Is Most Pronounced in the Central United States, Environmental Science & Technology, 54, 12 423–12 433, https://doi.org/10.1021/acs.est.9b06983, 2020.

Riaz, M., Kontogeorgis, G. M., Stenby, E. H., Yan, W., Haugum, T., Christensen, K. O., Løkken, T. V., and Solbraa, E.: Measurement of Liquid–Liquid Equilibria for Condensate + Glycol and Condensate + Glycol + Water Systems, Journal of Chemical & Engineering Data, 56, 4342–4351, https://doi.org/10.1021/je200158c, 2011.

Rickly, P. S., Coggon, M. M., Aikin, K. C., Alvarez, R. J., Baidar, S., Gilman, J. B., Gkatzelis, G. I., Harkins, C., He, J., Lamplugh, A., Langford, A. O., McDonald, B. C., Peischl, J., Robinson, M. A., Rollins, A. W., Schwantes, R. H., Senff, C. J., Warneke, C., and Brown, S. S.: Influence of Wildfire on Urban Ozone: An Observationally Constrained Box Modeling Study at a Site in the Colorado Front Range, Environmental Science & Technology, 57, 1257–1267, https://doi.org/10.1021/acs.est.2c06157, 2023.

Robertson, A. M., Edie, R., Field, R. A., Lyon, D., McVay, R., Omara, M., Zavala-Araiza, D., and Murphy, S. M.: New Mexico Permian Basin Measured Well Pad Methane Emissions Are a Factor of 5–9 Times Higher Than U.S. EPA Estimates, Environmental Science & Technology, 54, 13 926–13 934, https://doi.org/10.1021/acs.est.0c02927, 2020.

Rubin, J. I., Kean, A. J., Harley, R. A., Millet, D. B., and Goldstein, A. H.: Temperature dependence of volatile organic compound evaporative emissions from motor vehicles, Journal of Geophysical Research, 111, D03 305, https://doi.org/10.1029/2005JD006458, 2006.

Russo, R. S., Zhou, Y., White, M. L., Mao, H., Talbot, R., and Sive, B. C.: Multi-year (2004–2008) record of nonmethane hydrocarbons and halocarbons in New England: seasonal variations and regional sources, Atmospheric Chemistry and Physics, 10, 4909–4929, https://doi.org/10.5194/acp-10-4909-2010, 2010.

Sakamoto, Y., Sadanaga, Y., Li, J., Matsuoka, K., Takemura, M., Fujii, T., Nakagawa, M., Kohno, N., Nakashima, Y., Sato, K., Nakayama, T., Kato, S., Takami, A., Yoshino, A., Murano, K., and Kajii, Y.: Relative and Absolute Sensitivity Analysis on Ozone Production in Tsukuba, a City in Japan, Environmental Science & Technology, 53, 13 629–13 635, https://doi.org/10.1021/acs.est.9b03542, 2019.

Schroeder, J. R., Crawford, J. H., Fried, A., Walega, J., Weinheimer, A., Wisthaler, A., Müller, M., Mikoviny, T., Chen, G., Shook, M., Blake, D. R., and Tonnesen, G. S.: New insights into the column CH_2O/NO_2 ratio as an indicator of near-surface ozone sensitivity: CH_2O/NO_2 as Indicator of O_3 Sensitivity, Journal of Geophysical Research: Atmospheres, 122, 8885–8907, https://doi.org/10.1002/2017JD026781, 2017.

Serrano-Calvo, R., Veefkind, J. P., Dix, B., De Gouw, J., and Levelt, P. F.: COVID-19 Impact on the Oil and Gas Industry NO_2 Emissions: A Case Study of the Permian Basin, Journal of Geophysical Research: Atmospheres, 128, e2023JD038 566, https://doi.org/10.1029/2023JD038566, 2023.

Shaw, J. T., Rickard, A. R., Newland, M. J., and Dillon, T. J.: Rate coefficients for reactions of OH with aromatic and aliphatic volatile organic compounds determined by the multivariate relative rate technique, Atmospheric Chemistry and Physics, 20, 9725–9736, https://doi.org/10.5194/acp-20-9725-2020, 2020.

Sillman, S.: The relation between ozone, NOx and hydrocarbons in urban and polluted rural environments, Atmospheric Environment, 33, 1821–1845, https://doi.org/https://doi.org/10.1016/S1352-2310(98)00345-8, 1999.

Sillman, S. and He, D.: Some theoretical results concerning O_3-NO_x-VOC chemistry and NO_x-VOC indicators, Journal of Geophysical Research, 107, 4659, https://doi.org/10.1029/2001JD001123, 2002.

Sillman, S. and West, J. J.: Reactive nitrogen in Mexico City and its relation to ozone-precursor sensitivity: results from photochemical models, Atmos. Chem. Phys., pp. 3477–3489, https://doi.org/https://doi.org/10.5194/acp-9-3477-2009, 2009.

Simon, H., Reff, A., Wells, B., Xing, J., and Frank, N.: Ozone Trends Across the United States over a Period of Decreasing NOx and VOC Emissions, Environmental Science & Technology, 49, 186–195, https://doi.org/10.1021/es504514z, 2015.

Sive, B. C., Zhou, Y., Troop, D., Wang, Y., Little, W. C., Wingenter, O. W., Russo, R. S., Varner, R. K., and Talbot, R.: Development of a Cryogen-Free Concentration System for Measurements of Volatile Organic Compounds, Analytical Chemistry, 77, 6989–6998, https://doi.org/10.1021/ac0506231, 2005.

Song, H., Lu, K., Dong, H., Tan, Z., Chen, S., Zeng, L., and Zhang, Y.: Reduced Aerosol Uptake of Hydroperoxyl Radical May Increase the Sensitivity of Ozone Production to Volatile Organic Compounds, Environmental Science & Technology Letters, 9, 22–29, https://doi.org/10.1021/acs.estlett.1c00893, 2022.

Souri, A. H., Johnson, M. S., Wolfe, G. M., Crawford, J. H., Fried, A., Wisthaler, A., Brune, W. H., Blake, D. R., Weinheimer, A. J., Verhoelst, T., Compernolle, S., Pinardi, G., Vigouroux, C., Langerock, B., Choi, S., Lamsal, L., Zhu, L., Sun, S., Cohen, R. C., Min, K.-E., Cho, C., Philip, S., Liu, X., and Chance, K.: Characterization of errors in satellite-based HCHO NO_2 tropospheric column ratios with respect to chemistry, column-to-PBL translation, spatial representation, and retrieval uncertainties, Atmospheric Chemistry and Physics, 23, 1963–1986, https://doi.org/10.5194/acp-23-1963-2023, 2023.

Sprengnether, M. M., Demerjian, K. L., Dransfield, T. J., Clarke, J. S., Anderson, J. G., and Donahue, N. M.: Rate Constants of Nine C6C9 Alkanes with OH from 230 to 379 K: Chemical Tracers for [OH], The Journal of Physical Chemistry A, 113, 5030–5038, https://doi.org/10.1021/jp810412m, 2009.

Stein, A. F., Draxler, R. R., Rolph, G. D., Stunder, B. J. B., Cohen, M. D., and Ngan, F.: NOAA's HYSPLIT Atmospheric Transport and Dispersion Modeling System, Bulletin of the American Meteorological Society, 96, 2059–2077, https://doi.org/10.1175/BAMS-D-14-00110.1, 2015.

Stockwell, W. R., Kirchner, F., Kuhn, M., and Seefeld, S.: A new mechanism for regional atmospheric chemistry modeling, Journal of Geophysical Research: Atmospheres, 102, 25 847–25 879, https://doi.org/10.1029/97JD00849, 1997.

Strode, S. A., Rodriguez, J. M., Logan, J. A., Cooper, O. R., Witte, J. C., Lamsal, L. N., Damon, M., Van Aartsen, B., Steenrod, S. D., and Strahan, S. E.: Trends and variability in surface ozone over the United States, Journal of Geophysical Research: Atmospheres, 120, 9020–9042, https://doi.org/10.1002/2014JD022784, 2015.

Swarthout, R. F., Russo, R. S., Zhou, Y., Hart, A. H., and Sive, B. C.: Volatile organic compound distributions during the NACHTT campaign at the Boulder Atmospheric Observatory: Influence of urban and natural gas sources: VOLATILE ORGANIC COMPOUNDS DURING NACHTT, Journal of Geophysical Research: Atmospheres, 118, 10,614–10,637, https://doi.org/10.1002/jgrd.50722, 2013.

Swarthout, R. F., Russo, R. S., Zhou, Y., Miller, B. M., Mitchell, B., Horsman, E., Lipsky, E., McCabe, D. C., Baum, E., and Sive, B. C.: Impact of Marcellus Shale Natural Gas Development in Southwest Pennsylvania on Volatile Organic Compound Emissions and Regional Air Quality, Environmental Science & Technology, 49, 3175–3184, https://doi.org/10.1021/es504315f, 2015.

Taylor, P. H., Jiang, Z., and Dellinger, B.: Determination of the gas-phase reactivity of hydroxyl with chlorinated methanes at high temperature: Effects of laser/thermal photochemistry, International Journal of Chemical Kinetics, 25, 9–23, https://doi.org/10.1002/kin.550250103, 1993.

Tichenor, L. B., El-Sinawi, A., Yamada, T., Taylor, P. H., Peng, J., Hu, X., and Marshall, P.: Kinetic studies of the reaction of hydroxyl radicals with trichloroethylene and tetrachloroethylene, Chemosphere, 42, 571–577, https://doi.org/10.1016/S0045-6535(00)00229-0, 2001.

Trainer, M., Parrish, D. D., Buhr, M. P., Norton, R. B., Fehsenfeld, F. C., Anlauf, K. G., Bottenheim, J. W., Tang, Y. Z., Wiebe, H. A., Roberts, J. M., Tanner, R. L., Newman, L., Bowersox, V. C., Meagher, J. F., Olszyna, K. J., Rodgers, M. O., Wang, T., Berresheim, H., Demerjian, K. L., and Roychowdhury, U. K.: Correlation of ozone with NO $_y$ in photochemically aged air, Journal of Geophysical Research: Atmospheres, 98, 2917–2925, https://doi.org/10.1029/92JD01910, 1993.

Tzompa-Sosa, Z. A. and Fischer, E. V.: Impacts of Emissions of C $_2$ -C $_5$ Alkanes From the U.S. Oil and Gas Sector on Ozone and Other Secondary Species, Journal of Geophysical Research: Atmospheres, 126, https://doi.org/10.1029/2019JD031935, 2021.

Veefkind, J. P., Serrano-Calvo, R., De Gouw, J., Dix, B., Schneising, O., Buchwitz, M., Barré, J., Van Der A, R. J., Liu, M., and Levelt, P. F.: Widespread Frequent Methane Emissions From the Oil and Gas Industry in the Permian Basin, Journal of Geophysical Research: Atmospheres, 128, e2022JD037 479, https://doi.org/10.1029/2022JD037479, 2023.

Wang, P., Chen, Y., Hu, J., Zhang, H., and Ying, Q.: Attribution of Tropospheric Ozone to NO $_x$ and VOC Emissions: Considering Ozone Formation in the Transition Regime, Environmental Science & Technology, 53, 1404–1412, https://doi.org/10.1021/acs.est.8b05981, 2019.

Wang, W., Yuan, B., Peng, Y., Su, H., Cheng, Y., Yang, S., Wu, C., Qi, J., Bao, F., Huangfu, Y., Wang, C., Ye, C., Wang, Z., Wang, B., Wang, X., Song, W., Hu, W., Cheng, P., Zhu, M., Zheng, J., and Shao, M.: Direct observations indicate photodegradable oxygenated volatile organic compounds (OVOCs) as larger contributors to radicals and ozone production in the atmosphere, Atmospheric Chemistry and Physics, 22, 4117–4128, https://doi.org/10.5194/acp-22-4117-2022, 2022.

Warneke, C., McKeen, S. A., De Gouw, J. A., Goldan, P. D., Kuster, W. C., Holloway, J. S., Williams, E. J., Lerner, B. M., Parrish, D. D., Trainer, M., Fehsenfeld, F. C., Kato, S., Atlas, E. L., Baker, A., and Blake, D. R.: Determination of urban volatile organic compound emission ratios and comparison with an emissions database, Journal of Geophysical Research: Atmospheres, 112, 2006JD007 930, https://doi.org/10.1029/2006JD007930, 2007.

Wilson, E. W., Hamilton, W. A., Kennington, H. R., Evans, B., Scott, N. W., and DeMore, W. B.: Measurement and Estimation of Rate Constants for the Reactions of Hydroxyl Radical with Several Alkanes and Cycloalkanes, The Journal of Physical Chemistry A, 110, 3593–3604, https://doi.org/10.1021/jp055841c, 2006.

Wolfe, G. M., Marvin, M. R., Roberts, S. J., Travis, K. R., and Liao, J.: The Framework for 0-D Atmospheric Modeling (F0AM) v3.1, Geoscientific Model Development, 9, 3309–3319, https://doi.org/10.5194/gmd-9-3309-2016, 2016.

Xiong, Y., Chai, J., Mao, H., Mariscal, N., Yacovitch, T., Lerner, B., Majluf, F., Canagaratna, M., Olaguer, E. P., and Huang, Y.: Examining the Summertime Ozone Formation Regime in Southeast Michigan Using MOOSE Ground-Based HCHO/NO $_2$ Measurements and F0AM Box Model, Journal of Geophysical Research: Atmospheres, 128, e2023JD038 943, https://doi.org/10.1029/2023JD038943, 2023.

Xu, W., Zhang, G., Wang, Y., Tong, S., Zhang, W., Ma, Z., Lin, W., Kuang, Y., Yin, L., and Xu, X.: Aerosol Promotes Peroxyacetyl Nitrate Formation During Winter in the North China Plain, Environmental Science & Technology, 55, 3568–3581, https://doi.org/10.1021/acs.est.0c08157, 2021.

Xue, L. K., Wang, T., Guo, H., Blake, D. R., Tang, J., Zhang, X. C., Saunders, S. M., and Wang, W. X.: Sources and photochemistry of volatile organic compounds in the remote atmosphere of western China: results from the Mt. Waliguan Observatory, Atmospheric Chemistry and Physics, 13, 8551–8567, https://doi.org/10.5194/acp-13-8551-2013, 2013.

Zaragoza, J., Callahan, S., McDuffie, E. E., Kirkland, J., Brophy, P., Durrett, L., Farmer, D. K., Zhou, Y., Sive, B., Flocke, F., Pfister, G., Knote, C., Tevlin, A., Murphy, J., and Fischer, E. V.: Observations of Acyl Peroxy Nitrates During the Front Range Air Pollution and Photochemistry Éxperiment (FRAPPÉ), Journal of Geophysical Research: Atmospheres, 122, https://doi.org/10.1002/2017JD027337, 2017.

Zare, A., Romer, P. S., Nguyen, T., Keutsch, F. N., Skog, K., and Cohen, R. C.: A comprehensive organic nitrate chemistry: insights into the lifetime of atmospheric organic nitrates, Atmospheric Chemistry and Physics, 18, 15 419–15 436, https://doi.org/10.5194/acp-18-15419-2018, 2018.

Zhang, J. J., Wei, Y., and Fang, Z.: Ozone Pollution: A Major Health Hazard Worldwide, Frontiers in Immunology, 10, 2518, https://doi.org/10.3389/fimmu.2019.02518, 2019.

Zhang, Y., Gautam, R., Pandey, S., Omara, M., Maasakkers, J. D., Sadavarte, P., Lyon, D., Nesser, H., Sulprizio, M. P., Varon, D. J., Zhang, R., Houweling, S., Zavala-Araiza, D., Alvarez, R. A., Lorente, A., Hamburg, S. P., Aben, I., and Jacob, D. J.: Quantifying methane emissions from the largest oil-producing basin in the United States from space, Science Advances, 6, eaaz5120, https://doi.org/10.1126/sciadv.aaz5120, 2020.

Zhou, Y., Varner, R. K., Russo, R. S., Wingenter, O. W., Haase, K. B., Talbot, R., and Sive, B. C.: Coastal water source of short-lived halocarbons in New England, Journal of Geophysical Research, 110, D21 302, https://doi.org/10.1029/2004JD005603, 2005.

Appendix A

Notes on 0-D model configuration

I worked with two different 0-D "box" models while analyzing CarCavAQS data: the Framework for 0-D Atmospheric Modeling (FOAM v4.2.2) and the Dynamically Simple Model for Atmospheric Chemical Complexity (DSMACC). Both models can be observationally constrained and configured to run with the Master Chemical Mechanism (MCM) and the Tropospheric Ultraviolet and Visible (TUV) radiation model. The key differences between them are the programming languages (FOAM uses MATLAB, while DSMACC uses FORTRAN), and the solvers (FOAM uses MATLAB's ode15s solver, while DSMACC uses the Kinetics Preprocessor (KPP)). While both models should yield similar results with the same observational constraints, I ultimately chose to use F0AM for this thesis because it offers built-in tools for tasks like imposing observational constraints from a .csv file, tracking all species with select functional groups (e.g., RO_2), tracking individual radical termination pathways (useful for calculating parameters like L_n/Q) and automatically converting model output concentrations to ppbv. These tools, while possible to implement into DSMACC, require editing of the FORTRAN source code. F0AM is also more consistently updated (v4.3 was released in August 2023) and comes with example setups, a detailed user manual, and an active discussion forum (https://sites.google.com/site/wolfegm/models). Here are some key considerations when setting up a box model:

- Dilution: this is one of the most uncertain model parameters. Ideally, you would have time-resolved measurements PBL height to inform how dilution/entrainment changes throughout the day. If this measurement is not available, reanalysis data (e.g., MERRA-2) can help. Some studies have scaled their dilution directly by the measured PBL height but found that a constant dilution rate is often enough to reasonably replicate observed concentrations of unconstrained species (e.g., Kaiser et al., 2016). Either way, some constraint on PBL height would still be useful for implementing a diurnally varying depositional loss rate for O_3.

- Background concentrations of O_3 and other secondary species: Implementing background concentrations simulates the entertainment of these species from the residual layer. While vertically resolved measurements of O_3 would be ideal for informing background concentrations, nighttime averages measured at the surface can work as decent approximations. Some studies have noted that the previous day's afternoon maximum O_3 (Morris et al., 2010)), or the nighttime average surface O_x (= NO_2 + O_x) concentrations (He et al., 2022) are good estimates of O_3 concentrations in the nighttime residual layer. Uncertainties associated with parameterizing entrainment may still persist even with a good constraint on background O_3 because of the way dilution and background O_3 are intertwined (having a 1st-order dilution rate (k_{dil}) and a fixed background concentration is equivalent to a 0th order source and a 1st-order sink; Equation A.1). Therefore it is always important to evaluate the model's sensitivity to these parameters.

$$\frac{d[O_3]}{dt} = -k_{\text{dil}}([O_3] - [O_3]_{\text{background}}) \tag{A.1}$$

- Data interpolation: Imposed observational constraints need to be complete with no data gaps. Depending on the species measured, different data interpolation approaches are appropriate. See the supplement of Kaiser et al. (2016) for an example approach and corresponding justifications.

- Model time step (integration time): It is advisable to keep the model time step shorter than 1 h (e.g., 10 min or 15 min). If your observational constraints have hourly resolution, these can be linearly interpolated to a finer resolution so that the model is still constrained at each time step. Having an integration time of 1 h may lead to unrealistic results since parameters like photolysis are going to be updated only once per h.

- Additional measurements: Some measurements that weren't available during CarCavAQS but would have been very valuable for constraining a box model include direct measurements of the NO_2 photolysis rate (j_{NO_2}) and possibly other photolysis rates (using a filter radiometer). These measurements can be used to directly verify and scale TUV-calculated clear-sky photolysis rates. Time-resolved measurements of HCHO, along with other photolabile OVOCs, would also be valuable due to their important roles as primary radical sources. Depending on the study area these compounds can have both primary and secondary sources, and therefore having observations available for model validation is crucial.

Included below is MATLAB code that can be used to run repeated F0AM simulations in sequence while scaling NO_x and VOC constraints (i.e., to produce an isopleth diagram). This code is based on an example found on the F0AM discussion forum provided by Dr. Glenn Wolfe. If using the "ExampleSetup_DielCycle.m" setup provided in the F0AM package, this block of code should go directly after the "INPUT REPLICATION AND INTERPOLATION" block:

```
%% PERTURBATIONS AND MAIN MODEL LOOP

NOx2perturb = {'NO','NO2'}; %list NOx constraints to perturb
NOxflag = ismember(InitConc(:,1), NOx2perturb);

VOC2perturb = {'C5H8','C2H6','C3H8','IC4H10','NC4H10','IC5H12','NC5H12','
   NC6H14','M3HEX','NC8H18','NC9H20','NC10H22','CHEX','C2H2','C2H4','C3H6','
   BUT1ENE','BENZENE','TOLUENE','EBENZ','METHTOL','MXYL','OXYL','PXYL','CHCL3
   ','TCE'}; %list all VOC species to perturb
VOCflag = ismember(InitConc(:,1), VOC2perturb);

NOxfactor = 0.1:0.1:2.0; %set up NOx scaling factors
VOCfactor = 0.1:0.1:2.0; %set up VOC scaling factors

for iNOx = 1:length(NOxfactor) %main model loop
    for iVOC = 1:length(VOCfactor)
        InitConcNow = InitConc; %initialize
        InitConcNow(NOxflag, 2) = cellfun(@(conc) NOxfactor(iNOx)*conc,
           InitConcNow(NOxflag,2),'UniformOutput',0); % multiply
           concentrations by factor
        InitConcNow(VOCflag, 2) = cellfun(@(conc) VOCfactor(iVOC)*conc,
           InitConcNow(VOCflag,2),'UniformOutput',0); % multiply
           concentrations by factor
        SaveName = ['S_NOx' num2str(iNOx) '_VOC' num2str(iVOC)]; %name for
           model output
        ModelOptions.SavePath = SaveName;
        S.(SaveName) = F0AM_ModelCore(Met,InitConcNow,ChemFiles,BkgdConc,
           ModelOptions); %call model
        SplitRun(S.(SaveName),'custom',repIndex);
        FileName = ['S_NOx' num2str(iNOx) '_VOC' num2str(iVOC)];
        save("insert path here" + string(FileName) +'.mat', '-struct', 'S2');
           %only save last 24 h (previous simulations are for model spin up)
    end
end
```

Appendix B

Supporting Figures

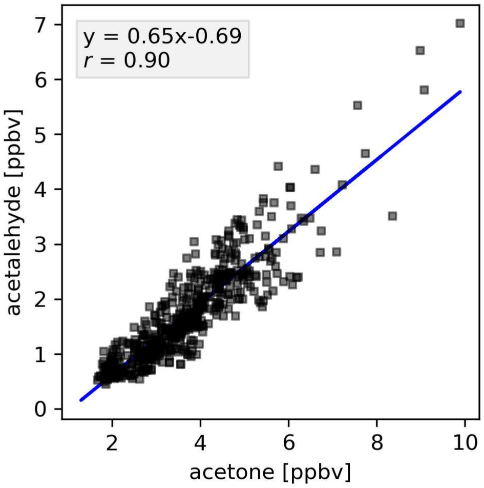

Figure B.1: Scatterplot of PTR-MS acetone vs. PTR-MS acetaldehyde. Data are fit with a linear least-squared regression.

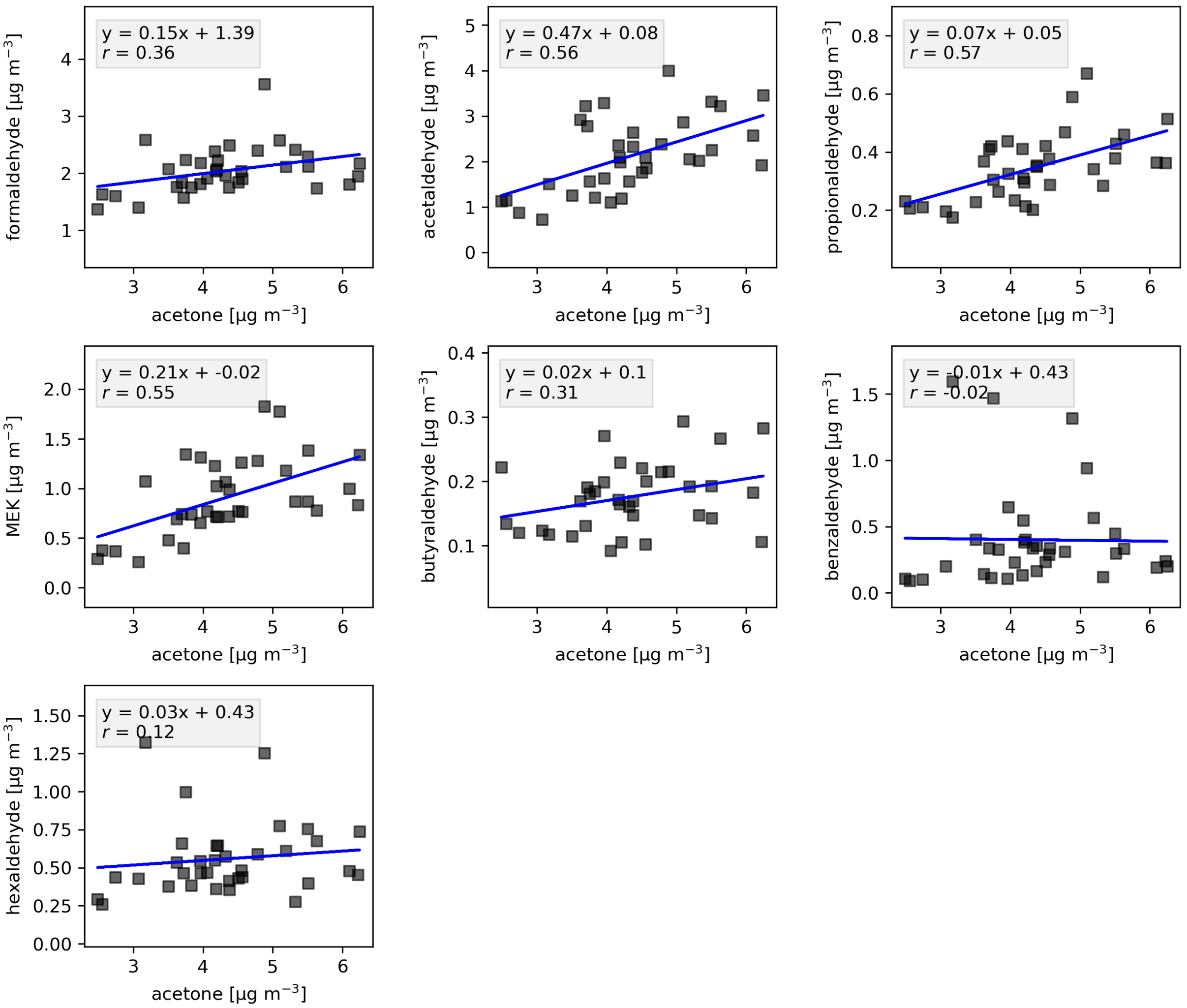

Figure B.2: Scatterplots of carbonyls with acetone concentrations obtained from the daily carbonyl cartridges. Data are fit with linear least-squared regressions.

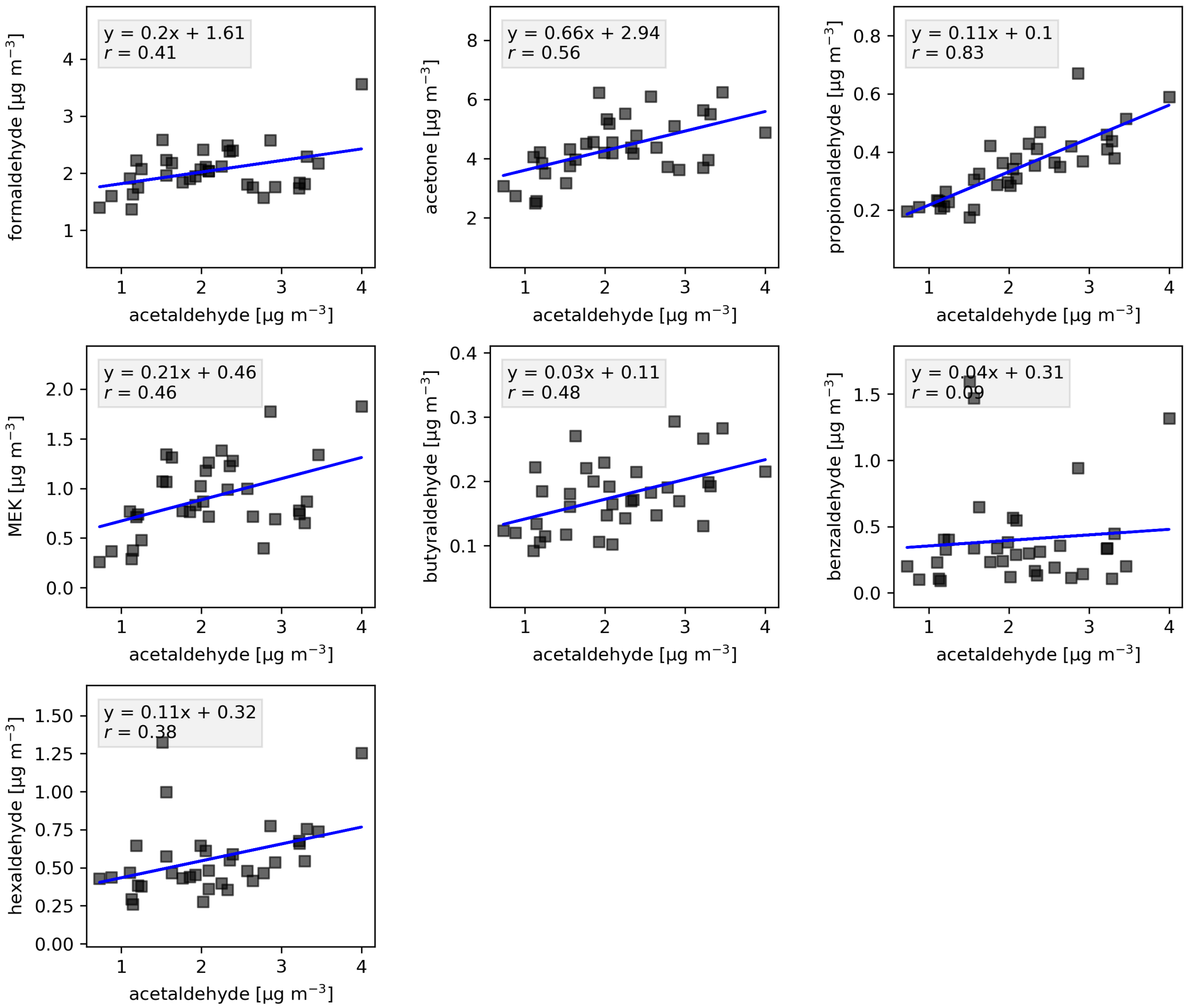

Figure B.3: Scatterplots of carbonyls with acetaldehyde concentrations obtained from the daily carbonyl cartridges. Data are fit with linear least-squared regressions.

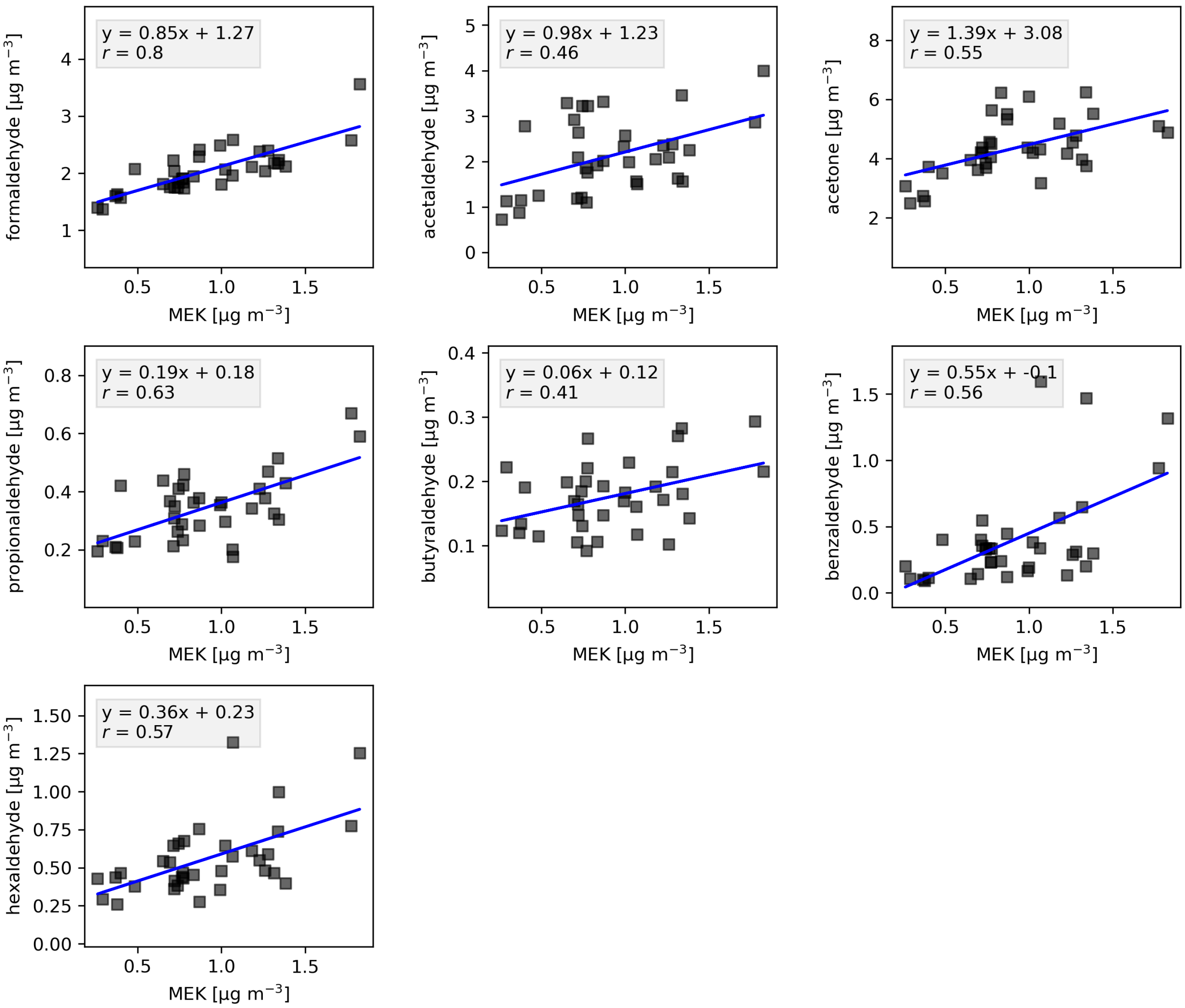

Figure B.4: Scatterplots of carbonyls with MEK concentrations obtained from the daily carbonyl cartridges. Data are fit with linear least-squared regressions.

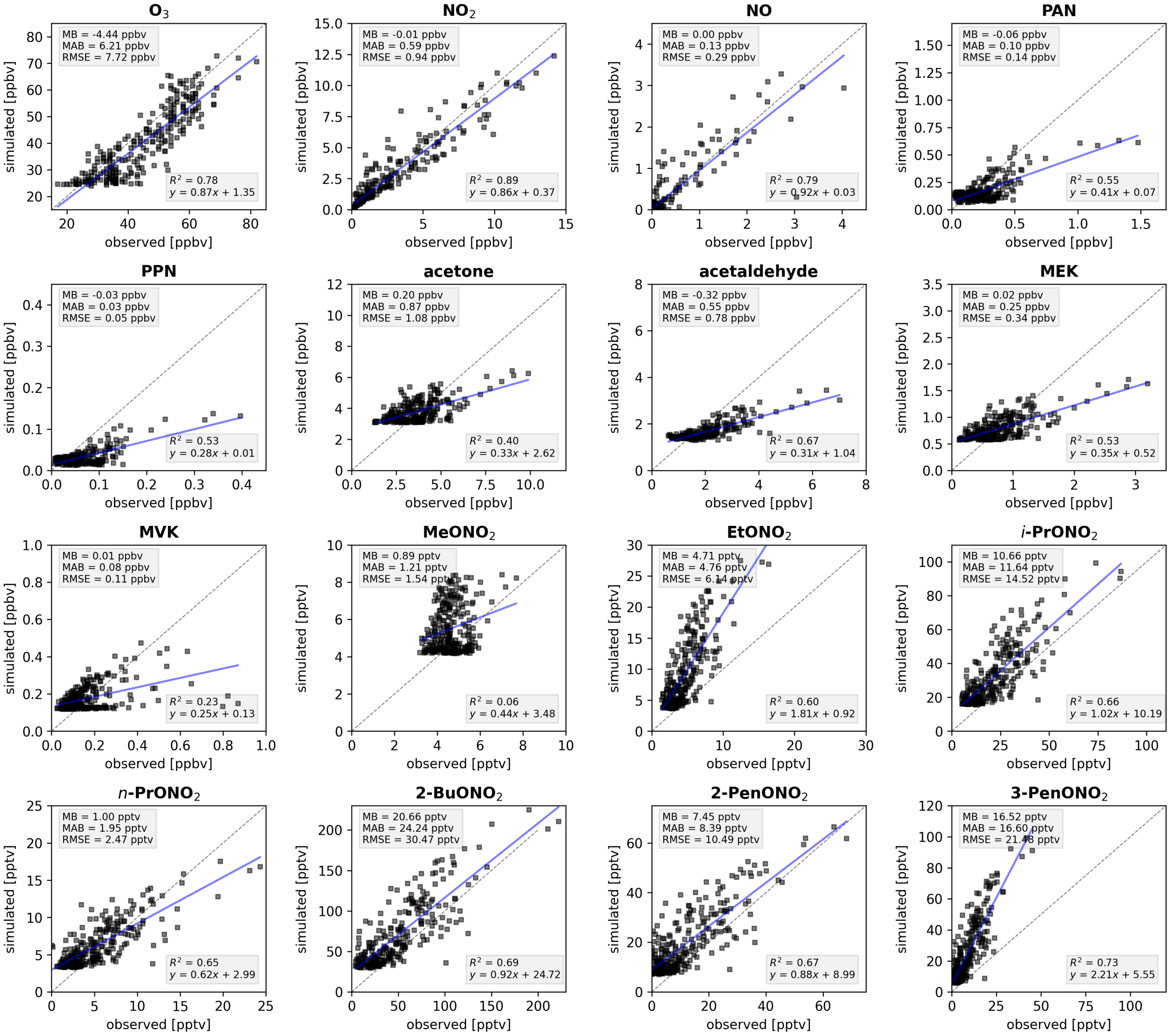

Figure B.5: Comparison of observed concentrations of species left unconstrained within the F0AM box model to their simulated values for the 11-day base case simulation. The 10-min model output time step was averaged to hourly resolution for these comparisons. Each subplot contains the mean bias (MB), mean absolute error (MAB), root mean square error (RMSE), coefficient of determination (R^2) and the linear least-squares fit to the data (blue lines). The dashed black lines represent 1:1 fits.